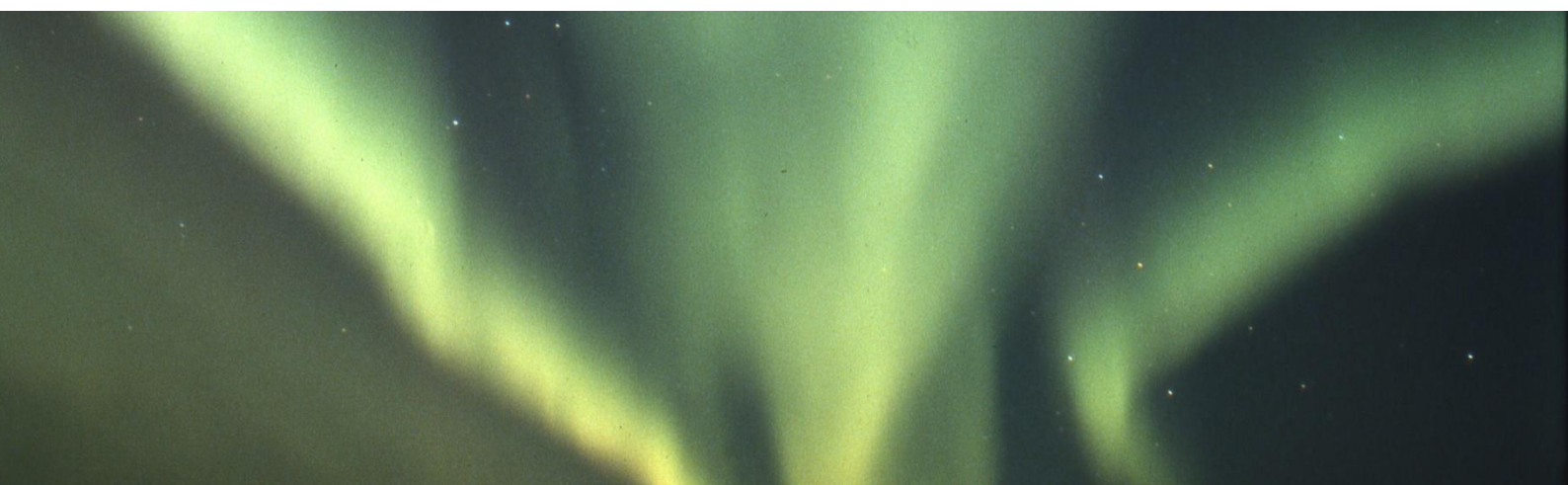


**URSI FINNISH XXXII CONVENTION ON RADIO SCIENCE
AND
ELECTROMAGNETICS 2010 MEETING**

Book of Abstracts

Editors: Emmi Kaivanto, Erkki Salonen



Cover picture taken in Äkäslompolo
by Kari Kaila

**URSI FINNISH XXXII CONVENTION ON RADIO SCIENCE
AND
ELECTROMAGNETICS 2010 MEETING**

Book of Abstracts

Editors: Emmi Kaivanto, Erkki Salonen

University of Oulu

Centre for Wireless Communications

Distribution:
University of Oulu
P.O. Box 8000
FI-90014 University of Oulu
+358 8 553 2880
E-mail [erkki.salonen at ee.oulu.fi](mailto:erkki.salonen@ee.oulu.fi)

© 2010 Emmi Kaivanto, Erkki Salonen and University of Oulu

ISBN 978-951-42-6284-5

Oulun yliopistopaino
Oulu 2010

Welcome

On the behalf of the organizing committee, I wish you warmly welcome to Oulu, the University of Oulu and to the 32nd Finnish Convention on Radio Science. The Convention will be held jointly with the national Electromagnetics 2010 meeting.

The objectives set for the International Union of Radio Science (URSI) are to stimulate and to coordinate studies in the fields of radio, telecommunication, and electronic sciences globally. The scientific activities of URSI are divided into ten Commissions, each responsible for a certain discipline. URSI has also member committees in more than 40 countries, including Finland. The first Finnish Convention of URSI was held in 1953. The event has been held several times in University of Oulu, the latest in 2003 as a two-day event, held together with the Finnish Wireless Communication Workshop. In this time, to keep the budget reasonable, a one-day event is organized. The areas of URSI Commissions C: Radiocommunication Systems and Signal Processing and G: Ionospheric Radio and Propagation are highlighted in this convention.

Traditionally, the URSI National Convention provides a good opportunity to get together the researchers in the wide field of radio science. The convention is also an opportunity for young researchers to present their research results and to get experience in a rather small-scale symposium on their “home ground”.

I thank the individuals in the organizing committee and other volunteers for their efforts towards a successful event. I would also like to thank the members of the Technical Program Committee for reviewing the papers to ensure a high quality technical programme. I express my gratitude to CWC for the support of the event making it free of registration charge. Finally, I would like to thank all the authors and other participants and wish you a pleasant event.

Erkki Salonen

Chairman of the organizing committee

Oulu, August 26, 2010

Program – Sessions A

8:30	Registration and coffee	page
9:30	Opening and welcome	
9:40	Plenary session The ESFRI Roadmap infrastructure facility EISCAT_3D – a new opportunity for ionospheric research <i>Esa Turunen</i>	3
	Session A1: Ionosphere research, <i>chair Kalevi Mursula</i>	
10:30	Conjugate EISCAT-Cluster observations of quiet-time near-Earth magnetotail fast flows and their signatures in the ionosphere <i>T. Pitkänen, A. T. Aikio, O. Amm, K. Kauristie, H. Nilsson</i>	7
10:55	Statistical analysis of incoherent scatter radar data <i>Ilkka I. Virtanen, Juha Vierinen, Mikko Orispää, Markku Lehtinen</i>	11
11:20	Stochastic inversion in calculating the spectrum of signals with uneven sampling <i>Tuomo Nygrén, Thomas Ulich</i>	15
11:45	lunch	
	Plenary session	
12:45	Radar Research at PVT Signature Management <i>A. Tuohimaa</i>	21
	Session A2: Antennas, <i>chair Ari Sihvola</i>	
13:30	Comparison of the bandwidth potential and Q value techniques for estimating antenna bandwidth <i>Jussi Rahola</i>	27
13:55	BST-COC polymer composite based Dielectric Resonator Antenna (DRA) for 2.4 GHz WLAN wrist applications <i>Vamsi K. Palukuru, Kensaku Sonoda, Heli Jantunen</i>	29
14:20	Modal analysis of planar symmetrical folded dipole for mobile terminals <i>Marta Cabedo-Fabrés, Marko Sonkki, Eva Antonino-Daviu, Miguel Ferrando-Bataller, Erkki Salonen</i>	35
14:45	Coffee	
	Session A3: EM waves in medium, <i>chair Seppo Karhu</i>	
15:00	Approximating ideal boundary conditions in electromagnetics with penetrable interfaces <i>Ari Sihvola, Henrik Wallén, Pasi Ylä-Oijala, Ismo V. Lindell</i>	41
15:25	A Glance on Simple Electromagnetic Homogenization Procedures <i>Henrik Kettunen, Jiaran Qi, Henrik Wallén, Ari Sihvola</i>	43
15:50	Some Interesting Effects when Homogenizing Plasmonic Composites <i>Henrik Wallén, Henrik Kettunen, Jiaran Qi, Ari Sihvola</i>	47
16:20	Young scientist award and closing	

Program – Sessions B

		page
	Session B1: Radio channel and interference, chair Esa Kunnari	
10:30	Generalized Exponential Decay Model for Power–Delay Profiles of Multipath Channels <i>Taneli Riihonen, Stefan Werner, Risto Wichman</i>	53
10:55	Wideband characterization of the LMS channel at K-band <i>Antti Roivainen, Veikko Hovinen, Jukka Kyröläinen, Michael Schönhuber, Fernando Pérez Fontán</i>	57
11:20	Analytical Link Distance Derivations for 3d Co-Channel Interference Scenarios <i>Pekka Pirinen</i>	61
11:45	lunch	
	Session B2: New Wireless Systems, chair Jouko Leinonen	
13:30	Two-Hop Relaying in LTE-A Downlink <i>Timo Prokkola</i>	67
13:55	An Efficient Close to Optimal Radio Resource Allocation Mechanism for LTE Downlink Transmission <i>Pradeep Chathuranga Weeraddana, Marian Codreanu, Matti Latva-Aho</i>	71
14:20	TCP Performance over Geostationary Satellite Link <i>Jouko Vankka</i>	75
14:45	Coffee	
	Session B3: Short Range Wireless Communications, chair Matti Hämäläinen	
15:00	Puettava radiotaajuinen tunnistantenni <i>Tiiti Kellomäki, Toni Björninen, Leena Ukkonen, Lauri Sydänheimo</i>	79
15:25	Energy Savings in Mobile Networks: Case Study on Femtocells <i>M. Jada, J. Hämäläinen, R. Jäntti</i>	83
15:50	Performance of IEEE 802.15.4a Receivers in Randomized Multiuser Interference in AWGN Channel <i>Ville Niemelä, Alberto Rabbachin, Matti Hämäläinen, Jari Linatti</i>	87

Technical Program Committee

Dr. Erkki Salonen, chairman (University of Oulu)
Mr. Veikko Hovinen (University of Oulu)
Dr. Seppo Karhu (University of Oulu)
Prof. Keijo Nikoskinen (Aalto University)
Dr. Henrik Wallén (Aalto University)
Prof. Risto Wichman (Aalto University)
Ms. Emmi Kaivanto, secretary (University of Oulu)

Organizing Committee

Mr. Veikko Hovinen
Ms. Emmi Kaivanto
Prof. Keijo Nikoskinen
Ms. Kirsi Ojutkangas
Mr. Ilkka I. Virtanen
Ms. Hanna Saarela
Dr. Erkki Salonen
Dr. Henrik Wallén

Plenary session 1

The ESFRI Roadmap infrastructure facility EISCAT_3D - a new opportunity for ionospheric research

Esa Turunen⁽¹⁾

⁽¹⁾ *EISCAT Scientific Association, Box 812, SE-981 28 Kiruna, Sweden
Email: firstname.lastname@eiscat.se*

EISCAT_3D is Europe's next-generation radar for the study of the high-latitude atmosphere and geospace, to be located in northern Fenno-Scandinavia. EISCAT_3D's capabilities go well beyond anything currently available to the international incoherent scatter research community. The facility consists of several very large active phased-array antenna transmitters/receivers and multiple passive sites located in three countries and comprising from tens of thousands to more than 100 000 individual antenna elements.

In December 2008, EISCAT_3D was placed on the updated ESFRI Roadmap of large research infrastructures, which are of strategic importance for the European research area for the next 20-30 years, by ESFRI, the European Strategy Forum for Research Infrastructures. During the years 2005-2009 the first 2.8 MEUR Design Study of EISCAT_3D was carried out. The Design Study received about 2 MEUR support from EU. In 2010 EU approved a 4.5 MEUR funding for the Preparatory Phase project of EISCAT_3D. The Preparatory Phase starts in October 2010 and is scheduled to be run for 4 years. Construction of EISCAT_3D is to be started in the end of the Preparatory Phase project, provided that international funding commitments are in place by that time. In Finland University of Oulu and Regional Development Funds of Lapland are currently funding a 1 MEUR development project for prototyping EISCAT_3D technology, and a larger project for EISCAT_3D receiver sites in Finland is currently under development.

EISCAT_3D combines several key attributes which have never before been available together in a single radar, such as volumetric imaging and tracking, interferometric imaging, multistatic configuration, improved sensitivity and transmitter flexibility. The use of advanced beam-forming technology allows the beam direction to be switched in milliseconds, rather than the minutes which it can take to re-position dish-based radars. This allows very wide spatial coverage to be obtained, by interleaving multiple beam directions to carry out quasi-simultaneous volumetric imaging. It also allows objects such as satellites and space debris to be tracked across the sky. At the passive sites, the early design allows for at least five simultaneous beams at full bandwidth, rising to at least over twenty beams if the bandwidth is limited to the ion line, allowing the whole range of the transmitted beam to be imaged from each passive site, using holographic radar techniques.

EISCAT_3D has a modular configuration, which allows an active array to be split into smaller elements to be used for aperture synthesis imaging. The result will be an entirely new data product, consisting of range-dependent images of small sub-beamwidth scale structures, with sizes down to 20m. EISCAT_3D will be the first

phased array incoherent scatter radar to use a multistatic configuration. A minimum of five radar sites, consisting of two pairs located around 120km and 250km from the active site respectively, on baselines running East and South from the active core, is envisaged in the Design Study. This would provide an optimal geometry for calculation of vector velocities in the middle and upper atmosphere. However no decisions on the locations of the EISCAT_3D sites have yet been made. The currently starting Preparatory Phase project will define the site locations in an early phase, based on optimization of science merits and the use of nationally available and feasible infrastructure possibly still to be developed.

The gain of the EISCAT_3D antennas and the large size of the active site arrays will deliver an enormous increase in the figure-of-merit relative to any of EISCAT's existing radars. An active site of 5,000 elements would already exceed the performance of the current EISCAT VHF system, while a active site comprising 16,000 elements, as suggested in the Design Study during the years 2005-2009, will exceed the sensitivity of the present VHF radar by at least an order of magnitude. Each transmitter unit will have its own signal generator, allowing the generation and transmission of arbitrary waveforms, limited only by the available transmission bandwidth and spectrum mask as allocated by the respective frequency management authorities. This allows the implementation of all currently used and envisaged modulation schemes and antenna codings (such as polyphase alternating codes, array tapering, orbital angular momentum beams) and also provides the possibility to adopt any kind of future code. In addition, it will allow advanced clutter mitigation strategies such as adaptive null steering and null shaping.

In Finland, a recent new proposal of developing a software radio solution for EISCAT_3D signal processing, based on the use of clustered general purpose computers, instead of dedicated hardware for the second level beam forming, may lead to significant reduction in the costs estimated during the Design Study. Most importantly, with the proposed solution a more flexible use of methods based on inversion mathematics is envisaged. This proposal will be prototyped and evaluated during the nationally funded Finnish project which supports the Preparatory Phase, using a test receiver based on the industrially produced LOFAR antennas for radio astronomy.

In this talk the concept solutions proposed for EISCAT_3D and the upper atmosphere and geospace science case for EISCAT_3D are reviewed. Studies of atmospheric energy budget, space plasma physics with both small-scale structures and large-scale processes, as well as geospace environment monitoring and possible service applications are reviewed by showing the recent highlights by the current EISCAT incoherent scatter radars for comparison.

Session A1

Conjugate EISCAT-Cluster observations of quiet-time near-Earth magnetotail fast flows and their signatures in the ionosphere

T. Pitkänen⁽¹⁾, A. T. Aikio⁽¹⁾, O. Amm⁽²⁾, K. Kauristie⁽²⁾, and H. Nilsson⁽³⁾

⁽¹⁾ *Department of Physics, University of Oulu
P.O.Box 3000, FI-90014, Finland*

Email: timo.pitkanen at oulu.fi

⁽²⁾ *Finnish Meteorological Institute, Helsinki, Finland*

⁽³⁾ *Swedish Institute of Space Physics, Kiruna, Sweden*

INTRODUCTION

Earthward plasma and magnetic flux transport in the magnetotail plasma sheet has been found to be dominated by transient fast flows termed bursty bulk flows (BBFs) [1].

The observed characteristics of BBFs have been found to fit into the theoretical picture of the bubble model [2]. The bubble represents depleted flux tubes that are propelled Earthwards by the interchange instability rising due to the decreased cross-tail current across the flux tubes. The flow shear between the moving bubble and its surroundings creates field-aligned currents on the edges of the bubble that flow into the ionosphere on the dawnside and out of the ionosphere on the duskside of the bubble.

In the ionosphere, BBFs have been found to be associated with narrow, mainly north-south aligned equatorward extending auroral forms termed as auroral streamers, e.g. [3], or local transient activations [4]. Both forms appear at the poleward boundary of the auroral oval and are known as poleward boundary intensifications (PBIs). These auroral signatures are generally considered to represent the ionospheric counterpart of the upward field-aligned current flowing at the duskside edge of a BBF, e.g. [5].

Ionospheric plasma flow corresponding to the Earthward flow in the magnetosphere is roughly equatorwards and the return flows around the field-aligned currents are roughly polewards. These equatorward flows have been observed by SuperDARN radars [6] and some indication of return flows can be found in a paper by [7].

The actual processes behind the generation of BBFs are not yet understood, but generally they are considered to be created by reconnection in the magnetotail neutral line. Many studies have shown connection between poleward boundary intensifications and enhancements in the reconnection electric field, e.g. [8]. However, those studies lacked simultaneous in-situ satellite measurements of associated plasma flow bursts in the magnetotail.

In this paper, we present observations of quiet-time BBFs observed in the magnetotail by Cluster spacecraft and by high-resolution measurements in the ionosphere by the EISCAT incoherent scatter radar, MIRACLE all-sky cameras and magnetometers.

OBSERVATIONS AND DISCUSSION

The observations were made on 17 October 2005 during the Finnish EISCAT measurement campaign. Between 18:10-19:00 UT the four Cluster satellites observed three BBF events in the evening sector near-Earth plasma sheet ($[-13.9, 8.0, -0.8] R_E$ in GSM) (panels a)–b) in Fig. 1). The bursty bulk flows showed typical signatures of

Earthward moving plasma bubble. The BBFs were found to consist of both convective and field-aligned velocity components. In most cases the flow speed in bursts exceeded 300 km/s. All the cases were also associated with tailward flows, which are consistent with return flows around the edges of the plasma bubble. Furthermore, in some cases tailward flows were associated with decreased plasma density, which supports the recent idea of formation of a depleted wake behind the moving plasma bubble [9].

In the ionosphere, the BBFs were associated with auroral streamers seen in EISCAT measurements as narrow latitudinally restricted electron temperature (T_e) enhancements in the F region data (collisional heating by auroral precipitation) (Panel e)). The streamers moved equatorwards and were associated with sharp plasma velocity shears (Panel b)). The 2-D convection pattern was plausibly south-eastward on the poleward side and north-westward on the equatorward side, so that the flow lines were mainly aligned along the streamer direction. The poleward plasma flows on the equatorward side of the streamers were associated with decreased electron density (Panel d)) and enhanced ion temperature (Panel f)) indicating low conductivity and strong poleward electric field present. Within the auroral streamer itself the flow had an equatorward component.

In the mainland all-sky cameras, streamers were magnetically almost east-west aligned auroral arcs showing temporal variations with ≤ 1 -min time scales (Fig. 2).

The location and motion of the auroral streamers at plasma flow shears in the ionosphere agree with the Cluster spacecraft data suggesting that a streamer represents the upward field-aligned current that flows at the duskward side of the Earthward moving plasma bubble observed simultaneously by Cluster. Furthermore, we interpret the enhanced equatorward plasma flows on the poleward side of the streamer to be the ionospheric manifestation of the Earthward plasma flows at Cluster. The narrow poleward flow channels observed on the equatorward side of the streamers are interpreted to represent ionospheric counterpart of return flow around the duskward flank of the bubble.

The reconnection electric field calculated from the EISCAT measurements showed intensifications associated with each BBF and auroral streamer (Blue line in Panel f) in Fig. 1). These observations support the model where bursty bulk flows result from reconnection bursts at the tail neutral line.

CONCLUSIONS

We have studied quiet-time BBFs observed in the magnetotail by Cluster and by high-resolution measurements in the ionosphere by the EISCAT-radars, all-sky cameras and magnetometers.

Several bursty bulk flows seen by Cluster in the plasma sheet could be associated with simultaneous auroral streamers in the conjugate ionosphere observed by EISCAT and all-sky cameras. The streamer-associated ionospheric plasma flow patterns measured by EISCAT agree with the expected ionospheric counterpart flows in the bubble model. The reconnection electric field intensifications associated with BBF-streamer events indicates that the BBFs were created during bursts of enhanced reconnection rate at the tail neutral line.

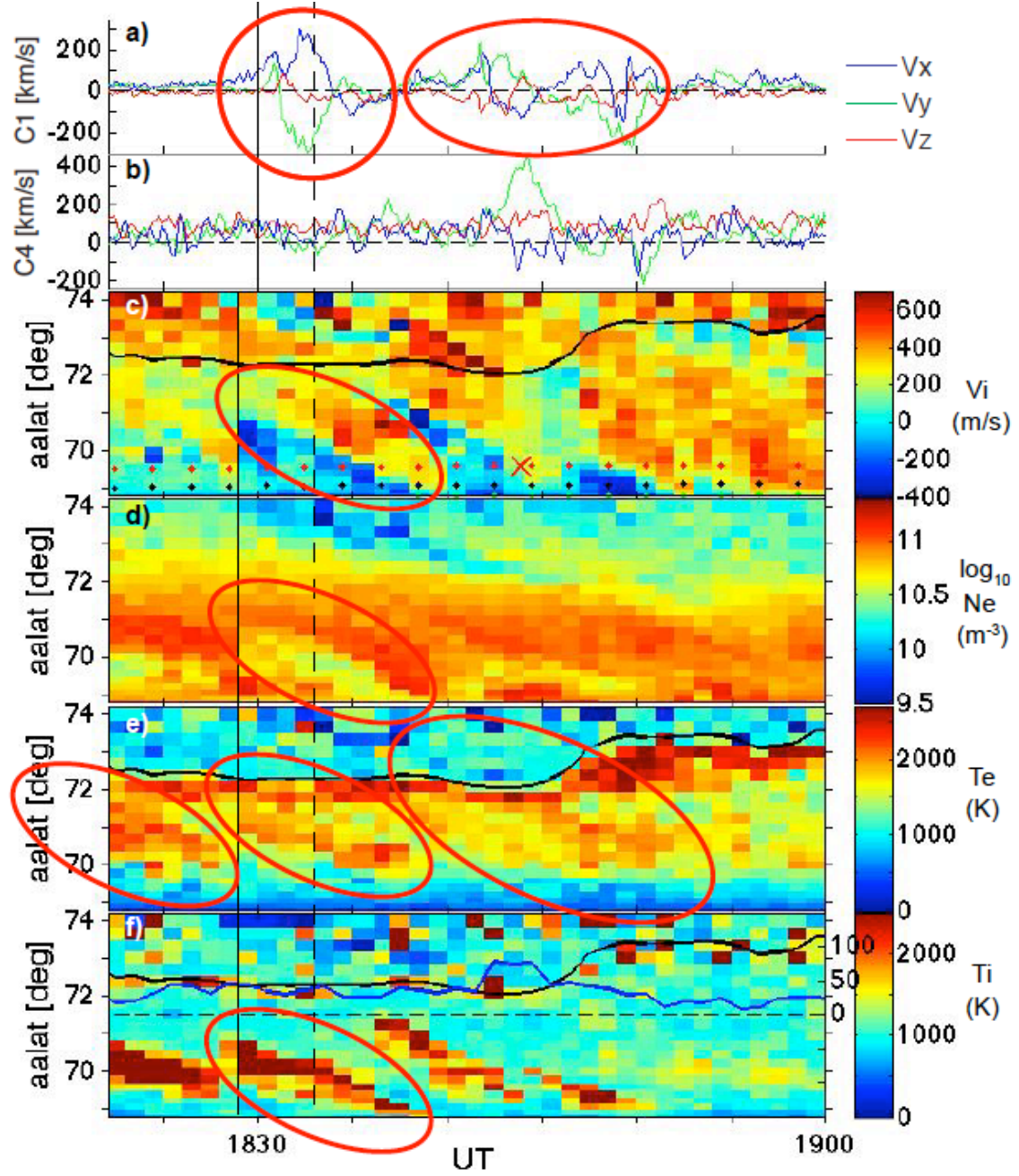


Figure 1: Cluster and EISCAT VHF data from the time interval 18:22–19:00 UT 17 Oct 2005. Panels a)–b): Cluster C1 CIS HIA ion and C4 CIS CODIF proton total velocity components in GSM coordinate system. Panels c)–f): VHF line-of-sight ion velocity (V_i , positive towards the radar), electron density (N_e), electron (T_e) and ion temperatures (T_i). Black curve in panels c), e) and f) marks the polar cap boundary. Blue line in panel f) is the reconnection electric field E_r estimate. Note the separate scale on the right for the E_r . Red circles mark signatures of BBF/streamer in different panels. Black vertical solid line indicates the beginning of a BBF at Cluster C1 at 18:30 UT and first signature of the associated streamer in EISCAT. Black vertical dashed line marks the time instant shown in Fig. 2. Note that only for the BBF beginning at 18:30 UT at C1 corresponding signatures in all EISCAT data panels have been encircled. For other cases corresponding signatures are encircled only in Panels a) and e).

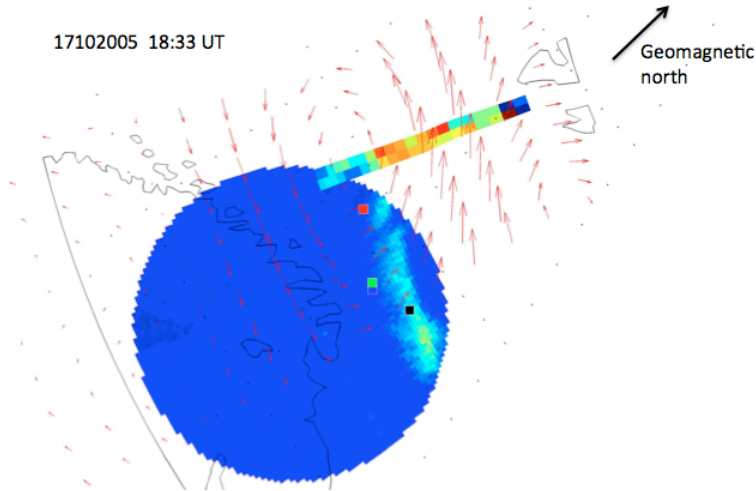


Figure 2: An example frame of conjugate ground-based observations at 18:33 UT. The circle shows auroral emissions by the Kevo all-sky camera mapped to an altitude of 110 km. The colour squares mark the Cluster footpoints (T96, C1 = black, C2 = red, C3 = green and C4 = blue). The two poleward colour bars indicate T_e (west) and V_i (east) measurements by the EISCAT VHF radar 18:33–18:34 UT (see also Panels e) and c) in Fig. 1). Red arrows represent the 2-D ionospheric equivalent currents in arbitrary units derived from the MIRACLE magnetometer data.

REFERENCES

- [1] V. Angelopoulos, W. Baumjohann, C. F. Kennel et al., “Bursty bulk flows in the inner central plasma sheet”, *J. Geophys. Res.*, vol 97, pp. 4027–4039, 1992.
- [2] C. X. Chen, and R. A. Wolf, “Interpretation of high-speed flows in the plasma sheet”, *J. Geophys. Res.*, vol 98, pp. 21 409–21 419, 1993.
- [3] V. A. Sergeev et al., “Multiple-spacecraft observation of a narrow transient plasma jet in the Earth’s plasma sheet”, *Geophys. Res. Lett.*, vol 27, pp. 851, 2000.
- [4] R. Nakamura et al., “Flow bursts and auroral activations: Onset timing and foot point location”, *J. Geophys. Res.*, vol 106, pp. 10 777–10 789, 2001.
- [5] O. Amm, A. Pajunpää, and U. Brändström, “Spatial distribution of conductances and currents associated with a north-south auroral form during a multiple-substorm period”, *Ann. Geophys.*, vol 17, pp. 1385, 1999.
- [6] R. Nakamura et al., “Localized fast flow disturbance observed in the plasma sheet and in the ionosphere”, *Ann. Geophys.*, vol 23, pp. 553–566, 2005.
- [7] S. Zou et al., “PFISR observations of strong azimuthal flow bursts in the ionosphere and their relation to nightside aurora”, *J. Atmos. Sol.-Ter. Phys.*, 71, 729–737, 2009.
- [8] T. Pitkänen, A. T. Aikio, A. Kozlovsky, and O. Amm, “Reconnection electric field estimates and dynamics of high-latitude boundaries during a substorm”, *Ann. Geophys.*, vol 27, pp. 2157–2171, 2009 (see also pp. 3007).
- [9] A. P. Walsh et al., “Cluster and Double Star multipoint observations of a plasma bubble”, *Ann. Geophys.*, vol 27, pp. 725–743, 2009.

Statistical analysis of incoherent scatter radar data

Ilkka I. Virtanen ^(1,2) , Juha Vierinen ⁽¹⁾ , Mikko Orispää ⁽¹⁾ and Markku Lehtinen ⁽¹⁾

⁽¹⁾ *Sodankylä Geophysical Observatory
Tähteläntie 62, FIN-99600 Sodankylä, Finland*

⁽²⁾ *Department of Physics, University of Oulu
P.O.Box 3000, FIN-90014 University of Oulu, Finland
Email: ilkka.i.virtanen@oulu.fi*

INTRODUCTION

The ionosphere is a partly ionised region of the atmosphere, extending from about 50 km to above 1000 km altitude. Weak scattering of radio waves from thermal fluctuations in the ionospheric plasma is called incoherent scatter. Incoherent scatter radars are high power large aperture radar systems, which detect properties of the incoherent scatter – usually its autocorrelation function – in order to gain information of prevailing ionospheric plasma parameters, such as electron density, electron temperature, ion temperature and line-of-sight plasma velocity. The measurement consists of two parts: autocorrelation function of the scattering process is first measured at different heights, and plasma parameters are then estimated from the measured autocorrelation functions.

The ionosphere consists of regions called "D", "E", and "F". The D region is the lowest one extending from 50 to 90 km, the E region is located around 100 km, and the area of strongest day time ionisation around 300 km altitude is the F region. As the plasma parameters in these regions are quite different, also the correlation time of the scattering process has large variations with height: the F region correlation time is short enough to make that part of the radar target severely overspread, whereas the D region is clearly an underspread target. The different regions thus require considerably different measurement techniques, making combined measurements of all ionospheric regions difficult.

Incoherent scatter radars use special modulation methods, which allow the autocorrelation function of the overspread target to be measured with a range resolution much better than transmission pulse length. Most commonly the desired resolution is achieved by combining data from several pulses in a special decoding process. The decoding works well only if the modulation fulfils certain, rather strict, requirements. These requirements can be almost completely relaxed if the decoding process is replaced with methods based on statistical inversion. Using this possibility, we have been able to design so-called multi purpose modulations, which are suitable for simultaneous autocorrelation function measurements from all regions of the ionosphere.

The fit of plasma parameters is a non-linear inverse problem, which is usually solved by means of iterative techniques. The analysis searches for a minimum of a cost function, and the first located minimum is accepted, though there is no guarantee that it is a global one. Errorbars of the plasma parameters are then usually derived from linearised theory, assuming Gaussian error distributions. We have applied a Monte Carlo technique to the plasma parameter fit, which allows the whole error distribution of the plasma parameters to be investigated, without restrictive prior assumptions about its shape. The method can be used to investigate the validity of the iteration results.

LAG PROFILE INVERSION

Due to the typically short correlation time of the incoherent scatter signal, conventional pulse compression by means of phase coding and decoding cannot be used as such with incoherent scatter radars. However, it is possible to first calculate lagged products of the received signal, and then decode these so-called lag profiles. The decoder output then consists of samples of the autocorrelation function at different heights, and the full autocorrelation functions can be constructed by simply re-organising and averaging the decoder output samples. The widely used alternating code technique exploits the lag profile decoding: the modulation consists of a set of phase coded pulses, which produce a complementary code set at all time lags shorter than the pulse length. The alternating code technique thus enables perfect side lobe cancellation in autocorrelation function measurement of a severely overspread target.

The echo signal received with a radar is convolution of the transmission modulation and the target. In simple pulse compression such modulations are used, whose autocorrelation function is exactly or nearly zero at all non-zero time lags. The received signal can then be decoded by correlating it with the modulation. This approach is valid also in lag profile decoding, if the target is replaced by the true lag profile, and the transmission modulation is replaced by its lagged product, the range ambiguity function. If other methods than decoding are available for the deconvolution, one gains the freedom to use arbitrary modulation patterns, as long as the modulation is known to the data analyst. This possibility is exploited in lag profile inversion method [1], where a specialised software package for large linear inverse problems, FLIPS [2], is used for solving the deconvolution problem. The method is identical to decoding if alternating codes are used, but complete side lobe cancellation is possible for any other modulation as well. The price of using non-perfect modulations is paid in the form of increased variance of the results.

The input data of lag profile inversion is raw voltage samples of both attenuated transmitted signals and the received signals. Accurate information of the transmission waveform is thus always available, and we have gained the freedom to transmit literally anything – within the limitations set by the radar hardware.

MULTI PURPOSE MODULATIONS

The difficulty of combined measurements of the whole ionosphere arises from the fact, that the D-region would require pulses to be transmitted with short inter-pulse periods, whereas long pulses transmitted with long inter-pulse periods are sufficient for the upper parts of the ionosphere. A natural choice would be to transmit pulses with non-uniform inter-pulse periods but, because decoding requires pulses to be transmitted with uniform inter-pulse periods, this has not been possible.

As the lag profile inversion analysis [1] has provided us the freedom to transmit any modulation allowed by the radar transmitter, we have been able to perform the first multi purpose experiments with the EISCAT radars. The analysis of combinations of different pulse lengths and inter-pulse periods was first demonstrated [4] and a pulse coding method known as aperiodic transmitter coding [5] was then applied to incoherent scatter radar measurements with some modifications [3]. In addition to the ionospheric works, the aperiodic modulations have been used in special space debris measurements [6], where also plasma parameters were derived from the same data.

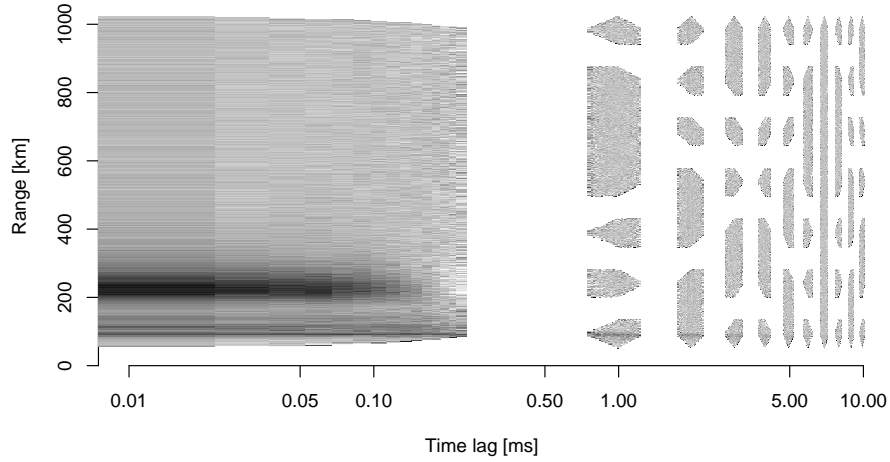


Figure 1: Real part of incoherent scatter autocorrelation function, measured with the PPATC technique [3] in Tromsø, Norway, November 28 2008, 12:32 UT.

MONTE CARLO INVERSION OF PLASMA PARAMETERS

The iterative fit of plasma parameters can be validated by means of Monte Carlo methods, which provide the full error distribution of the plasma parameters. We have recently implemented a variant of the random walk Metropolis algorithm [7], the adaptive Metropolis [8], to the plasma parameter fit. The adaptive sampling simplifies the analysis from the user point-of-view, as the algorithm automatically tunes itself according to the target distribution. Efficient sampling can be achieved with very little prior knowledge of the error distributions. Examples of electron density and ion temperature distributions are given in Fig. 2.

References

- [1] I. I. Virtanen, M. S. Lehtinen, T. Nygrén, M. Orispää, and J. Vierinen. Lag profile inversion method for EISCAT data analysis. *Annales Geophysicae*, 26:571–581, March 2008.
- [2] M. Orispää and M. S. Lehtinen. Fortran Linear Inverse Problem Solver (FLIPS). *Inverse Problems and Imaging*, 2010. accepted for publication.
- [3] I. I. Virtanen, J. Vierinen, and M. S. Lehtinen. Phase-coded pulse aperiodic transmitter coding. *Annales Geophysicae*, 27:2799–2811, July 2009.
- [4] I. I. Virtanen, M. S. Lehtinen, and J. Vierinen. Towards multi-purpose IS radar experiments. *Annales Geophysicae*, 26:2281–2289, 2008.
- [5] S. V. Uppala and J. D. Sahr. Spectrum estimation of moderately overspread radar targets using aperiodic transmitter coding. *Radio Science*, 29:611–623, May 1994.
- [6] J. Vierinen, M. S. Lehtinen, J. Markkanen, and I. I. Virtanen. Measuring space debris with phase coded aperiodic transmission sequences. In *Proceedings of the Fifth European Conference on Space Debris, Darmstadt, Germany, 30 March - 2 April 2009*. ESA/ESOC, 2009.

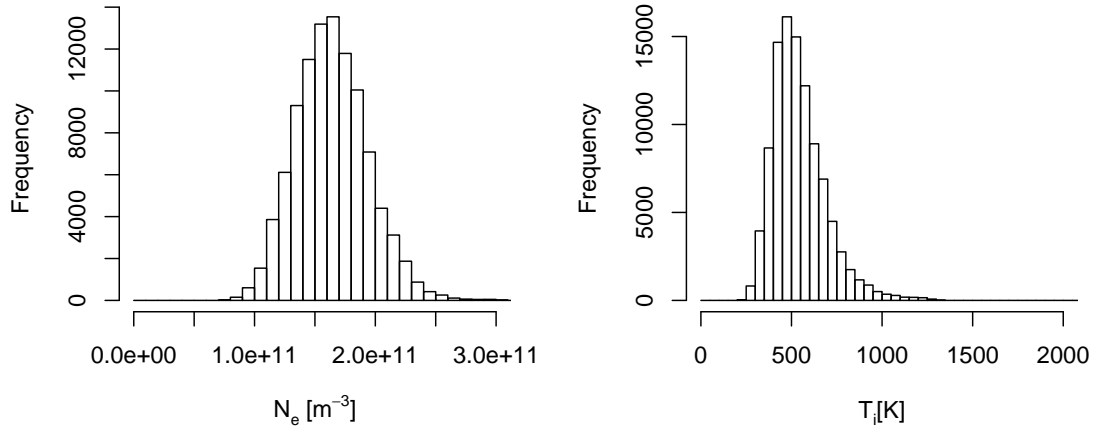


Figure 2: Marginal distributions of electron density (left) and ion temperature (right) at 130 km altitude above Tromsø, Norway, November 27 2008, 20:22 UT. Adaptive Metropolis algorithm was used to sample 100 000 points. The histograms were made using the last 90 000 points, whereas the first 10 000 were excluded as a burnin period.

- [7] N. Metropolis, A. W. Rosenbluth, M. N. Rosenbluth, A. H. Teller, and E. Teller. Equation of state calculations by fast computing machines. *The Journal of Chemical Physics*, 21(6):1087–1092, 1953.
- [8] H. Haario, E. Saksman, and J. Tamminen. An adaptive metropolis algorithm. *Bernoulli*, 7(2):223–242, 2001.

Stochastic inversion in calculating the spectrum of signals with uneven sampling

Tuomo Nygrén ⁽¹⁾

Thomas Ulich ⁽²⁾

⁽¹⁾ *Department of Physics, University of Oulu
P.O. Box 3000, FIN-90014, University of Oulu, Finland
Email: [tuomo.nygren\(at\)oulu.fi](mailto:tuomo.nygren(at)oulu.fi)*

⁽²⁾ *Sodankylä Geophysical Observatory, University of Oulu
FIN-99600, Sodankylä, Finland
Email: [thomas.ulich\(at\)sgo.fi](mailto:thomas.ulich(at)sgo.fi)*

INTRODUCTION

The standard method of calculating the spectrum of a digital signal is based on the Fourier transform, which gives the amplitude and phase spectra at a set of equidistant frequencies from signal samples taken at equal intervals. In this paper a different method based on stochastic inversion is introduced. It does not imply a fixed sampling rate, and therefore it is useful in analysing geophysical signals which may be unequally sampled or may have missing data points. This could not be done by means of Fourier transform without preliminary interpolation. Another feature of the inversion method is that it allows unequal frequency steps in the spectrum, although this property is not needed in practice. The method has a close relation to methods based on least-squares fitting of sinusoidal functions to the signal. However, the number of frequency bins is not limited by the number of signal samples. In Fourier transform this can be achieved by means of additional zero-valued samples, but no such extra samples are used in this method. Finally, if the standard deviation of the samples is known, the method is also able to give error limits to the spectrum. This helps in recognising signal peaks in noisy spectra.

METHOD

Consider a model of a time signal $x(t)$ in terms of sinusoidal oscillations at m angular frequencies ω_k , $k = 1, 2, \dots, m$ with different amplitudes and phases, i.e.

$$x(t) = \sum_{k=1}^m (a_k \sin \omega_k t + b_k \cos \omega_k t). \quad (1)$$

By sampling the signal at times t_j , $j = 1, 2, \dots, n$, we obtain a sample sequence of n numbers

$$x(t_j) = \sum_{k=1}^m (a_k \sin \omega_k t_j + b_k \cos \omega_k t_j) + \varepsilon_j, \quad j = 1, 2, \dots, n. \quad (2)$$

Here sampling is considered as a measurement of the signal value and ε_j is the true measurement error (not an error estimate). Since $x(t)$ may contain a DC component, it is reasonable to choose $\omega_1 = 0$. Then (2) can be written as

$$x(t_j) = b_1 + \sum_{k=2}^m (a_k s_{jk} + b_k c_{jk}) + \varepsilon_j, \quad (3)$$

where

$$s_{jk} = \sin \omega_k t_j \text{ and } c_{jk} = \cos \omega_k t_j. \quad (4)$$

The amplitudes a_k and b_k are unknowns which are to be determined.

By collecting all unknowns, measurements and measurement errors into column vectors

$$\mathbf{X} = \begin{pmatrix} b_1 \\ b_2 \\ \vdots \\ b_m \\ a_2 \\ a_3 \\ \vdots \\ a_m \end{pmatrix}, \quad \mathbf{x} = \begin{pmatrix} x(t_1) \\ x(t_2) \\ \vdots \\ x(t_n) \end{pmatrix} \quad \text{and} \quad \boldsymbol{\varepsilon} = \begin{pmatrix} \varepsilon_1 \\ \varepsilon_2 \\ \vdots \\ \varepsilon_n \end{pmatrix}, \quad (5)$$

all equations of the form (3) can be written as a single matrix equation

$$\mathbf{x} = \bar{\mathbf{A}} \cdot \mathbf{X} + \boldsymbol{\varepsilon}, \quad (6)$$

where

$$\bar{\mathbf{A}} = \begin{pmatrix} 1 & c_{12} & c_{13} & \dots & c_{1m} & s_{12} & s_{13} & \dots & s_{1m} \\ 1 & c_{22} & c_{23} & \dots & c_{2m} & s_{22} & s_{23} & \dots & s_{2m} \\ 1 & c_{32} & c_{33} & \dots & c_{3m} & s_{32} & s_{33} & \dots & s_{3m} \\ \vdots & \vdots & \vdots & \ddots & \vdots & \vdots & \vdots & \ddots & \vdots \\ 1 & c_{n2} & c_{n3} & \dots & c_{nm} & s_{n2} & s_{n3} & \dots & s_{nm} \end{pmatrix}. \quad (7)$$

This is a stochastic linear inversion problem with a well-known solution [1]

$$\mathbf{X}_0 = \bar{\mathbf{Q}}^{-1} \cdot (\bar{\mathbf{A}}^T \cdot \bar{\boldsymbol{\Sigma}}^{-1}) \cdot \mathbf{x}. \quad (8)$$

Here T indicates transpose,

$$\bar{\boldsymbol{\Sigma}} = \langle \boldsymbol{\varepsilon} \cdot \boldsymbol{\varepsilon}^T \rangle \quad (9)$$

is the covariance matrix of the Gaussian random error vector $\boldsymbol{\varepsilon}$ and

$$\bar{\mathbf{Q}} = \bar{\mathbf{A}}^T \cdot \bar{\boldsymbol{\Sigma}}^{-1} \cdot \bar{\mathbf{A}} \quad (10)$$

is the Fisher information matrix. The statistical errors of the unknowns are given by the posteriori covariance matrix

$$\bar{\boldsymbol{\Sigma}}_{\mathbf{X}} = \bar{\mathbf{Q}}^{-1}. \quad (11)$$

Solution (8) gives the unknown amplitudes a_k and b_k for each frequency component. When they are known, the power of the frequency component ω_k is given by

$$P_k = a_k^2 + b_k^2. \quad (12)$$

SAMPLE RESULTS

A special property of the method is that it allows the determination of a greater number of unknowns than the number of measurements. This means that the number of frequency bins in the spectrum can be large. However, the spectral resolution is determined by the length of the sample sequence in the same way as in Fourier transform. Adding more frequency bins has the same interpolating effect as adding zeros to the end of the sample sequence and using Fourier transform.

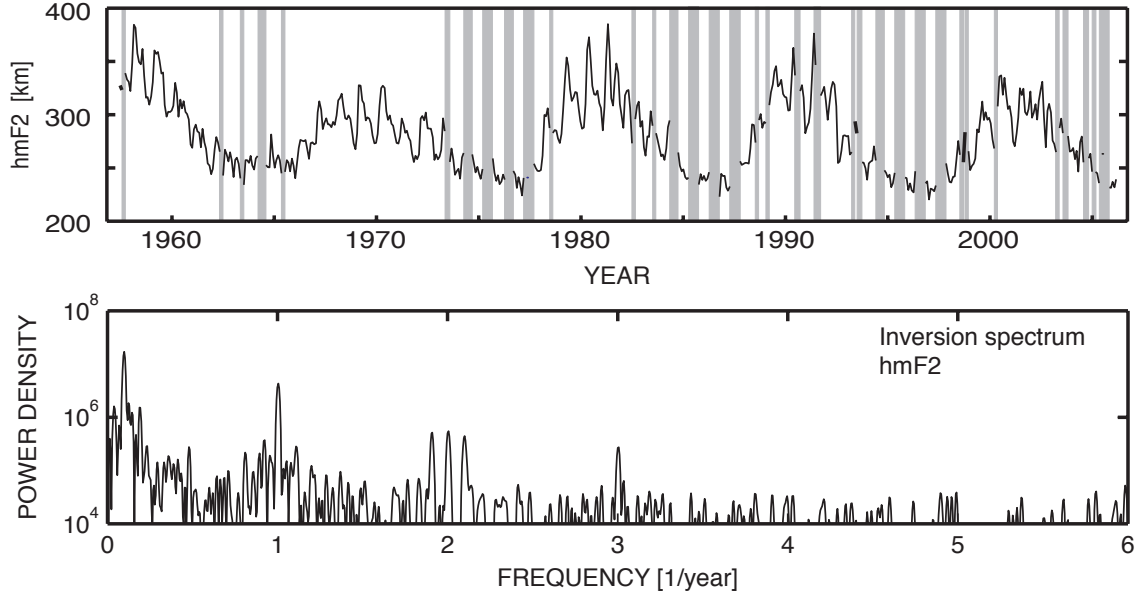


Figure 1: Example of a time series with gaps (grey stripes) and the calculated power spectrum.

As an example of the method, the power spectrum of the virtual height of the ionospheric F layer (hmF2) was calculated. The data were measured at Sodankylä, Finland, in 1957–2006, covering about 4.5 solar cycles. The peak altitude hmF2 was calculated from the peak plasma frequencies of the F2 and E layers and the maximum usable frequency for a 3000-km radio path [2]. Hourly monthly medians averaged over 10–14 LT were used in the analysis. Since months have different lengths, this leads to variable sampling intervals. The data also contains several gaps and therefore Fourier transform could not be directly applied to this time series.

The top panel of Fig. 1 shows the time series with intermediate gaps indicated by the grey stripes. The number of data points in this time series is 491. The power spectrum is shown in the bottom panel. The number of frequencies in the spectrum is 1200 (i.e. 2399 unknowns in the inversion). The most prominent spectral peak at low frequencies is due to the solar cycle variation. The next peaks are the annual (1/year) and semiannual (2/year) variations and the second harmonic of the annual variation (3/year). An interesting feature is that, on both sides of the semiannual variation, additional prominent spectral peaks appear. They are shifted from the semiannual peak by an amount which is equal to the frequency of the solar cycle variation. Hence they are due to nonlinear mixing of the semiannual variation with the solar cycle.

DISCUSSION

The method is only briefly introduced in this paper. A more thorough mathematical treatment shows that it is based on finding the most probable values of the amplitudes and phases of each frequency of the signal spectrum. This also explains why the number of unknowns can indeed exceed the number of measurement values. The single example shown in Fig. 1 demonstrates the power of the method in calculating spectra from data sequences with unequal sampling intervals and data gaps. Other examples have been calculated which indicate that even long gaps in the data have no effect on the widths of the spectral peaks but they only create random noise peaks. If a gap is too long, weak spectral

peaks may be embedded in noise.

The method described in this paper is actually not completely new [3]. However, a new aspect in the present work is that the number of frequency bins in the spectrum is not limited by the number of samples as believed before. This is convincingly demonstrated by Fig. 1, as well as by a number of other examples. The use of stochastic inversion as a starting point also gives a deeper insight in the method than the previous approaches do. Furthermore, if error estimates of data samples are available, the method also gives a possibility to calculate an error limit for each spectral point. This, however, is not investigated here.

References

- [1] T. Nygrén, M. Markkanen, M. Lehtinen, E.D. Tereshchenko, and B.Z. Khudukon, "Stochastic inversion in ionospheric radiotomography," *Radio Sci.*, vol. 32, pp. 2359–2372, 1997.
- [2] P.A. Bradley, and J.R. Dudeney, "A simple model of the vertical distribution of electron concentration in the ionosphere," *J. Atmos. Terr. Phys.*, vol. 35, pp. 2131–2146, 1973.
- [3] M.R. Craymer, "The least squares Spectrum, its inverse transform and autocorrelation function: Theory and some applications in geodesy," (<ftp://geod.nrcan.gc.ca/pub/GSD/craymer/pubs/thesis1998.pdf>) *Ph.D. Dissertation, University of Toronto, Canada*, 1998.

Plenary session 2

Radar Signature Management Research at PVTT and within PVTO2010 SUOJA

Antti Tuohimaa

PVTT

P.O.BOX 5, FIN 34110 Lakiala, Finland

Email: antti.tuohimaa at mil.fi

INTRODUCTION

Radar research in Finnish Defence Forces was originally built around aerial situational awareness and it started with short pulse radars to get range resolution. As the data processing capacity improved defence forces started looking for radars with some pulse compression in order to reach better range resolution and yet to have enough energy to detect targets. Today radar research focuses ever higher pulse compression with wider radar bandwidths. It is not only high range resolution and detailed Doppler processing but also other methods such as (inverse) synthetic aperture radar (I)SAR processing, smart radar control and adaptive waveforms, etc. that has been researched. In the same time noise and multistatic radars impose growing capabilities.

Indeed, it is possible to reach resolutions of 10 cm with today's measurement systems. This makes it possible to detect small targets among clutter and to identify interesting features. For example, in air defence it would be possible to measure length and width and reveal dominant scattering centres of the aircraft depending on the target's flight path. Furthermore, the above developments especially with SAR-image processing (improved resolutions, real time automatic target recognition, interferometry, tomography, polarimetry and moving target identification) require advanced countermeasures for the target to be able to survive in combat. In future satellite -SAR -constellations, and multistatic radars can be expected to enter the area. All this opens an interesting and wide field for research both on radars and radar countermeasures with plenty of challenges.

RESEARCH FACILITIES AT PVTT

Radar signature management is basically studying countermeasures to different radar threats. However, for the survivability and countermeasure studies, it is useful to be able to emulate threat radar up to its signal processing. This is however not straightforward and in some cases it may be even impossible. Therefore, it is usually, taken a consensus with general radars as threat, and yet valuable information can be drawn for operational analysis. The biggest challenge has been to measure the target from different threat angles.

To cope with this an open field test range has been built at Lakiala. It consists of an instrumentation radar from VHF - to Ka-band. The radar has two configuration, the transportable (Fig. 1) and the fixed arm configuration. In the latter case it is installed on the lift at Lakiala's old copper mine tower, which lies ashore of Paroijärvi -lake.



Figure 1: PVTI instrumentation radar in transportable configuration (left);
And heavy duty tilting turntable with a target (right)

A heavy duty tilting turn table has been constructed on the other side of the lake (Fig. 1) at the distance of 230 m from the radar. The tilting turn table is placed more than 4 m above the lake surface in order to ensure that the lake surface will not cause unwanted ground bounce. The radar can be moved up and down in the tower to minimize the multipath effect. The multipath effect due to the lake was modelled in advance to make certain that an acceptable level can be reached. The ground, after radar reflection measurements, was covered with gravel of size 3-6 mm. The table itself was considered on the stealth point of view to provide as low radar cross section (σ) as possible. However, the reflection from the table to target was not minimized, and radar absorbing material is being used to minimize it.

We have measured objects with σ of -60 to -70 dBsm (dB as referred to 1 square meter) on the table, and these results can still be markedly improved (Fig. 2, left). The resolution at certain bands is limited by FICORA (Finnish Communication Regulatory Authority), but in 26 - 40 GHz band the 1 cm resolution can be reached. If we predict radar signatures over the prohibited bands with the help of data measured at allowed bands, comparable resolution can be reached at 2-18 GHz. Besides integrated stealth, radars can be countered with active and passive measures such as for example jamming, decoys, chaff and radar camouflage as shown in Fig 2 (top right Land Rover, bottom right Land Rover with radar camouflage).

Radar cross section prediction and analysis play an essential role in defence procurements or product development projects. Typically σ values of new vehicles and decoys are calculated before prototypes are made.

PVTI relies mostly on the CAST software which is based on physical optics combined with physical diffraction theory. Furthermore, method of moments is also implemented in the software, and is used when electrically small targets such as antennae are studied. The software is built by VTT. To have realistic σ it is usually calculated over the **hemisphere** with 1 degree steps or smaller. In addition to the CAST, We use Finite Domain Time Difference methods to study antennae and radar absorbing materials.

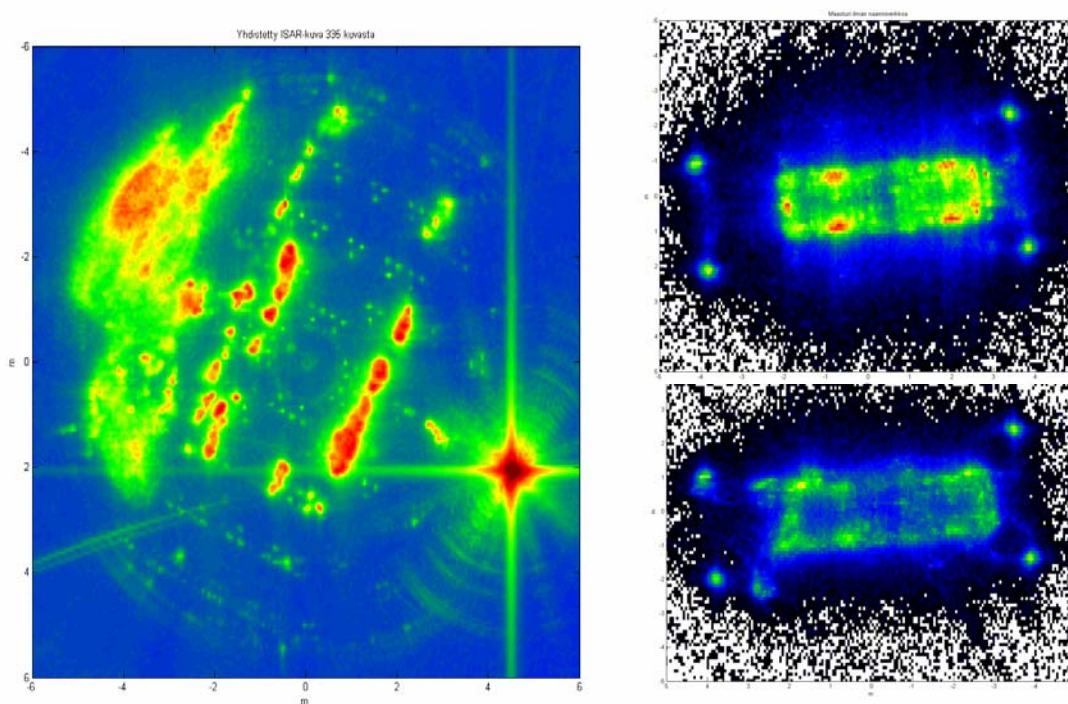


Figure 2: Left motion corrected ISAR –image of the turntable; Top right ISAR-image of a car without radar camouflage; And bottom right ISAR-image of the same car with radar camouflage

The method together with the current processing capacity has not reached to point where the σ values of real size targets can be predicted effectively enough. Indeed, typical target sizes are several metres and the interesting frequency bands may go up to 100 GHz. Therefore, the targets are electrically huge.

Currently PVT is building intensively methods improve the ISAR image processing capacity, including automatic target recognition viewpoints, and tomographic imaging. In the same time tools are being developed to analyze both radar measurements and signature prediction results. The aim is to analyze the results in terms of battlefield survivability.

PVTO2010 SUOJA

Defence Forces Technology Program 2010 (PVTO2010) on Protection is a three year program ending 2012, and its budget is 7.5 MEUR, which is shared on three main tasks: ballistic protection, platform stealth technology, and protection integration (which is mostly simulation and operational analysis).

From the radar signature management viewpoint, the PVTO2010 on Protection includes three interesting branches: 1) low observable unmanned aerial vehicle (UAV) demonstration, which includes state of art available stealth technology (Fig 3), 2) development of a radar cross section prediction software, and

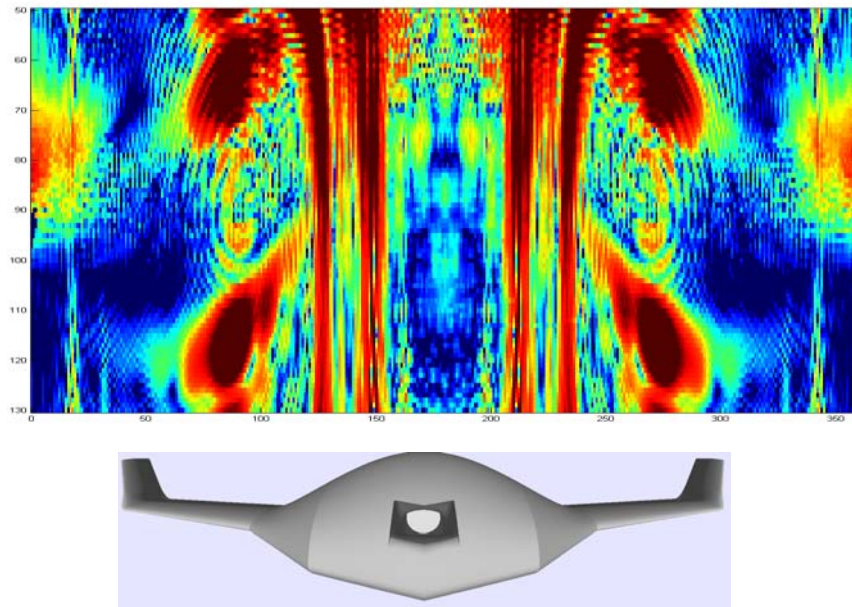


Figure 3: Top radar cross section values of one version of unmanned aerial vehicle as a function of angle at an interesting frequency; Bottom UAV model

an analysis tool to estimate the survivability of targets in a given scenario, and 3) a multistatic radar cross section measurement system.

The low observable UAV produces valuable information, how stealth technology can be utilized in the industry and it also gives a good insight of the effectiveness of different low observable methods in overall. An example of calculated radar cross section is shown in Fig 3. The radar cross section is calculated as a function of horizontal and vertical angle so that the nose of the UAV is in the middle of the figure. It can be easily seen that the winglets cause considerable radar reflection. Thus a new version of the UAV is currently under development. Calculations are completed with CAST software. The model will also be measured at PVTI in order to verify theoretical calculations.

Similarly interesting results can be expected from the software development and the multistatic radar measurement system. The latter ready provides valuable insight in usability of such systems and their challenges.

Fast development of radars and their countermeasures offer an interesting and wide field for research. Multitude of research questions arise from hardware challenges and materials (including metamaterials), as well as from radar cross section calculation and radar data processing, and finally from operational analysis.

POINT OF CONTACT

Principal Scientist: Antti Tuohimaa (PVTI, Signature Management)
E-mail: antti.tuohimaa@mil.fi
Telephone: +358 299 550 557

Session A2

Comparison of the bandwidth potential and Q value techniques for estimating antenna bandwidth

Jussi Rahola ⁽¹⁾

⁽¹⁾ *Optenni Ltd*

*P.O. Box 42, FIN-02211 Espoo, Finland
Email: jussi.rahola@optenni.com*

INTRODUCTION

In general, it is difficult to compare different antennas in terms of their bandwidth because the antennas could be differently matched (overcoupled vs. undercoupled) or not matched at all. This paper presents two techniques that can be used to compare differently matched antennas. These tools can be used in the antenna concept creation phase to select the best antenna candidate that can be later tuned to resonance by modifying the structure or by using a matching circuit.

The Q value technique [1] is based on estimation of the antenna Q value directly from the impedance data. The technique implicitly uses a series reactive component to make the total reactance zero at the analysis frequency. The Q value estimate can be calculated from a simple formula that also includes the derivative of the input impedance.

In the bandwidth potential technique (see e.g. [2]), a two-component matching circuit for conjugate matching is constructed at each analysis frequency and the symmetric bandwidth through the matching circuit is recorded. In the optimized bandwidth potential the symmetric bandwidth is optimized for each analysis frequency.

RESULTS

When the antenna is narrowband (or the obtainable bandwidth through a matching circuit is narrow) the Q value and bandwidth potential approaches give very similar results. Also the optimized bandwidth potential results are quite close to the unoptimized results. However, when the antenna becomes more wideband and especially if a double resonance appears, the Q value technique does not any longer produce reliable results as it was derived using the single resonance assumption. Also the difference between the optimized and unoptimized bandwidth potential can be quite large when a double resonance appears.

In addition, if there is measurement noise or simulation artifacts in the impedance data the Q value may produce erratic results because it uses the derivative of the impedance in the estimation. Therefore, the bandwidth potential technique offers a more reliable method for estimating the obtainable bandwidth.

REFERENCES

- [1] A. Yaghjian and S. Best, "Impedance, bandwidth, and Q of antennas," *IEEE Trans. Antennas Propagat.*, vol. 53, pp. 1298–1324, 2005.
- [2] J. Rahola, "Bandwidth potential and electromagnetic isolation: Tools for analysing the impedance behaviour of antenna systems," in *Proceedings of the EuCAP 2009 conference, Berlin, March 23-27, 2009*, 2009.

BST-COC polymer composite based Dielectric Resonator Antenna (DRA) for 2.4 WLAN wrist applications

Vamsi K. Palukuru*, Kensaku Sonoda, and Heli Jantunen

Microelectronics and Materials Physics Laboratories, EMPART research group of Infotech Oulu, P.O. Box 4500, FIN-90014 University of Oulu, Finland

Abstract— The dielectric properties of Barium Strontium Titanate (BST) and cyclic olefin copolymer (COC) composite are presented at 2.4 GHz frequency using ring resonator structures. A cylindrical dielectric resonator antenna (DRA) based on BST-COC composite operating in the 2.4 WLAN band is presented. The antenna covers the 2.4 -2.484 GHz WLAN band with a return loss of -8 dB. This antenna can be used for wrist-watch type wireless communication devices. The effect of the proximity of the user on the antenna performance is studied through simulation models. A DRA is suitable for wrist type applications due to its directive radiation pattern away from the user. The antenna shows a peak realized gain of 4.9 dBi in free space and 2.5 dBi in the proximity of the user's hand. These DRA types of antenna are found to perform better in proximity to the human body than do the resonant types.

Index Terms— Dielectric resonator antenna, BST-COC composite material, user's effect.

I. INTRODUCTION

With the rapid growth in wireless health care monitoring, devices for consumer applications have received much attention in recent years. Usually, these wireless health monitoring devices comprise wearable antennas placed in the vicinity of a human torso or arm. The antenna performance such as antenna bandwidth, total radiation efficiency and the shape of the radiation pattern will be greatly affected by the presence of the human body, which can be treated as a lossy dielectric medium. The performance of different type of antennas might be affected differently by the proximity of the human body. This is because of different types of coupling mechanism between the antenna and the body. Many researchers have demonstrated resonant type antennas for wearable applications [1-4]. However, the performance of these resonant type antennas is significantly affected by the presence of the human body due to the presence of strong surface currents on the ground plane of the antenna. In order to alleviate these adverse effects, these resonant type antennas are usually separated from the human body by approximately 5 mm, thus increasing the total antenna efficiency. However, this solution increases the overall antenna volume.

Ceramic-polymer 0-3 composites have been attracting considerable interest because they enable the realization of inexpensive 3-D microwave devices and packages. These composites, using thermoplastic polymer, have the additional advantage of simple 3-D fabrication processes, such as injection molding. The dielectric properties of thermoplastic composites prepared from barium-strontium-titanate $\text{Ba}_{1-x}\text{Sr}_x\text{TiO}_3$ (BST) and different kinds of polymers such as polyvinylidene fluoride- co-trifluoroethylene, polyphenylene sulfide (PPS), cycloolefin copolymer, and polypropylene-based polymer alloy have been investigated for radio frequency applications. [5–6].

In this work, a cylindrical dielectric resonator antenna based on BST-COC polymer composite material for wrist type application operating in the 2.4 wireless local area network frequency band (2.4 to 2.484 GHz) is designed, fabricated and measured. The antenna performance of the dielectric resonator antenna (DRA) is less affected by the presence of the human body when compared with that of a resonant type of antenna. This can be attributed to the weaker surface currents on the ground plane of the DRA.

* Corresponding author. Tel.: +358 8 5537963;
E-mail address: vamsi@ee.oulu.fi (V. Palukuru).

II. SUBSTRATE PREPARATION

The preparation of the BST-COC composite through extrusion was reported in detail by Tao *et al.*, [6]. The BST-COC composite with ceramic loading of 45.8 vol % was extruded through a hot mold of suitable sample size (22 mm×43 mm×1 mm) for RF characterization. The DRA was made by hot pressing the BST-COC composite into the desired dimensions. The DRA was soldered onto a ground plane backed Rogers 4003C ($\epsilon_r = 3.38$) substrate. A copper foil about 9 μm thick was transferred onto the BST-COC composite substrates using ASPECT additive circuit transfer technology [7].

III. RF CHARACTERIZATION OF BST-COC SUBSTRATE

A microstrip ring resonator structure was chosen for the RF characterization of the BST-COC composite substrate at 2.44 GHz. The ring resonator structure offers the most accurate and simple method for RF characterization of planar substrates [8]. A schematic layout of the ring resonators operating at 2.44 GHz is presented in Fig.1 (a). Ansoft HFSS (version 11), a commercial 3-D electromagnetic simulator, was used for the design of the ring resonator structures. The resonance frequency and unloaded Q-factor of the ring resonator were measured to be 2.456 GHz and 43.6 respectively.

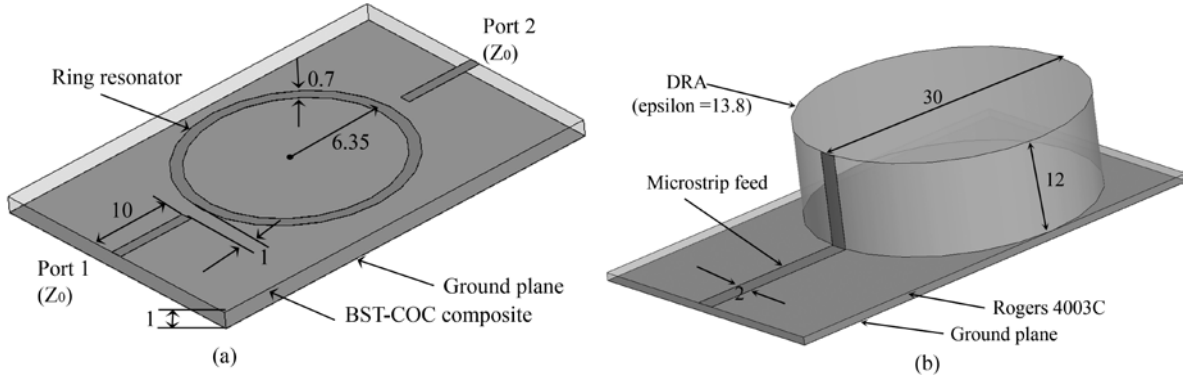


Fig. 1. (a) Schematic layout of the ring resonator structure for the dielectric characterization of BST-COC composite at 2.5 GHz, (b) Schematic layout of a DRA based on BT-COC composite (dimensions in mm).

The effective relative permittivity of the BST-COC composite is extracted from the measured resonance frequency of the ring resonator using the equation (1) [8].

$$\epsilon_{eff} = \left(\frac{c}{2 \times \pi \times r_m \times f_c} \right)^2 \quad (1)$$

where r_m , f_c are the mean radius and resonance frequency of the ring resonator, respectively and c is the velocity of light in free space.

The relative permittivity of the composite material is extracted from the effective relative permittivity using equation 2.

$$\epsilon_r = \frac{2 \times \epsilon_{eff} + \left[1 + \frac{12 \times h}{w_{eff}} \right]^{-0.5} - 1}{\left[1 + \frac{12 \times h}{w_{eff}} \right]^{-0.5} + 1} \quad (2)$$

where h is the thickness of the composite substrate and w_{eff} is the effective width of the microstrip line. This is calculated from the physical width, w taking the fringing fields of the microstrip line into consideration:

$$w_{eff} = w + \frac{1.25 \times t}{\pi} \cdot \left(1 + \ln \left(\frac{2h}{t} \right) \right) \quad (3)$$

The dielectric losses of the composite material are calculated from the measured total losses and estimated conductor losses [9]. The extracted relative permittivity and loss tangent of the BST-COC composite are 14.5 and 0.00235, respectively.

IV. ANTENNA STRUCTURE

Fig.1 (b) depicts the geometry of a BST-COC composite based DRA suitable for wrist applications. The cylindrical DRA has a diameter of 30 mm and a height of 12 mm. The antenna is excited by an edge microstrip probe feed. The DRA operating at 2.44 GHz provides a compact structure, and is thus suitable for application in wrist-watch type wireless communication devices. A copper foil of about 3 μm was laminated onto the DRA to make the metallization of the edge microstrip feed. The DRA was soldered to a 50 mm x 30 mm reverse side-grounded PCB (Rogers R4003C, $\epsilon_r = 3.38$, thickness 0.8 mm) with 17 μm thick copper metallization. A 50 Ω microstrip line was used as feed for the antenna. The complete antenna structure was simulated using Ansoft HFSS (version. 11). The radiation pattern and the total efficiency of the antenna were measured with a Satimo Starlab near-field chamber [10]. A user hand model, Indexsar IXB-060L [11], was used for human hand proximity studies. In this manner the return loss and radiation characteristics of the antennas as a function of the distance between the hand model and the antenna, D , were analyzed.

V. RESULTS

The fabricated ring resonator structure is shown in Fig. 2 (a). The relative permittivity and dielectric loss tangent values of the BST-COC were 14.5 and 2.35×10^{-3} at 2.45 GHz frequency, respectively. A photograph of the fabricated DRA is presented in Fig. 2 (b). The measured return loss and gain in dB of the antenna in free space and as a function of distance from the user's hand model are shown in Fig.3 (a) and (b), respectively. The DRA covers the 2.4 WLAN frequency band with better than -8 dB return loss in all cases. The resonant frequency of the antenna was not significantly affected by the proximity of the human body. This can be attributed to the weak surface currents on the ground plane of the DRA. The gain of the DRA in free space was 2.7 dB at 2.44 GHz. The gain of the antenna increased (from 2 dB to 2.65 dB) as the distance from the human body increased (from 0 mm to 5 mm). Thus, in all cases, the gain of antenna remained better than 2 dB across the 2.4 WLAN frequency band. The peak gain values of the DRA presented are better than that of the resonant type antennas reported by Palukuru *et al.* [1] and K. L. Wong *et al.*, [2] when the antenna is placed near to the human body ($D=0$ mm).

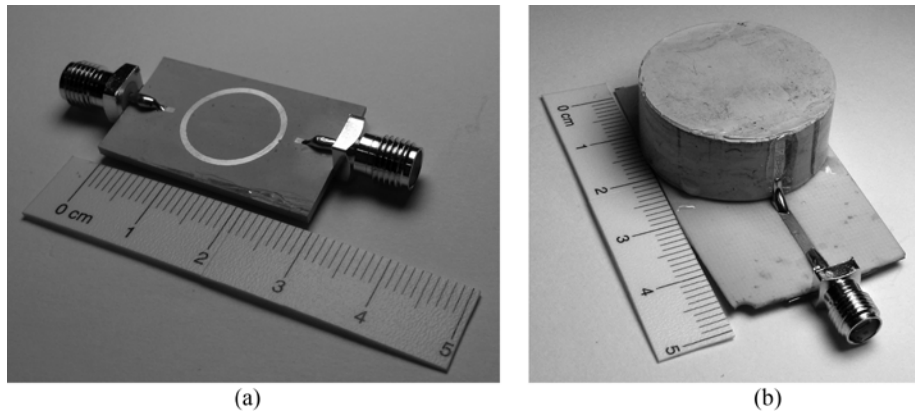


Fig. 2. (a) Photo of the fabricated ring resonator structure on BST-COC composite, (b) Photo of the DRA fabricated.

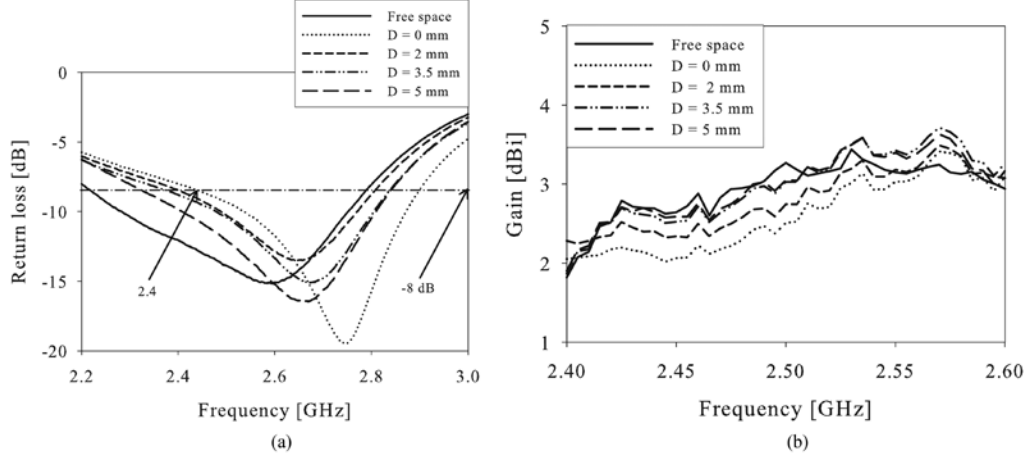


Fig. 3. (a) Measured return loss of the antenna, (b) Measured gain of the antenna with different distances from the human body.

Fig. 4 shows the measured radiation pattern of the DRA in free space and in the presence of the user's hand ($D = 0$ mm, 5 mm). The shape of the radiation pattern is not significantly affected by the proximity of the human hand.

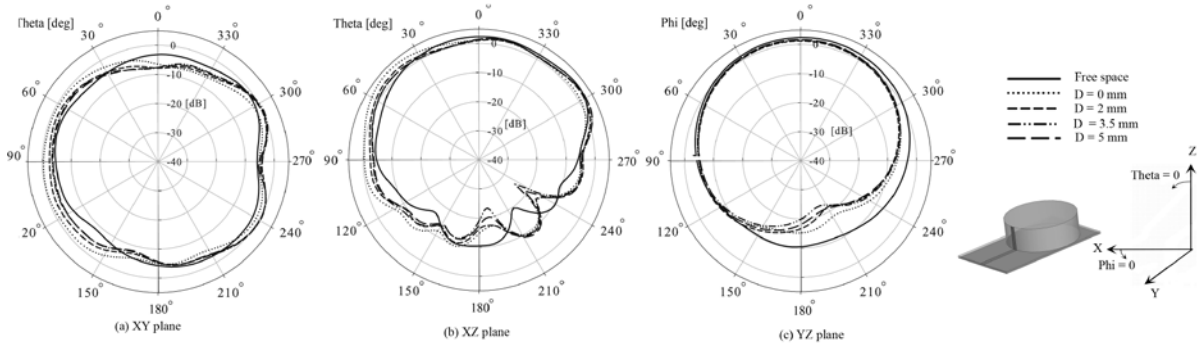


Fig. 4. Measured far-field radiation patterns of the DR antenna; a) in the XY plane; (b) in the XZ plane; and (c) in the YZ plane.

VI. CONCLUSION AND DISCUSSION

The dielectric properties of a BST-COC composite with ceramic loading of 45.8 vol % at 2.45 GHz are presented and a cylindrical dielectric resonator antenna for possible wrist applications is reported. The BST-COC composite has a relative permittivity of 14.5 and a loss tangent value of 2.35×10^{-3} at 2.45 GHz. The antenna covers the 2.4 WLAN frequency band with better than -8 dB return loss and 2 dB gain. Additionally, the impact of the proximity of the user's hand on antenna performance was studied experimentally with a user's hand model. The DRA shows better radiation performance in proximity to the human body compared with that of resonant type antennas. The antenna size can be further miniaturized by the use of a BST-COC composite with a higher value of relative permittivity and by using compact antenna shapes such as rectangular antenna structures.

VII. ACKNOWLEDGEMENTS

The author VP acknowledges the Finnish Foundation for Technology Promotion, the Riitta and Jorma J. Takanen Foundation, and the Tauno Tönninki Foundation for financial support of the work.

REFERENCES

- [1] Palukuru VK, Pekonen A, Pynttäre V, Mäkinen R, Hagberg J, and Jantunen H: An inkjet-printed inverted-F antenna for 2.4-GHz wrist applications. *Microw Opt Technol Lett*. 2009; 51(12): 2936-2938.
- [2] K.L. Wong and C.I. Lin, Characteristics of a 2.4-GHz compact shorted patch antenna in close proximity to a lossy medium, *Microwave Opt Technol Lett* 45 (2005), 480–483.
- [3] C.H. Wu, K.L. Wong, Y.C. Lin, and S.W. Su, Internal shorted monopole antenna for the watch-type wireless communication device for Bluetooth operation, *Microwave Opt Lett* 49 (2007), 942–946.
- [4] Vamsi K Palukuru , Kensaku Sanoda , Juha Hagberg , Heli Jantunen, BST-polymer composite-based planar inverted-F (PIFA) chip antenna for 2.4 GHz wrist applications, *Journal of Integrated Ferroelectrics* [In press].
- [5] Vamsi K. Palukuru, Kensaku Sanoda, Vesa Pynttäre, Tao Hu, Riku Mäkinen, Matti Mäntysalo, Juha Hagberg, Heli Jantunen , Inkjet-Printed RF Structures on BST–Polymer Composites: An Application of a Monopole Antenna for 2.4 GHz Wireless Local Area Network Operation , *Journal of Applied Ceramic Technology*, Published Online: May 20 2010 2:36PM DOI: 10.1111/j.1744-7402.2010.02532.x
- [6] Hu T, Juuti J, Jantunen H, and Vilkmann T: Dielectric properties of BST/polymer composite. *J Eur Ceram Soc*. 2007; 27: 3997–4001.
- [7] Hagberg J, Kekonen T, and Kutilainen T: ASPACT® additive circuit transfer technology, *Proc 16th Eur Microelectron Packag Conf*. 2007; 581-584.
- [8] Yang L, Rida A, Vyas R, and Tentzeris MM: RFID Tag and RF Structures on a Paper Substrate Using Inkjet-Printing Technology. *IEEE Trans Microw Theory Tech*. 2007; 55(12): 2894-2901.
- [9] Gang Zou; Gronqvist, H.; Starski, J.P.; Johan Liu, Characterization of liquid crystal polymer for high frequency system-in-a-package applications," *Advanced Packaging*, *IEEE Transactions on* , vol.25, no.4, pp. 503-508, Nov 2002
- [10] Iversen PO, Garreau P, and Burrell D: Real-time spherical near-field handset antenna measurements. *IEEE Antennas Propag Mag*. 2001; 43: 90–94.
- [11] <http://www.indexsar.com/pdf/Hand.prov.data.5-1106.pdf>. [Accessed on 24th July, 2010].

MODAL ANALYSIS OF PLANAR SYMMETRICAL FOLDED DIPOLE FOR MOBILE TERMINALS

Marta Cabedo-Fabrés⁽¹⁾, Marko Sonkki⁽²⁾, Eva Antonino-Daviu⁽¹⁾
Miguel Ferrando-Bataller⁽¹⁾, Erkki Salonen⁽²⁾

⁽¹⁾*Instituto de Telecomunicaciones y Aplicaciones Multimedia (iTEAM)*
Universidad Politécnica de Valencia, Camino de Vera, s/n, 46022 Valencia, Spain
Email: marcafab at dcom.upv.es, evanda at upvnet.upv.es, mferrand at dcom.upv.es

⁽²⁾*Centre for Wireless Communications (CWC)*
P.O. Box 4500, FI-90014 University of Oulu, Finland
Email: msonkki at ee.oulu.fi, es at ee.oulu.fi

INTRODUCTION

The Theory of Characteristic Modes (TCM), first developed by Garbacz [1] and later refined by Harrington and Mautz in the seventies [2], can be used to obtain the radiating modes of any arbitrarily-shaped metallic structure. These radiating modes, known as characteristic modes, not only present really attractive orthogonality properties, but also bring physical insight into the radiating phenomena taking place on the antenna.

Because of these advantages, the TCM is extremely useful for systematic analysis and design of antenna. Recently, the TCM has been used for the design of diverse wire and planar antennas, obtaining excellent results [3]. In this paper the TCM is going to be used to provide a clear explanation of the operating principle of the planar symmetrical folded dipole antenna.

The characteristic modes (J_n) can be defined as a set of orthogonal real surface currents associated to any conducting object, which depend on its shape and size, and are independent of any excitation source. The resonance frequency of the current modes can be determined by using the information provided by its associated characteristic angles (α_n). Characteristic angles can be defined as

$$\alpha_n = 180^\circ - \tan^{-1}(\lambda_n) \quad (1)$$

where λ_n are the eigenvalues associated to each characteristic mode [2]. From physical point of view, the characteristic angle models the phase angle between a characteristic current J_n and the associated characteristic field E_n . Hence, a mode is at resonance when its characteristic angle α_n is 180° . The closer the characteristic angle is to 180° , the better radiating behavior the mode presents.

As it will be shown, the variation of the eigenvalues as a function of frequency gives information about the resonances and radiating bandwidth of the different current modes. In general, eigenvalues range from $-\infty$ to $+\infty$. Considering a mode is at the resonance when its associated eigenvalue is zero, it is inferred that the smaller the magnitude of the eigenvalue is, the more efficiently the mode radiates when excited. Additionally, the sign of the eigenvalue determines whether the mode contributes to store magnetic energy ($\lambda_n > 0$) or electric energy ($\lambda_n < 0$).

Finally, associated to the characteristic currents, a set of characteristic fields can be computed. Therefore, the field radiated by the antenna can be expressed as a superposition of these characteristic fields or modal fields.

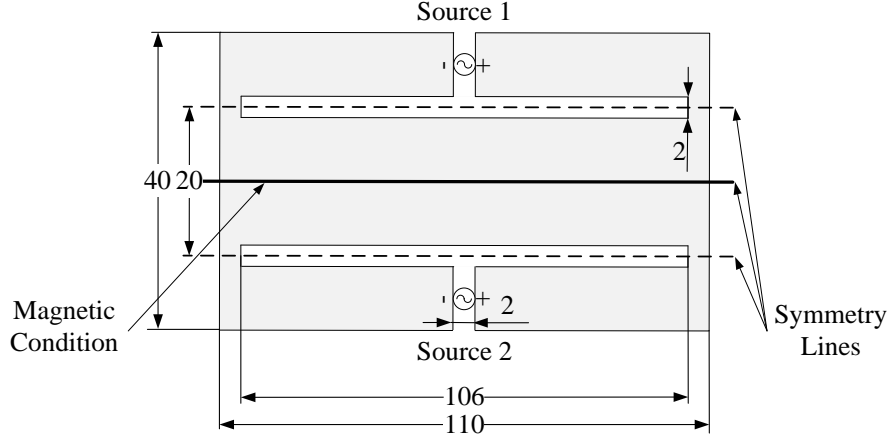


Figure 1: Studied antenna structure with symmetrical slots based on symmetry lines.
White area is air when gray is marked as conducting material. (Units: mm)

MODAL ANALYSIS OF SYMMETRICAL FOLDED DIPOLE

In this section the modal study of the symmetrical folded dipole (Fig. 1) is presented. The antenna structure consists of 110 mm x 40 mm radiating ground plane. Two symmetrical slots (106 mm x 2 mm) divides the ground plane in three separate parts or dipoles based on symmetry lines. It will be shown how, by using two equally fed sources to excite the folded dipoles, an artificial magnetic condition can be created in the symmetry axes between antennas.

Fig. 2 shows the normalized current distribution at resonance for the first nine characteristic modes (J_n) of the symmetrical folded dipole. The structure is complicated and therefore, a higher number of modes should be considered to better understand the antenna behavior. The modes can be classified in antenna or transmission line modes depending on coupling experimented by the three dipoles that conforms the structure.

Antenna modes J_1 , J_3 and J_7 exhibit a magnetic condition at the symmetry axis of the radiating ground plane, so all currents are in phase in the three dipoles in which the structure is divided. On the contrary, transmission line modes J_0 , J_2 , J_4 , J_5 , J_6 and J_8 present currents flowing in opposite phase in the three dipoles that compose the structure.

Fig. 3 depicts the characteristic angles curves for the first nine characteristic modes of the symmetrical folded dipole. One can notice there is a special non resonant mode J_0 whose currents form a close loop around the structure. Antenna modes J_1 , J_3 and J_7 present the softest slope at 180° , and hence, the widest radiation bandwidth. It should be remarked that mode J_8 , in spite of being a transmission line mode, exhibits quite good radiating behavior. This happens because in the mode J_8 , currents in the upper and lower dipoles are in phase, and hence, they reinforce each other providing good radiation performance.

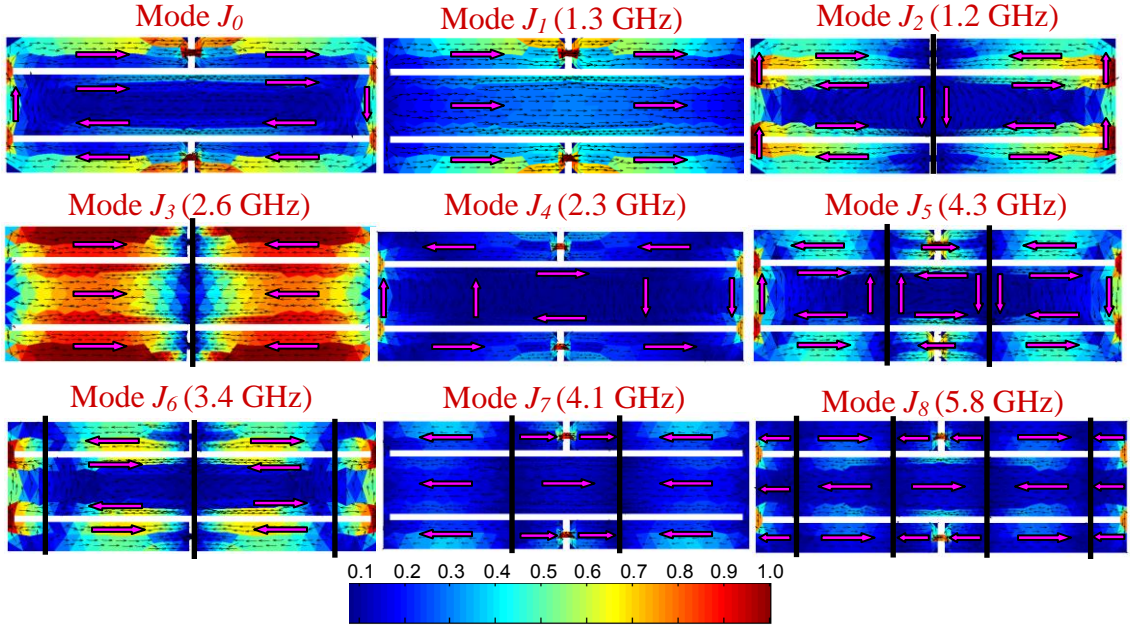


Figure 2: Normalized current distribution at resonance for the first nine characteristic modes of the symmetrical folded dipole.

Fig. 4 studies the contribution of each mode to the total power radiated by the antenna, when it is fed simultaneously at the centre of the upper and lower dipoles. The symmetry of the feeding favors the excitation of antenna modes and avoids the appearance of transmission line modes.

As observed in Fig. 4, when the symmetrical feeding is used only modes J_1 , J_7 and J_8 are excited and hence contribute to radiation. As confirmed by Fig. 3, these three modes are precisely the ones that present widest radiating bandwidth (together with mode J_3 , that is not excited as it presents zero current at the feeding points).

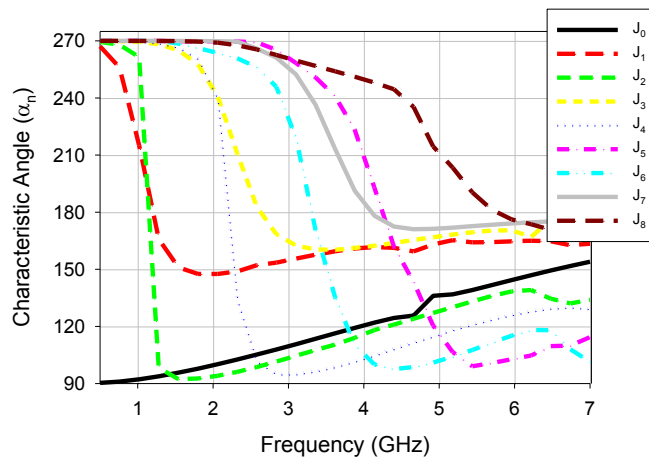


Figure 3: Contribution of each mode to the total radiated power of the double folded dipole when it is fed simultaneously at the centre of the upper and lower dipoles.

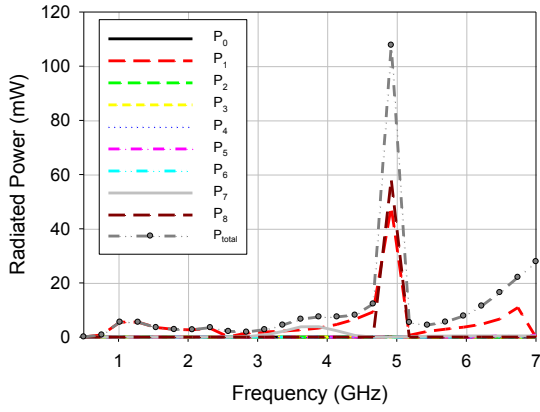


Figure 4: Contribution of each mode to the total radiated power of the symmetrical folded dipole when it is fed simultaneously at the centre of the upper and lower dipoles.

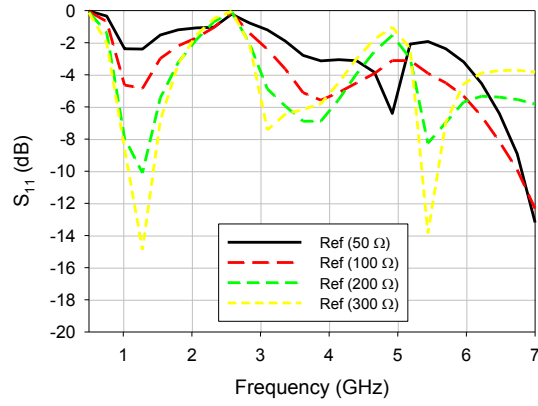


Figure 5: S_{11} parameter of the symmetrical folded dipole with symmetrical feeding calculated for different reference impedances.

Finally in Fig. 5 the S_{11} parameter is computed for different reference impedances when the symmetrical folded dipole is excited symmetrically. Due to the large radiation resistance of the excited antenna modes, the better matching is obtained for the highest reference impedance.

Once more, mode J_1 plays an essential role in the structure, as it dominates at the lowest frequencies; it keeps contribution to the total radiated power long after the resonance, combining modes J_7 and J_8 by creating the second and third radiation peaks, respectively.

CONCLUSIONS

The modal analysis has demonstrated that in the symmetrical folded dipole, there are antenna modes that in case of being excited yield very wideband radiating behaviour. This behaviour is associated to the creation of a magnetic condition at the symmetry axis, which generates currents flowing in phase along the structure that reinforce to increase radiation. Using symmetrical feeding, it is possible to excite only antenna modes, avoiding at the appearance of transmission line modes whose excitation would ruin the matching bandwidth.

REFERENCES

- [1] R. J. Garbacz and R. H. Turpin, "A generalized expansion for radiated and scattered fields", *IEEE Trans. Antennas Propagat.*, vol. AP-19, pp. 348-358, May 1971.
- [2] R. F. Harrington and J. R. Mautz, "Theory of Characteristic Modes for Conducting Bodies", *IEEE Trans. Antennas Propagat.*, AP-19, 5, September 1971, pp. 622-628.
- [3] M. Cabedo, E. Antonino, A. Valero and M. Ferrando, "The Theory of Characteristic Modes Revisited: A Contribution to the Design of Antennas for Modern Applications", *IEEE Antennas and Propag. Magazine*, Vol. 49, no. 5, pp. 52-68, Oct. 2007.

Session A3

Approximating ideal boundary conditions in electromagnetics with penetrable interfaces

Ari Sihvola, Henrik Wallén, Pasi Ylä-Oijala, Ismo V. Lindell

*Aalto University School of Science and Technology
Department of Radio Science and Engineering
P.O. Box 13000, FI-00076 AALTO, Finland
Email: firstname.lastname@tkk.fi*

In problems of electromagnetics, accepted field solutions need to satisfy the Maxwell equations. In addition, for the fields to be unique in a given domain of interest, they also need to obey boundary conditions on the surface of this domain. A well-known boundary condition is the so-called perfect electric conductor (PEC) boundary condition which requires that the tangential (parallel to the surface) electric field vanishes at this boundary. By duality, the PMC (perfect magnetic conductor) boundary condition means that the tangential magnetic field becomes zero at the boundary. A generalization of these two conditions is the PEMC (perfect electromagnetic conductor) boundary condition [1] which means that a linear combination of the electric and magnetic fields cannot have a tangential component. Recently, also boundary conditions involving *normal* components of the fields have been introduced [2, 3]. For example, the so-called DB boundary condition forces the normal components of the electric and magnetic flux densities to vanish.

Ideal boundary conditions are useful in solving electromagnetic problems because the space behind this boundary does not have any effect on the fields. In real-world problems, however, we encounter interfaces, not absolute boundaries. In other words, the fields penetrate through material interfaces, and the structure behind the interface needs to be taken into account in the exact solution of the problem. However, if the material contrast over the interface is very strong, the replacement of the interface by an ideal boundary condition can be a very reasonable approximation. For example, in microwave engineering applications, the surface of a very good conductor can approximate quite well the PEC boundary.

In addition to approximating a material interface by a boundary condition, which can be called the *analytic approach* to electromagnetic problems, also the reverse approximation can be taken, the *synthetic approach*. By this latter approach we mean that the boundary condition is the primary object of our study, and we ask the question which type of material structure would simulate the effect on electromagnetic fields as closely as possible (when compared with the ideal boundary). Intuitively, one expects that the material parameters of such a synthetic structure would need to be very different in magnitude compared with the corresponding parameters in the domain where the fields are calculated, in other words, the medium on the other side of the interface should possess *extreme material parameters*, to borrow a term from recent metamaterials literature [4].

As an example, Figure 1 displays a comparison of the effect of a boundary condition and material interface in the case of plane wave scattering by a sphere. Shown is the scattering efficiency (total scattering cross section normalized by the geometrical cross section) of the sphere which has a size parameter of the value 4. The dotted line shows the value of a DB sphere, $Q_{\text{sca}} = 2.542$, and the two curves show the behavior of the cross section for material spheres when their parameters vary. The permittivity and permeability are equal in both cases and approach zero inversely with the parameter b . For the solid curve, the parameters are real and for the dashed curve they are purely imaginary. Both penetrable spheres clearly approach the DB sphere in terms of this scattering quantity. Indeed, the relative difference is already down to 1% when the sphere permittivity and permeability are 0.1 ($b = 10$).

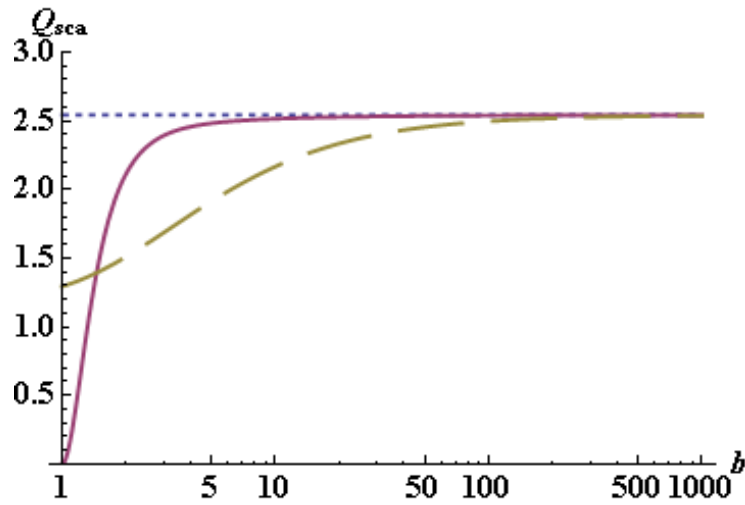


Figure 1: The scattering efficiency of a sphere with size parameter (wave number times radius) of 4. Dotted blue line: DB sphere, solid red line: homogeneous sphere with equal (real) permittivity and permeability of value $1/b$, dashed green line: homogeneous sphere with equal (imaginary) permittivity and permeability of value j/b .

REFERENCES

- [1] I.V. Lindell and A.H. Sihvola, "Perfect electromagnetic conductor," *Journal of Electromagnetic Waves and Applications*, vol. 19, no. 7, pp. 861-869, 2005.
- [2] I.V. Lindell, A.H. Sihvola: "Electromagnetic DB boundary," XXXI Finnish URSI Convention on Radio Science, Espoo, 28.10.2008, *TKK Radio Science and Engineering Publications*, Report R5, October 2008, pp. 81-82.
- [3] I.V. Lindell, H. Wallén, and A. Sihvola, "General electromagnetic boundary conditions involving normal field components," *IEEE Antennas and Wireless Propagation Letters*, vol. 8, issue 16, pp. 877-880, 2009.
- [4] A. Sihvola, S. Tretyakov, A. De Baas, "Metamaterials with extreme material parameters," *Journal of Communications Technology and Electronics*, vol 52, no.9, pp. 986-990, 2007.

A Glance on Simple Electromagnetic Homogenization Procedures

Henrik Kettunen

Jiaran Qi

Henrik Wallén

Ari Sihvola

*Aalto University School of Science and Technology
Department of Radio Science and Engineering
P.O. Box 13000 FI-07600 AALTO
Email: henrik.kettunen at tkk.fi*

INTRODUCTION

In electromagnetics, homogenization means replacing the complex heterogeneous microstructure of a material by a macroscopically homogeneous model. In other words, the effective parameters, electric permittivity ϵ_{eff} and magnetic permeability μ_{eff} , of the material are sought. Homogenization has a long history. However, the problem is still topical, as more complex structures can nowadays be more accurately modeled using computational methods [1, 2]. Using this knowledge, the material parameters can be tuned in a desired way by constructing artificial composite materials.

In this presentation we consider a geometrically simple example, a simple cubic lattice of dielectric spheres in vacuum (see Fig. 1). The spherical inclusions with relative permittivity $\epsilon_i = 10$ occupy a volume fraction $p = 1/10$ of the total volume. The relative permittivity of the external vacuum is denoted by $\epsilon_e = 1$. The spheres are assumed non-magnetic and only the effective relative permittivity ϵ_{eff} is studied.

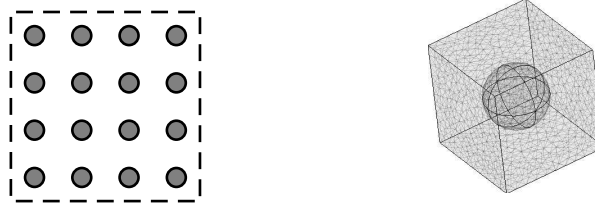


Figure 1: A simple cubic lattice (2D projection) (left) and one unit cell (right).

First, we consider the electrostatic case with an infinite lattice using classical mixing formulas. Then, we study a dynamic case where a propagating wave interacts with the composite material. The material parameters are retrieved numerically using the reflection and transmission data computed from a slab-like sample of the considered material.

The idea of homogenization is based on the condition that the intrinsic inhomogeneities of the material must be notably small compared with the wavelength of the external field. We want to see how quickly and strongly the obtained permittivity starts to deviate from the static reference value as the frequency and the electrical size of the unit cells of the lattice are increasing. We are also seeking limitations after which the obtained parameters are no longer reliable. Our current research deals with determining these limits more accurately and finding more stable methods for composite material homogenization [3, 4].

FROM STATICS TO DYNAMICS

In the literature, there exists a great variety of different mixing formulas [5]. A simple formula suitable for a cubic lattice of spheres is the Maxwell Garnett mixing rule, which using the given parameters ($p = 1/10$, $\epsilon_i = 10$ and $\epsilon_e = 1$) gives

$$\epsilon_{\text{MG}} = \epsilon_e + 3p\epsilon_e \frac{\epsilon_i - \epsilon_e}{\epsilon_i + 2\epsilon_e - p(\epsilon_i - \epsilon_e)} \approx 1.243. \quad (1)$$

A better estimate can be obtained using e.g. Lord Rayleigh mixing formula, but with a volume fraction this small, (1) can be considered a reference accurate enough.

The dynamic case is modeled using COMSOL MULTIPHYSICS, which is a commercial software based on the finite element method (FEM). We are applying the S-parameter retrieval, also known as Nicolson–Ross–Weir technique [6, 7]. The effective permittivity of the material is retrieved based on the simulated reflection and transmission data. In this case, we cannot handle an infinite amount of bulk material. Instead we have to study only a thin sample of the composite. There are two limitations for the sample slab. Naturally, the material parameters should not depend on the amount of the material. This means that the slab must be thick enough to include a sufficient number of unit cells to behave like a bulk material. On the other hand, the weakness of the NRW technique is that the electric thickness of the sample should not exceed $\lambda/2$, as then the solution becomes non-unique. Even though the correct branch closest to the physical solution could be chosen, the solution is contaminated by Fabry–Pérot type of resonances, which occur when the slab thickness becomes an integer multiple of one half wavelength.

Fig. 2 presents the obtained permittivities for different slabs as a function of frequency. The frequency scale is normalized by f_{20} that denotes the frequency where the thickness of one unit cell is $\lambda/20$ compared with the quasistatic effective wavelength. The effect of frequency dispersion is clearly seen. A slab consisting of only one layer gives a higher permittivity compared with the thicker slabs, which indicates that it does not behave like a bulk material. By adding more layers, the permittivity in the static limits starts to converge towards the Maxwell Garnett approximation (1).

The most distinguishable features in Fig. 2 are, however, the unexpected resonances occurring for slabs with 5 and 9 layers within the shown frequency range. These are due to the aforementioned Fabry–Pérot phenomenon where the total thickness of the sample becomes $\lambda/2$ and the reflection from the slab vanishes. Nevertheless, this natural occurrence should not be seen as a resonance in the permittivity curve. Moreover, at the observed (anti-)resonances, the permittivity is decreasing with increasing frequency, which violates the principle of causality. Therefore, the retrieval technique is successful only below the first Fabry–Pérot resonance, where also the size of one unit cell remains very small.

CONCLUSIONS

Homogenization of a simple dielectric cubic lattice composite was studied. The results of the dynamic S-parameter simulations were compared with an analytical static estimate. It was seen that with increasing frequency the retrieved permittivity starts to increase and notably deviate from the static value. When using the S-parameter retrieval, the amount of material, i.e., the number of unit cells must be sufficient for the sample to behave as a bulk material. On the other hand, the total thickness of the sample should remain below one half wavelength, as otherwise the result is contaminated by Fabry–Pérot type of resonances. These restrictions together state that the size of one unit cell must remain extremely small.

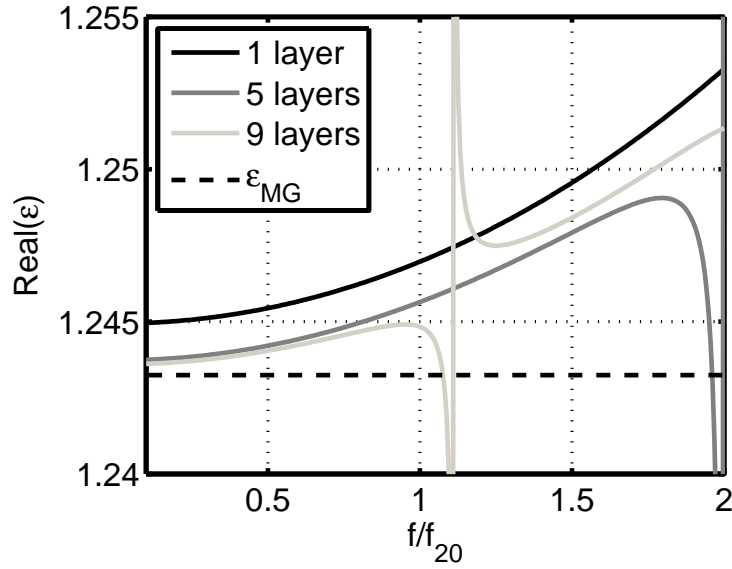


Figure 2: Retrieved permittivities for slabs with different number of layers as a function of (normalized) frequency.

References

- [1] G. W. Milton, *The Theory of Composites*. Cambridge: Cambridge Univ. Press, 2002.
- [2] C. Brosseau, “Modelling and simulation of dielectric heterostructures: a physical survey from an historical perspective,” *J. Phys. D: Appl. Phys*, vol. 39, pp. 1277–1294, Mar. 2006.
- [3] H. Kettunen, J. Qi, H. Wallén, and A. Sihvola, “Homogenization of dielectric composites with finite thickness,” in *Proceedings of ACES 2010*, Tampere, Finland, April 26–29, pp. 490–495, 2010.
- [4] J. Qi, H. Kettunen, H. Wallén, and A. Sihvola, “Frequency dependence of effective permittivity of simple dielectric composites,” in *Proceedings of ACES 2010*, Tampere, Finland, April 26–29, pp. 248–253, 2010.
- [5] A. Sihvola, *Electromagnetic Mixing Formulas and Applications*. London: IEE, 1999.
- [6] A. M. Nicolson and G. F. Ross, “Measurement of the intrinsic properties of materials by time-domain techniques,” *IEEE Trans. Inst. Meas.*, vol. IM-19, pp. 377–382, Nov. 1970.
- [7] W. B. Weir, “Automatic measurement of complex dielectric constant and permeability at microwave frequencies,” *Proc. IEEE*, vol. 62, pp. 33–36, Jan. 1974.

Some Interesting Effects when Homogenizing Plasmonic Composites

Henrik Wallén

Henrik Kettunen

Jiaran Qi

Ari Sihvola

*Aalto University School of Science and Technology
Department of Radio Science and Engineering
PO Box 13000, FI-00076 Aalto, Finland*

Email: henrik.wallén@tkk.fi

INTRODUCTION

The effective permittivity ε_{eff} of a composite is usually not the volume average of its constituents. The impact of the microstructure of the composite is important even for ordinary dielectric composites with modest contrasts between the constituents, and the effect can be dramatic for plasmonic composites with negative permittivity and small losses. In the idealized case, with lossless plasmonic inclusions ($\varepsilon_i < 0$) in a dielectric environment ($\varepsilon_e > 0$), we can theoretically get any real value for ε_{eff} due to plasmonic resonances. When realistic losses are taken into account, the plasmonic resonances are damped, but still the (real part of) ε_{eff} can be significantly larger than ε_e or smaller than ε_i . Moreover, if we consider the plane-wave transmission and scattering from a slab with such resonant inclusions, a straightforward retrieval of ε_{eff} yields reasonable results, but the simultaneously obtained effective permeability μ_{eff} seems unphysical.

In this presentation, we discuss these interesting effects using a geometrically very simple composite.

QUASISTATIC EFFECTIVE PERMITTIVITY USING MIXING FORMULAS

Consider a 2D composite with circular inclusions with permittivity ε_i occupying an area fraction p in an environment with permittivity ε_e . Many mixing formulas for estimating the effective permittivity ε_{eff} of such a composite are available [1], and two of the most popular and useful ones are the Maxwell Garnett formula

$$\varepsilon_{\text{eff}} = \varepsilon_e + \frac{2p \varepsilon_e (\varepsilon_i - \varepsilon_e)}{\varepsilon_i + \varepsilon_e - p(\varepsilon_i - \varepsilon_e)}, \quad (1)$$

and the (symmetric) Bruggeman formula

$$\varepsilon_{\text{eff}} = \frac{1}{2} \left(B \pm \sqrt{B^2 + 4\varepsilon_i \varepsilon_e} \right), \quad B = \varepsilon_e - \varepsilon_i + 2p(\varepsilon_i - \varepsilon_e). \quad (2)$$

For ordinary dielectric mixtures, it is well known that the Maxwell Garnett formula is better suited for mixtures with well separated inclusions, while the Bruggeman formula is more accurate for random mixtures where clustering is allowed [1].

The difference between the estimates (1) and (2) can be significant for mixtures with $1 \leq \varepsilon_e \ll \varepsilon_i$ but both estimates are within the interval $\varepsilon_e \leq \varepsilon_{\text{eff}} \leq \varepsilon_i$ for all $0 < p < 1$. However, if one constituent has negative permittivity, say $\varepsilon_i < 0$ and $\varepsilon_e > 0$, the situation is qualitatively different. Then, the Maxwell Garnett formula predicts one plasmonic resonance at a certain p , while the Bruggeman formula gives a region with complex (lossy) effective permittivity although both ε_i and ε_e are real. One example is shown in Figure 1, and more details on the applicability of mixing formulas for plasmonic composites can be found in [2].

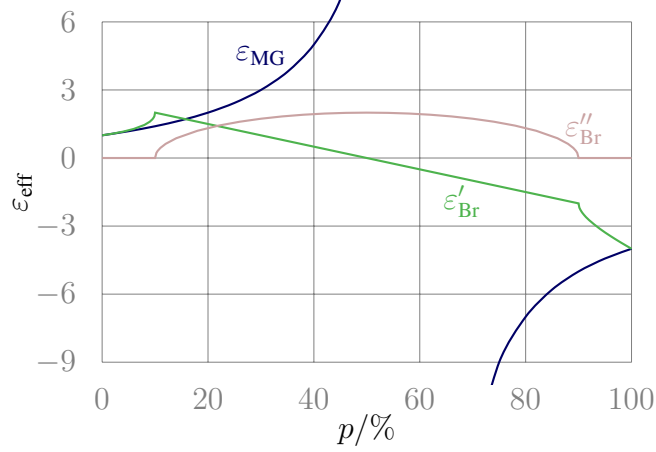


Figure 1: Quasistatic effective permittivity using the Maxwell Garnett (ε_{MG}) and Bruggeman ($\varepsilon_{\text{Br}} = \varepsilon'_{\text{Br}} - j\varepsilon''_{\text{Br}}$) formulas for a composite with cylindrical inclusions with $\varepsilon_i = -4$ occupying an area fraction p in air ($\varepsilon_e = 1$). The Maxwell Garnett formula predicts a plasmonic resonance at $p = 60\%$, while the Bruggeman formula predicts (quite strange) losses for $10\% < p < 90\%$.

The complex frequency dependent permittivity of many metals [3] (approximately) obey a Drude dispersion of the form

$$\varepsilon(\omega) = \varepsilon' - j\varepsilon'' = 1 - \frac{\omega_p^2}{\omega^2 - j\omega\nu}, \quad \begin{cases} \omega_p = \text{plasma frequency,} \\ \nu = \text{damping frequency} \ll \omega_p, \end{cases} \quad (3)$$

where the real part ε' is negative below ω_p , while the imaginary part ε'' can be relatively small. Using a mixture with ε_i given by this Drude model, we get the Lorentz-dispersion

$$\varepsilon_{\text{eff}}(\omega) = 1 + \frac{\omega_{p,\text{eff}}^2}{\omega_{0,\text{eff}}^2 - \omega^2 + j\omega\nu_{\text{eff}}}, \quad \begin{cases} \omega_{p,\text{eff}} = \omega_p\sqrt{p}, \\ \omega_{0,\text{eff}} = \omega_p\sqrt{(1-p)/2}, \\ \nu_{\text{eff}} = \nu, \end{cases} \quad (4)$$

for the effective permittivity using the Maxwell Garnett formula (1). Choosing $\nu = \omega_p/100$ and the fairly small area fraction $p = 10\%$, we get the result shown in Figure 2. If the circular inclusions are arranged in a square lattice, this estimate is extremely accurate in the quasistatic limit compared with the series solution in [4].

S-PARAMETER RETRIEVAL

The probably most common way to determine the effective material parameters $\varepsilon_{\text{eff}}, \mu_{\text{eff}}$ for metamaterials is to simulate or measure the S -parameters for a slab, i.e., the reflection and transmission of a normally incident plane wave, and compute $\varepsilon_{\text{eff}}, \mu_{\text{eff}}$ assuming that the composite slab behaves as a homogeneous isotropic one [5, 6]. However, the validity (or accuracy) of this simple model has also been criticized [7, 8]

In this case, we take a five layer slab with the same composite as in Figure 2 and simulate the S -parameters using a 2D finite-element solver (COMSOL Multiphysics 3.5a). Assuming a square lattice of circular inclusions and scaling the unit cell side-length a differently compared with the plasma wavelength λ_p of the Drude model (3), we get the results in Figure 3. The retrieved ε_{eff} seems very reasonable and it converges, as expected, towards the quasistatic prediction with smaller unit cells compared with the wavelength.

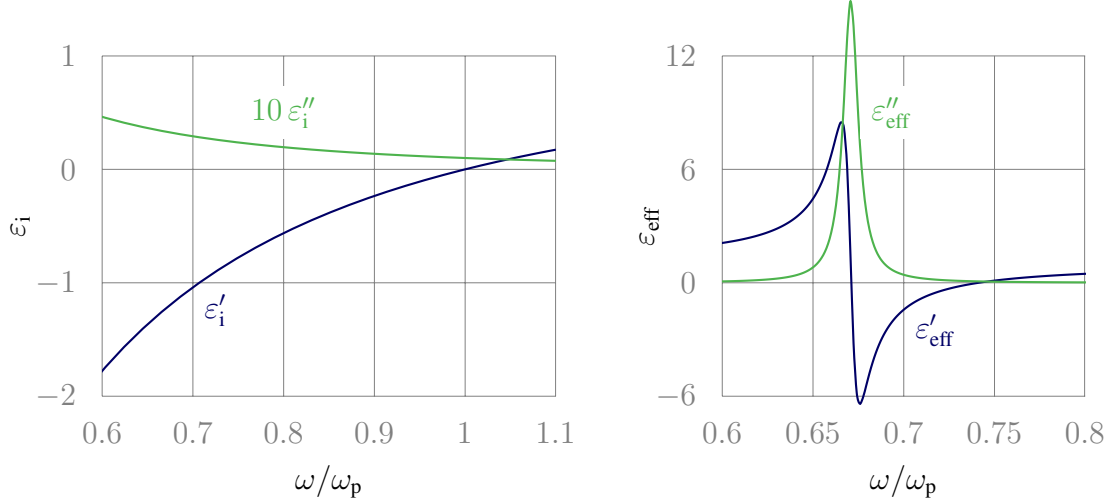


Figure 2: A composite with $p = 10\%$ cylindrical inclusions with the Drude dispersion on the left gives the effective permittivity with the Lorentz dispersion on the right using the Maxwell Garnett formula.

However, the retrieved μ_{eff} shows a similar kind of “anti-resonance” as many metamaterials with more complicated resonant inclusions. This is clearly not reasonable, and it suggests that the five-layer slab is not actually effectively homogeneous enough near the (physically perfectly reasonable) plasmonic resonance. Indeed, comparing the oblique reflection and transmission for the composite slab with the homogenized one reveals that the retrieved ϵ_{eff} and μ_{eff} are not very accurate.

CONCLUSIONS

A composite with plasmonic inclusions with realistic losses can have an effective quasi-static permittivity with a strong resonance at some frequency. However, a slab of the composite does not necessarily behave as a homogeneous one. The problems in the homogenization of the above presented composite slab are actually very similar to the ones in many contemporary metamaterial-realizations, and so this geometrically very simple composite can be useful as a benchmark problem.

REFERENCES

- [1] A. Sihvola, *Electromagnetic mixing formulas and applications*. The Institution of Electrical Engineers, 1999.
- [2] H. Wallén, H. Kettunen, and A. Sihvola, “Mixing formulas and plasmonic composites,” in *Metamaterials and Plasmonics: Fundamentals, Modelling, Applications*, NATO SPS, Ser. B, pp. 91–102, Springer, 2009.
- [3] P. B. Johnson and R. W. Christy, “Optical constants of the noble metals,” *Phys. Rev. B*, vol. 6, pp. 4370–4379, Dec. 1972.
- [4] R. C. McPhedran and D. R. McKenzie, “Electrostatic and optical resonances of arrays of cylinders,” *Appl. Phys.*, vol. 23, pp. 223–235, 1980.
- [5] D. R. Smith, S. Schultz, P. Markoš, and C. M. Soukoulis, “Determination of effective permittivity and permeability of metamaterials from reflection and transmission coefficients,” *Phys. Rev. B*, vol. 65, pp. 195104:1–5, Apr. 2002.

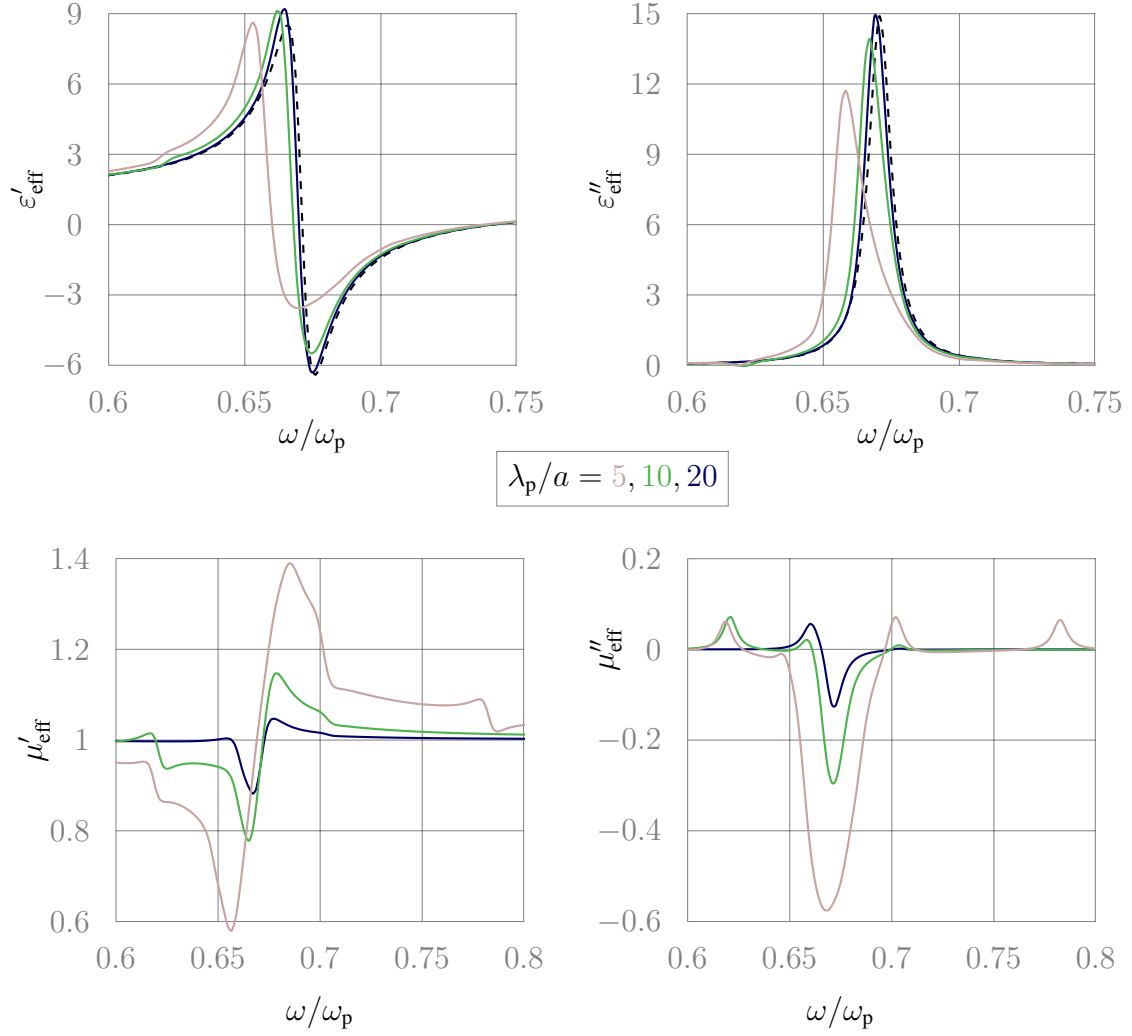


Figure 3: Effective permittivity $\epsilon_{\text{eff}} = \epsilon'_{\text{eff}} - j\epsilon''_{\text{eff}}$ (top) and permeability $\mu_{\text{eff}} = \mu'_{\text{eff}} - j\mu''_{\text{eff}}$ (bottom), retrieved from simulated S -parameters. The permittivity seems reasonable and converges towards the quasistatic prediction (dashed line), but the permeability shows an unphysical “anti-resonance” in addition to weak Fabry–Pérot resonances.

- [6] X. Chen, T. M. Grzegorzczuk, B.-I. Wu, J. Pacheco, Jr., and J. A. Kong, “Robust method to retrieve the constitutive effective parameters of metamaterials,” *Phys. Rev. E*, vol. 70, pp. 016608:1–7, July 2004.
- [7] C. R. Simovski, “Material parameters of metamaterials (a review),” *Opt. Spectrosc.*, vol. 107, no. 5, pp. 726–753, 2009.
- [8] C. Menzel, T. Paul, C. Rockstuhl, T. Pertsch, S. Tretyakov, and F. Lederer, “Validity of effective material parameters for optical fishnet metamaterials,” *Phys. Rev. B*, vol. 81, pp. 035320:1–5, Jan. 2010.

Session B1

Generalized Exponential Decay Model for Power–Delay Profiles of Multipath Channels

Taneli Riihonen ⁽¹⁾

Stefan Werner ⁽¹⁾

Risto Wichman ⁽¹⁾

⁽¹⁾ *Aalto University School of Science and Technology
SMARAD CoE and Dept. of Signal Processing and Acoustics
P.O. Box 13000, FI-00076 Aalto, Finland
Email: {taneli.riihonen, stefan.werner, risto.wichman}@tkk.fi*

INTRODUCTION

We study the modelling of generic multipath channels that, as illustrated in Figure 1, may comprise a line-of-sight path, specular and diffuse reflections as well as single and multiple scattering. We assume propagation environment in which the conditions of wide-sense stationary uncorrelated scattering (WSSUS) [1] are satisfied and channels remain approximately stationary during measuring or data frame transmission.

Our objective is to develop a generalized model for power–delay profiles (PDPs). Given impulse response $h(t)$ of a fading channel, the PDP represents the mean power of multipath components at delay t :

$$P(t) = \mathcal{E}\{|h(t)|^2\}. \quad (1)$$

The expectation operation $\mathcal{E}\{\cdot\}$ denotes statistically the average over the distribution of fast fading and the sample average in the context of measurements. Total transmit (Tx) and receive (Rx) powers are given by P_{Tx} and $P_{Rx} = \int_{-\infty}^{\infty} P(t) dt$, respectively.

PDP modelling is essential for the characterization of propagation environments. It yields many well-known metrics such as the lag τ (the largest τ for which $P(t) = 0$ if $t < \tau$), the channel gain $g = P_{Rx}/P_{Tx}$, the mean delay $\mu = (1/P_{Rx}) \int_{-\infty}^{\infty} tP(t) dt$, and the mean square delay spread $\sigma^2 = (1/P_{Rx}) \int_{-\infty}^{\infty} (t - \mu)^2 P(t) dt$. The Fourier transform of the PDP gives the frequency correlation function (FCF) which is used for determining the channel coherence bandwidth. The PDP can be also used for evaluating the signal-to-interference ratio (SIR) of orthogonal frequency division multiplexing (OFDM) transmission.

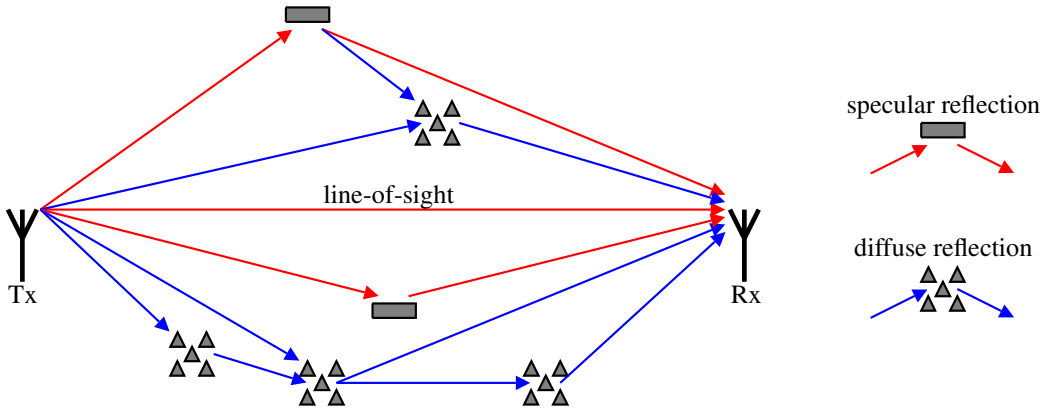


Figure 1: Conceptual multipath radio channel.

CLUSTERED POWER-DELAY PROFILE

We model the PDP as a composite of N clusters as shown in Figure 1. In theory $N \rightarrow \infty$ but in practice N should be quite small which imposes a tradeoff between modelling fidelity and analytical tractability. Each cluster comprises a large number of small-scale multipath components that propagate through the same set of large-scale specular and diffuse scatterers. We let K_n denote the order of the n th cluster, i.e., the number of *diffuse* reflections at the propagation path.

The clustered PDP can be expressed as

$$P(t) = P_{\text{specular}}(t) + P_{\text{diffuse}}(t) = \sum_{n=1}^N P_{K_n}(t, g_n, \tau_n, S_n) \quad (2)$$

in which $P_{K_n}(t, g_n, \tau_n, S_n)$ is the PDP of the n th cluster, characterized by gain g_n , lag τ_n , and the set of delay spread parameters $S_n = \{\sigma_{n,1}, \sigma_{n,2}, \dots, \sigma_{n,K_n}\}$ associated with the K_n diffuse reflections. For simplicity, we consider the practical case in which $\sigma_{n,k}$, $k = 1, 2, \dots, K_n$, are distinct for all n . The total channel gain and lag become $g = \sum_{n=1}^N g_n$ and $\tau = \min_n \tau_n$, respectively. Figure 2 shows an example of a clustered PDP.

Specular clusters

The specular part $P_{\text{specular}}(t)$ models the potential line-of-sight (LOS) path and unscattered (mirror-like) reflections. As $K = 0$ for a specular cluster, its PDP becomes simply

$$P_0(t, g, \tau, \{\}) = g P_{\text{Tx}} \delta(t - \tau) \quad (3)$$

where $\delta(\cdot)$ denotes the unit impulse for which $\delta(t) = 0$ when $t \neq 0$ and $\int_{-\infty}^{\infty} \delta(t) dt = 1$. The only parameters are gain g and lag τ , and the mean delay becomes $\mu = \tau$.

Diffuse clusters with single scattering

The diffuse part $P_{\text{diffuse}}(t)$ models the dense multipath components (DMC) resulting from the combination of single and multiple scattering. Single scattering ($K = 1$) is modelled with the classic exponential PDP [2]:

$$P_1(t, g, \tau, \{\sigma\}) = \frac{g P_{\text{Tx}}}{\sigma} e^{-\frac{t-\tau}{\sigma}} U(t - \tau), \quad (4)$$

where $U(\cdot)$ denotes the unit step for which $U(t) = 0$ if $t < 0$ and $U(t) = 1$ if $t \geq 0$. The parameters are gain g , lag τ and root mean square (RMS) delay spread σ , and the mean delay becomes $\mu = \sigma + \tau$. The classic exponential PDP may be used also for modelling specular clusters (with small σ) because $\lim_{\sigma \rightarrow 0} P_1(t, g, \tau, \{\sigma\}) = P_0(t, g, \tau, \{\})$.

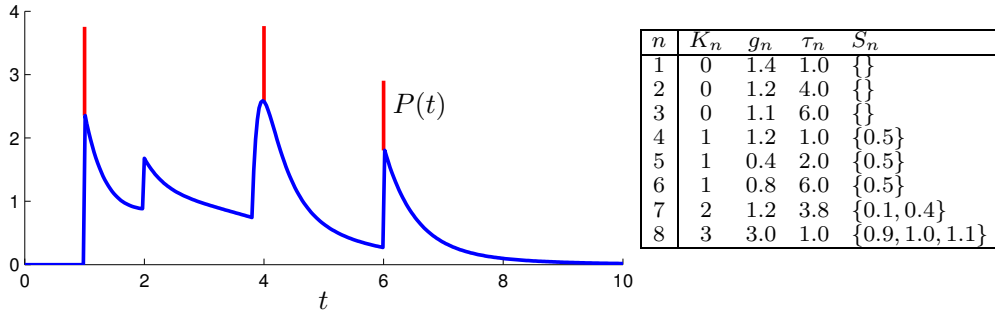


Figure 2: Example power-delay profile ($N = 8$, $P_{\text{Tx}} = 1$).

GENERALIZED EXPONENTIAL DECAY MODEL FOR MULTIPLE SCATTERING

We generalize now the classic exponential PDP given in (4) for modelling clusters with multiple scattering ($K > 1$) in $P_{\text{diffuse}}(t)$. The model is based upon the fact that a propagation path with $K_1 + K_2$ reflections can be partitioned into a cascade of two propagation paths with K_1 and K_2 reflections. This is equivalent to the convolution of partition PDPs:

$$P_{K_1+K_2}(t, g_1 g_2, \tau_1 + \tau_2, S_1 \cup S_2) = \frac{1}{P_{\text{Tx}}} P_{K_1}(t, g_1, \tau_1, S_1) * P_{K_2}(t, g_2, \tau_2, S_2) \quad (5)$$

for any $K_1 \geq 0$ and $K_2 \geq 0$.

Any cluster with K reflections can be partitioned into a cascade of K single-scattering clusters by applying (5) repeatedly. After calculating the multiple convolutions, we get

$$\begin{aligned} P_K(t, g, \tau, S) &= \frac{1}{P_{\text{Tx}}^{K-1}} P_1(t, g_1, \tau_1, \{\sigma_1\}) * P_1(t, g_2, \tau_2, \{\sigma_2\}) * \dots * P_1(t, g_K, \tau_K, \{\sigma_K\}) \\ &= \sum_{k=1}^K \left(\prod_{l=1, l \neq k}^K \frac{\sigma_k}{\sigma_k - \sigma_l} \right) P_1(t, g, \tau, \{\sigma_k\}) \end{aligned} \quad (6)$$

in which $g = \prod_{k=1}^K g_k$ and $\tau = \sum_{k=1}^K \tau_k$ denote the total gain and lag of the cluster, respectively. Thus, a K -fold multiple-scattering cluster is effectively equal to the superposition of K single-scattering clusters interfering both constructively and destructively.

APPLICATION TO THE ANALYSIS OF OFDM TRANSMISSION

In OFDM transmission, orthogonal frequency-domain subcarriers are transformed into a time-domain signal with inverse fast Fourier transform (FFT) of length T_{FFT} . As a countermeasure against multipath fading, cyclic prefix (CP) of length T_{CP} is added to mitigate inter-symbol interference and to facilitate simple frequency-domain equalization. The receiver is synchronized to begin the symbol demodulation at time instant τ_{TOR} which is referred to as the time of reference (TOR).

One application for the PDP model in the analysis of OFDM systems is given by its FCF and the coherence bandwidth. They provide useful information for system design, e.g., when choosing subcarrier spacing and frequency-domain pilot structures.

Another application for the PDP model is in the evaluation of the signal-to-interference ratio:

$$\text{SIR} = \frac{P_U}{P_{\text{ICI}} + P_{\text{ISI}}} \quad (7)$$

for which received power $P_{\text{Rx}} = P_U + P_{\text{ICI}} + P_{\text{ISI}}$ is divided into useful signal power P_U , inter-carrier interference (ICI) power P_{ICI} , and inter-symbol interference (ISI) power P_{ISI} .

Multipath components that arrive outside of the CP window cause ICI and ISI and their effect becomes more pronounced with excessive delay spread. Thus, the power of multipath components can be divided into useful and interference power based on their delays w.r.t. the TOR. For this purpose, we apply a piecewise linear weighting function [3]

$$w(t) = \frac{1}{T_{\text{FFT}}} \max \{0, \min \{T_{\text{FFT}}, t - \tau_a, \tau_d - t\}\} \quad (8)$$

with breakpoints $\tau_a = \tau_{\text{TOR}} - T_{\text{FFT}}$, $\tau_b = \tau_{\text{TOR}}$, $\tau_c = \tau_{\text{TOR}} + T_{\text{CP}}$, and $\tau_d = \tau_{\text{TOR}} + T_{\text{CP}} + T_{\text{FFT}}$. The weighting approach is demonstrated in Figure 3.

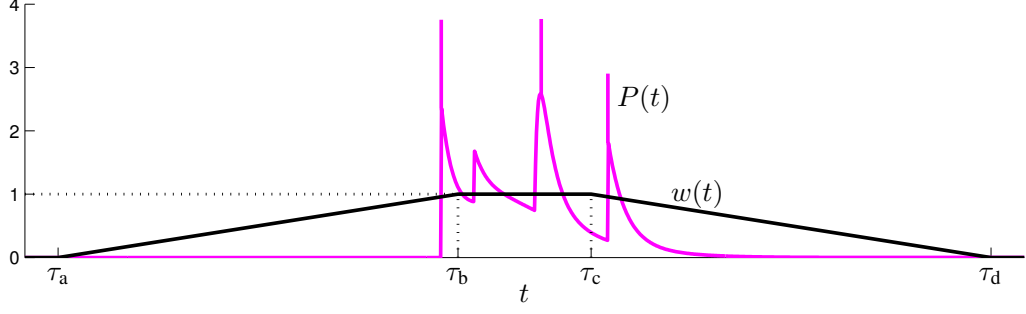


Figure 3: The weighting function.

As a variation of the discrete-case analysis presented in [3], the signal power components can be obtained from the continuous PDP by calculating the following integrals:

$$P_U = \int_{-\infty}^{\infty} w^2(t) P(t) dt, \quad (9)$$

$$P_{ICI} = \int_{-\infty}^{\infty} w(t) P(t) dt - P_U, \quad (10)$$

$$P_{ISI} = \int_{-\infty}^{\infty} (1 - w(t)) P(t) dt. \quad (11)$$

Thus, the shape of the PDP defined by the parameters in (2) and the physical layer OFDM parameters (T_{FFT} , T_{CP}) are involved in a tradeoff determining the performance of the modulation scheme. Furthermore, the PDP model allows to compare different receiver time synchronization schemes through the TOR in the presence of ICI and ISI. In [4], we apply this methodology for the analysis of a full-duplex repeater link.

CONCLUSION

We proposed a generalized model for the power–delay profiles of multipath radio channels. The model is a composite of exponentially-decaying clusters that represent the line-of-sight path, specular reflections, and diffuse reflections with single and multiple scattering. The PDP is useful for the characterization of propagation environment and, in particular, it facilitates analytical evaluation of the performance of OFDM transmission.

REFERENCES

- [1] P. A. Bello, “Characterization of randomly time-variant linear channels,” *IEEE Transactions on Communications Systems*, vol. 11, no. 4, pp. 360–393, December 1963.
- [2] A. A. M. Saleh and R. A. Valenzuela, “A statistical model for indoor multipath propagation,” *IEEE Journal on Selected Areas in Communications*, vol. 5, no. 2, pp. 128–137, February 1987.
- [3] H. Steendam and M. Moeneclaey, “Analysis and optimization of the performance of OFDM on frequency-selective time-selective fading channels,” *IEEE Transactions on Communications*, vol. 47, no. 12, pp. 1811–1819, December 1999.
- [4] T. Riihonen, K. Haneda, S. Werner, and R. Wichman, “SINR analysis of full-duplex OFDM repeaters,” *Proc. 20th IEEE International Symposium on Personal, Indoor and Mobile Radio Communications*, September 2009.

Wideband characterization of the LMS channel at K-band

Antti Roivainen⁽¹⁾, Veikko Hovinen⁽¹⁾, Jukka Kyröläinen⁽¹⁾,
Michael Schönhuber⁽²⁾, Fernando Pérez Fontán⁽³⁾

⁽¹⁾*Centre for Wireless Communications
P.O.Box 4500, FI-90014 University of Oulu, Finland
Email: first.last [at] ee.oulu.fi*

⁽²⁾*Joanneum Research, Austria*

⁽³⁾*University of Vigo, Spain*

INTRODUCTION

The motivation behind our study is the increasing need for mobile satellite multimedia. Satellite based services working at frequency range between 1—3 GHz suffer from lack of available bandwidth due to congestion, higher frequencies in the K-band are now considered as an extension of existing services at L- and S-band. Hercules Transporter C130 aircraft was used to mimic a satellite transmitter at various elevation angles. Long link distance made it possible to include cloud layer and precipitation effects in the radio path. Utilizing the Propsound channel sounder (PSCS) and frequency conversion blocks in both ends, 200 MHz wideband measurements at the centre frequency of 17.6 GHz were carried out in Austria in the late summer of 2009. Qualitative analysis of the data has been carried out, and parameters for a Markov type model are currently being extracted.

This activity has been carried out under the ESA Contract C20871 – Propagation Effects for Mobile Multimedia Services under ARTES 5.

MEASUREMENT CAMPAIGN

The aircraft flew along equi-centred circles at various elevations carrying onboard the PSCS, a 420 W high-power tube amplifier (HPA), an uninterruptible power system and a Nitrogen source for de-moisturizing the TX waveguide. The TX antenna was mounted under the fuselage in a fixed tilt to compensate the aircraft bank angle during the circles. This ensured that the receiver van, and the RX antenna on its roof, was kept within the HPBW of the TX antenna. Fig. 1 shows the overall route planning.

Elevation angles at 20, 40 and 60 degrees were chosen to give data for an elevation dependency study. The link lengths were nominally 10 km from the preselected centre points on the ground. Deviation of the RX vehicle from the centre point of the trajectory brings a radial speed component into the radio link between the aircraft and the van. This causes a Doppler shift, and therefore the routes were carefully designed not to exceed the operational limits of the measurement system.

Four radio environments were chosen to consider typical scenarios as needed for the channel modelling. Fig. 2 gives a bird's eye view to the actual routes travelled by the measurement van. The railroad scenario was substituted by a trolley-bus scenario with similar installations for electricity. All four routes were selected in or close to the city of Linz / Austria.

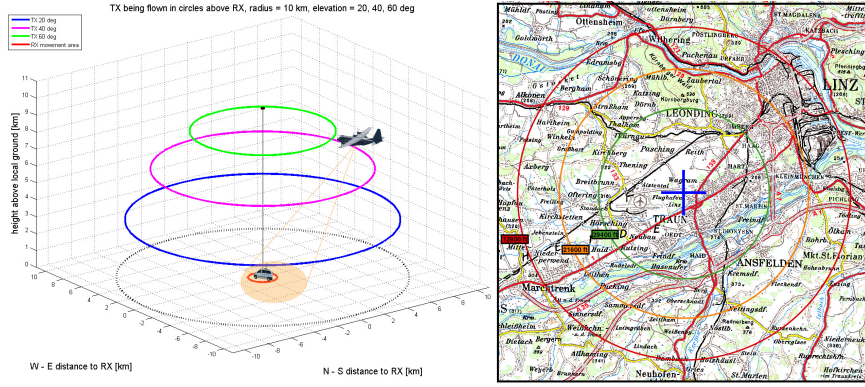


Fig. 1: Measurement configuration:
Left: Schematic view, Right: Flight plan for Rural scenario.

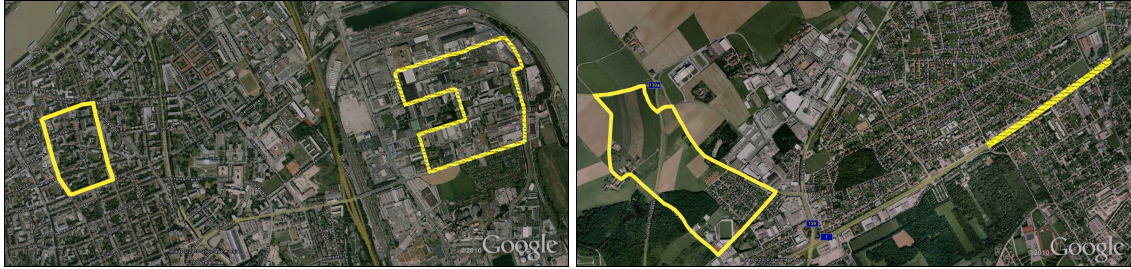


Fig. 2: Measurement routes in Linz (Scenarios from left to right):
Urban, Suburban, Rural, Railroad.

The rural scenario included open passages, a road through the forest, an underpass and a road through a residential area. The suburban scenario was located within an industrial park, characterized by a dense arrangement of flat houses and storages along the road. The urban scenario measurements took place in the very centre of Linz, with narrow street canyons formed by houses of four or more storeys. The trolley-bus scenario was by a four-lane road, with vertical concrete pylons in the middle and sturdy horizontal metallic bars carrying the electricity installations above the lanes.

Fig. 3 shows how the strong signal received in an open area drops into a ‘bad state’ when the RX enters an underpass, and then fluctuates between the two states while the route is in a forested area. The large change cannot be described by a single distribution [1]. A better result is achieved with a state-oriented approach, where at least two distributions are applied to describe the good and bad signal states.

DATA ANALYSIS

In our approach we apply Rice and Rayleigh distributions for the good and bad signal states, respectively. Rice distributed signal amplitude is defined as [2]

$$p_{\text{Rice}}(r|a) = \frac{r}{\sigma^2} \exp\left[-\frac{r^2 + a^2}{2\sigma^2}\right] I_0\left(\frac{ra}{\sigma^2}\right) \quad r \geq 0, \quad (1)$$

where r is the mean signal amplitude, a is the direct path amplitude, σ^2 is the variance of the real and imaginary parts of the signal amplitude, and I_0 is the modified Bessel function of the first kind and zeroth order. With $a=0$, this becomes a Rayleigh distribution.

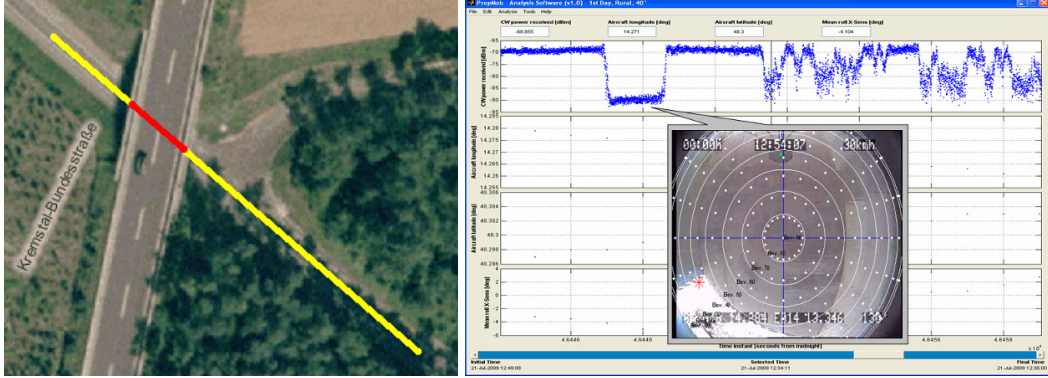


Fig. 3: Measured signal level changes in the rural scenario.

The satellite channel is modelled as a two-state Markov chain, where the channel states are determined by the Rice factor $k = a^2 / (2\sigma^2)$. For the modelling purposed, we split k into parameters $A = 20 \lg a$, representing the *direct signal power*, and $MP = 10 \lg 2\sigma^2$, which describes the normalised *diffuse multipath power* caused by the direct signal illuminating the environment in the vicinity of the mobile.

The data was analysed in two steps. In the first step, the *instantaneous power delay profiles* (PDP) $p_i(\tau)$ were averaged over $d=0.5$ meter portions of movement to yield *average PDPs* (APDP). At 17.6 GHz, distance d equals to 29.3 wavelengths, which in terms of mobile radio channel can still be considered as small-scale. As defined by (2), PDP is the squared amplitude of the input delay spread function $h_i(\tau)$ (the ‘complex impulse response’, CIR) at time instant i , cut at a given signal level to mask out the reflections from distant scatterers

$$p_i(\tau) = |h_i(\tau)|^2. \quad (2)$$

The channel state parameters A , MP and the state transition probabilities, and their dependency of elevation angle are to be extracted from the APDPs by studying the evolution of the average power delay profile over distance travelled by the RX van.

In the second step, the APDPs are fitted into an exponential decay function (a linear ramp in dB scale). The exponential decay is described by the total signal power P_0 and the delay spread τ_{rms} along the delay τ as

$$P(\tau) = \frac{P_0}{\tau_{\text{rms}}} \exp\left(-\frac{\tau}{\tau_{\text{rms}}}\right), \quad (3)$$

The delay spread τ_{rms} is calculated using definition (4) [2].

$$\tau_{\text{rms}} = \sqrt{\frac{1}{P_T} \sum_{i=1}^N \tau_i^2 P(\tau_i) - \tau_0^2}, \quad (4)$$

where $P(\tau_i)$ is the received power at delay τ_i , and P_T is the total received power. The mean excess delay τ_0 is defined by

$$\tau_0 = \frac{1}{P_T} \sum_{i=1}^N P(\tau_i) \tau_i . \quad (5)$$

Preliminary RESULTS

The mutual dependency of the channel state parameters A and MP are depicted in Fig. 4.

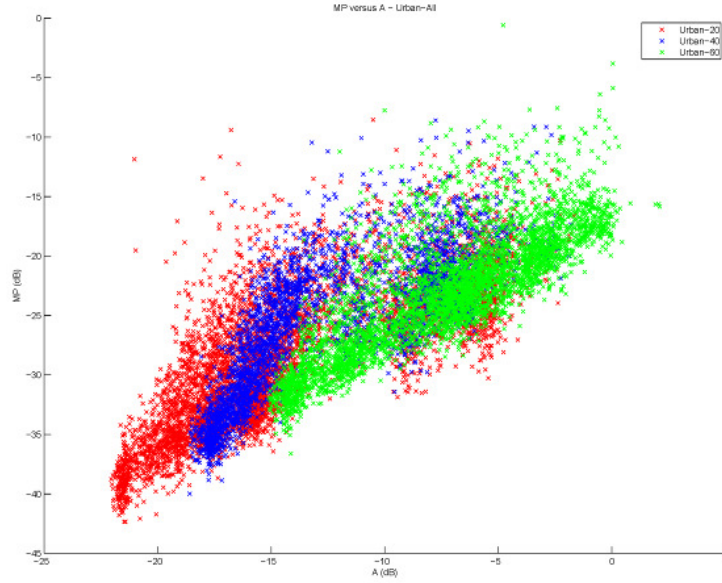


Fig. 4: Parameters for Rice distributed signal.

CONCLUSIONS

A unique radio channel measurement campaign has been carried out at 17.6 GHz to gain increased knowledge of LMS signal propagation at Ku- and Ka-band. The recorded data quality is excellent and when mapped on the real environment the signal shows plausible behaviour. Channel simulator development is currently being constructed based on these data.

REFERENCES

- 1 Fernando Pérez Fontán, P. Mariño Espiñeira, *Modeling the Wireless Propagation Channel*. John Wiley & Sons Ltd, 2008, 252 pages.
- 2 Simon R. Saunders, Alejandro Aragón-Zavala, *Antennas and propagation for Wireless Communication Systems*. John Wiley & Sons Ltd, England, 2007, 524 pages.

ANALYTICAL LINK DISTANCE DERIVATIONS FOR 3D CO-CHANNEL INTERFERENCE SCENARIOS

Pekka Pirinen

*Centre for Wireless Communications, P.O. Box 4500, FI-90014 University of Oulu,
FINLAND*

Email: pekka.pirinen at ee.oulu.fi

INTRODUCTION

Co-channel interference is one of the fundamental limiting factors for the radio capacity of wireless systems. Femtocells [1] have gained a lot of interest lately as an effective solution to increase spectral efficiency. Femtocells need also to cope with interference (originating, e.g., from other femtocells and macrocells in the neighborhood). Paper [2] presented simulation based co-channel co-existence performance evaluation between indoor femtocells and a co-located macrocell. This contribution complements those studies with applicable analytical link distance models.

LINK DISTANCE DISTRIBUTIONS IN 3D INDOOR LAYOUT

Monte Carlo simulations are often used for averaging performance over, e.g., spatial geometry variations. Typically simulations require a high number of realizations, i.e., high complexity to be statistically accurate enough. From the computational point of view the closed-form analytical models are preferable whenever available. Here the link distance probability density functions (PDFs) are solved analytically for the case of having multiple square-shaped (femto)cells next to each other as shown in Fig. 1. Following the principle that link distance PDF is equal to the arc length normalized by the sectional area [3], and after some trigonometry and geometry exercises, the distance from AP23 in Fig. 1 to user planes in cells numbered by 0–5 can be solved and expressed as

$$p_0(d) = \begin{cases} \frac{2\pi d}{a^2}, & x_0 \leq d \leq x_1, \\ \frac{2\pi d}{a^2} - \frac{8d}{a^2} \cos^{-1} \left(\frac{a}{2\sqrt{d^2 - h^2}} \right), & x_1 < d \leq x_2, \end{cases} \quad (1)$$

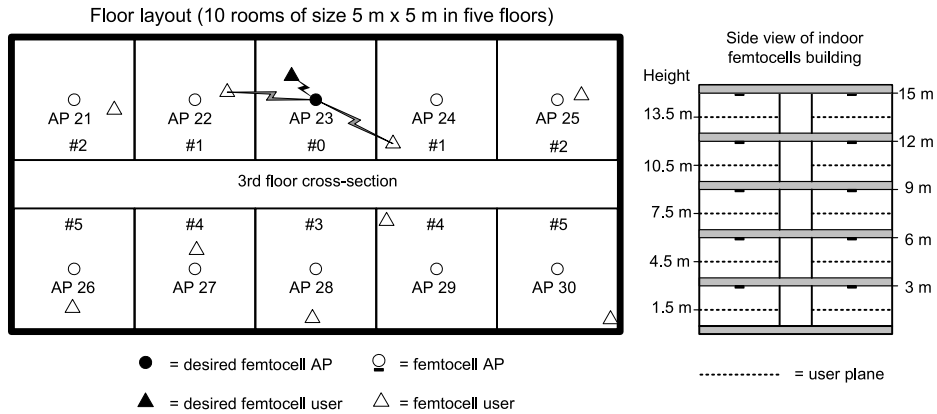


Figure 1: Floor layout for the femtocells.

$$p_1(d) = \begin{cases} \frac{2d}{a^2} \cos^{-1} \left(\frac{a}{2\sqrt{d^2-h^2}} \right), & x_1 \leq d \leq x_2, \\ \frac{2d}{a^2} \sin^{-1} \left(\frac{a}{2\sqrt{d^2-h^2}} \right), & x_2 < d \leq x_5, \\ \frac{2d}{a^2} \left[\sin^{-1} \left(\frac{a}{2\sqrt{d^2-h^2}} \right) - \cos^{-1} \left(\frac{3a}{2\sqrt{d^2-h^2}} \right) \right], & x_5 < d \leq x_6, \end{cases} \quad (2)$$

$$p_2(d) = \begin{cases} \frac{2d}{a^2} \cos^{-1} \left(\frac{3a}{2\sqrt{d^2-h^2}} \right), & x_5 \leq d \leq x_6, \\ \frac{2d}{a^2} \sin^{-1} \left(\frac{a}{2\sqrt{d^2-h^2}} \right), & x_6 < d \leq x_{11}, \\ \frac{2d}{a^2} \left[\sin^{-1} \left(\frac{a}{2\sqrt{d^2-h^2}} \right) - \cos^{-1} \left(\frac{5a}{2\sqrt{d^2-h^2}} \right) \right], & x_{11} < d \leq x_{12}, \end{cases} \quad (3)$$

$$p_3(d) = \begin{cases} \frac{2d}{a^2} \cos^{-1} \left(\frac{a/2+2}{\sqrt{d^2-h^2}} \right), & x_3 \leq d \leq x_4, \\ \frac{2d}{a^2} \sin^{-1} \left(\frac{a}{2\sqrt{d^2-h^2}} \right), & x_4 < d \leq x_8, \\ \frac{2d}{a^2} \left[\sin^{-1} \left(\frac{a}{2\sqrt{d^2-h^2}} \right) - \cos^{-1} \left(\frac{3a/2+2}{\sqrt{d^2-h^2}} \right) \right], & x_8 < d \leq x_9, \end{cases} \quad (4)$$

$$p_4(d) = \begin{cases} \frac{d}{a^2} \left[\cos^{-1} \left(\frac{a/2+2}{\sqrt{d^2-h^2}} \right) - \sin^{-1} \left(\frac{a}{2\sqrt{d^2-h^2}} \right) \right], & x_4 \leq d \leq x_7, \\ \frac{d}{a^2} \left[\sin^{-1} \left(\frac{3a}{2\sqrt{d^2-h^2}} \right) - \sin^{-1} \left(\frac{a}{2\sqrt{d^2-h^2}} \right) \right], & x_7 < d \leq x_9, \\ \frac{d}{a^2} \left[\sin^{-1} \left(\frac{3a}{2\sqrt{d^2-h^2}} \right) - \cos^{-1} \left(\frac{3a/2+2}{\sqrt{d^2-h^2}} \right) \right], & x_9 < d \leq x_{10}, \end{cases} \quad (5)$$

$$p_5(d) = \begin{cases} \frac{d}{a^2} \left[\cos^{-1} \left(\frac{a/2+2}{\sqrt{d^2-h^2}} \right) - \sin^{-1} \left(\frac{3a}{2\sqrt{d^2-h^2}} \right) \right], & x_7 \leq d \leq x_{10}, \\ \frac{d}{a^2} \left[\sin^{-1} \left(\frac{3a/2+2}{\sqrt{d^2-h^2}} \right) - \sin^{-1} \left(\frac{a/2+2}{\sqrt{d^2-h^2}} \right) \right], & x_{10} < d \leq x_{13}, \\ \frac{d}{a^2} \left[\sin^{-1} \left(\frac{3a/2+2}{\sqrt{d^2-h^2}} \right) - \cos^{-1} \left(\frac{5a}{2\sqrt{d^2-h^2}} \right) \right], & x_{13} < d \leq x_{14}, \end{cases} \quad (6)$$

where d denotes distance, a is the side length of the square cell, h is the height difference between link ends, and limits $x_i, i = 0, \dots, 14$ are defined in Table 1.

Fig. 2 shows one floor link distance PDFs according to (1)–(6) with $h = 1.5$ m. Fig. 3 depicts the corresponding cumulative distribution functions (CDFs) that can be realized by integrating PDF over the whole distance range. For further numerical analyses or simulations it is now possible to select, e.g., worst, median or best case link distances as 0th, 50th or 100th percentiles of CDFs.

Finally, Fig. 4 gives an example how the analytical link distance models relate to the Monte Carlo simulation based approach in pure femtocell interference limited scenario. Averaged random snapshot simulation and 40th percentile link distance CDF provide close match whereas extremes illuminate the expected range of performance variations.

References

- [1] V. Chandrasekhar, J. G. Andrews, and A. Gatherer, “Femtocell networks: a survey,” *IEEE Commun. Mag.*, vol. 46, pp. 59–67, Sep. 2008.
- [2] P. Pirinen, “Co-channel co-existence study of outdoor macrocell and indoor femtocell users,” in *Proc. European Wireless 2010 Conference (EW'10)*, Lucca, Italy, Apr. 2010, pp. 207–213.
- [3] S. W. Oh and K. H. Li, “Effect of circular-cell approximation on the forward-link BER performance of a power-controlled CDMA system,” in *Proc. IEEE Global Telecommunications Conference (Globe-com'99)*, Rio de Janeiro, Brazil, Dec. 1999, pp. 2472–2476.

Table 1: Distances in (1)–(6).

Distance	Value	Example: ($a = 5, h = 1.5$)
x_0	h	1.50
x_1	$\sqrt{\frac{a^2}{4} + h^2}$	2.92
x_2	$\sqrt{\frac{a^2}{2} + h^2}$	3.84
x_3	$\sqrt{\frac{a^2}{4} + 2a + 4 + h^2}$	4.74
x_4	$\sqrt{\frac{a^2}{2} + 2a + 4 + h^2}$	5.36
x_5	$\sqrt{\frac{9a^2}{4} + h^2}$	7.65
x_6	$\sqrt{\frac{5a^2}{2} + h^2}$	8.05
x_7	$\sqrt{\frac{5a^2}{2} + 2a + 4 + h^2}$	8.87
x_8	$\sqrt{\frac{9a^2}{4} + 6a + 4 + h^2}$	9.62
x_9	$\sqrt{\frac{5a^2}{2} + 6a + 4 + h^2}$	9.94
x_{10}	$\sqrt{\frac{9a^2}{2} + 6a + 4 + h^2}$	12.20
x_{11}	$\sqrt{\frac{25a^2}{4} + h^2}$	12.60
x_{12}	$\sqrt{\frac{13a^2}{2} + h^2}$	12.84
x_{13}	$\sqrt{\frac{13a^2}{2} + 2a + 4 + h^2}$	13.37
x_{14}	$\sqrt{\frac{17a^2}{2} + 6a + 4 + h^2}$	15.77

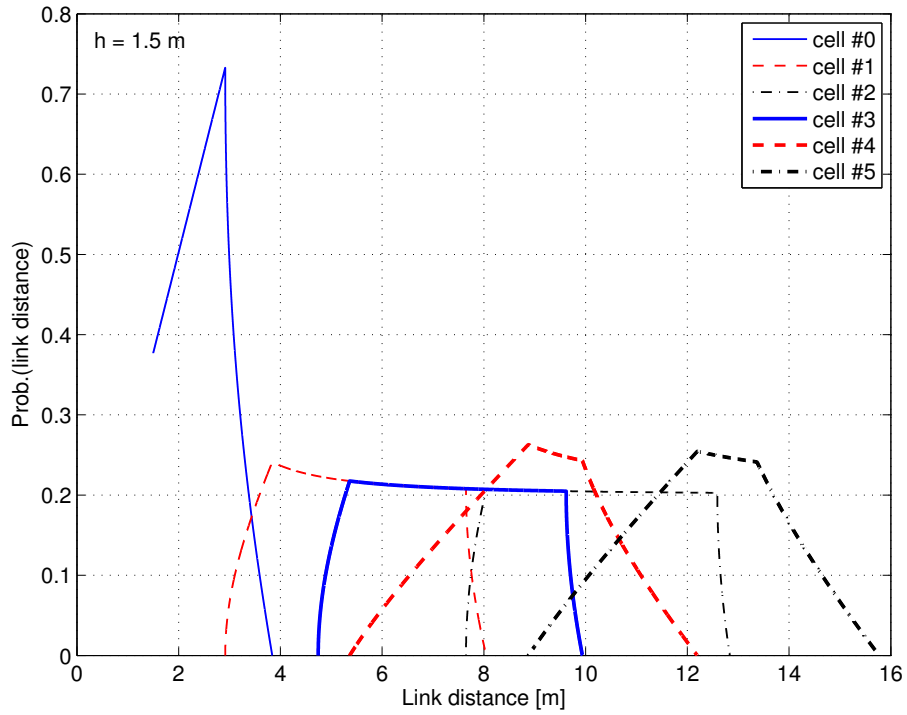


Figure 2: Probability density functions of interference link distances.

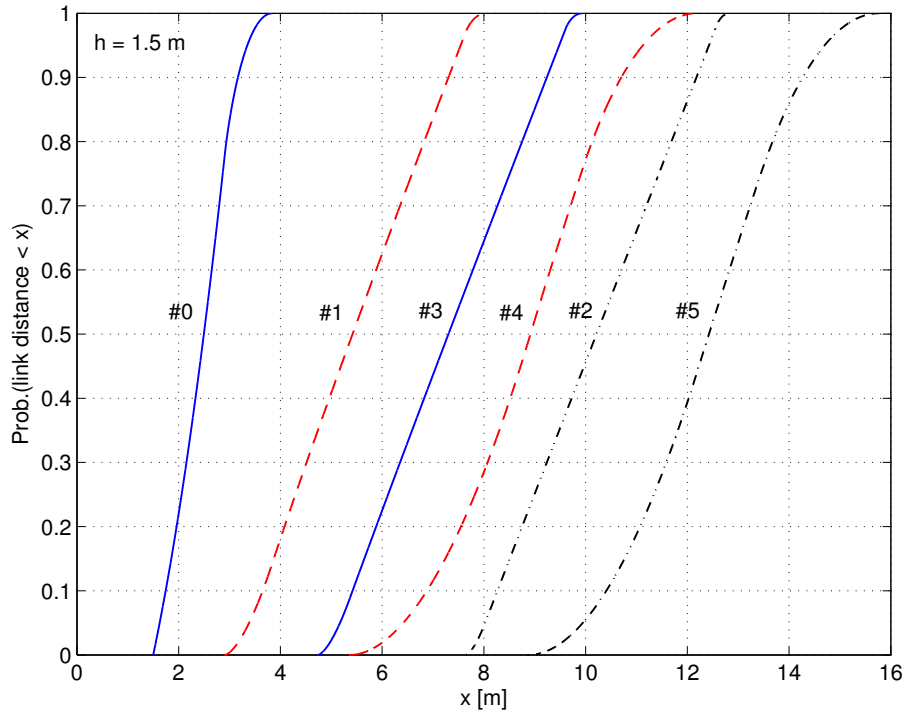


Figure 3: Cumulative distribution functions of interference link distances.

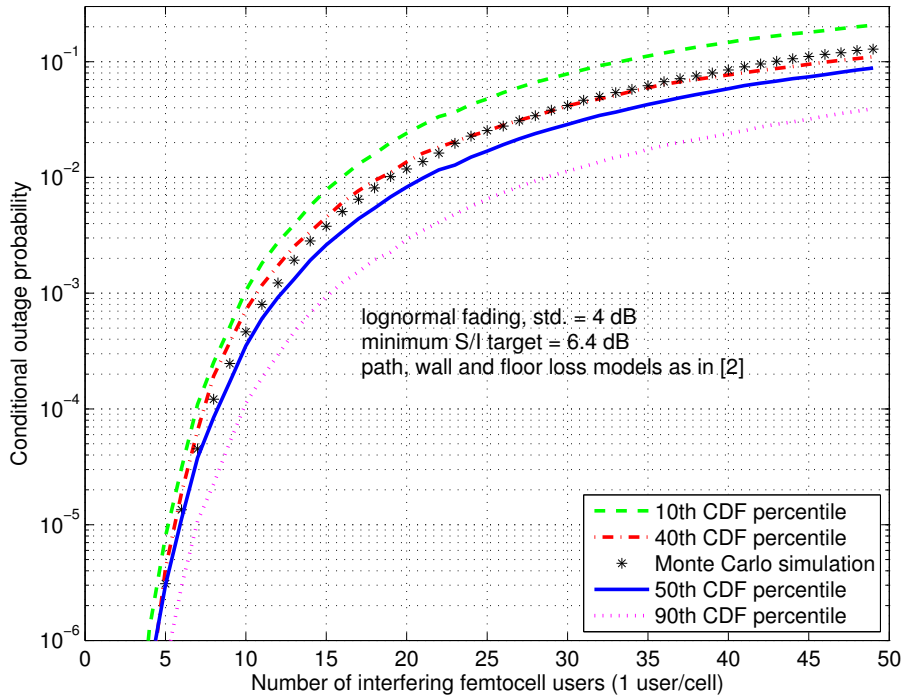


Figure 4: Femtocell interference limited conditional outage probability of the desired link.

Session B2

Two-Hop Relaying in LTE-A Downlink

Timo Prokkola ⁽¹⁾

⁽¹⁾ *Centre for Wireless Communications, University of Oulu
P.O. Box 4500 FI-90014 University of Oulu, Finland
Email: timopro@ee.oulu.fi*

INTRODUCTION

The third generation (3G) long term evolution advanced (LTE-A) standard is a part of the Third Generation Partnership Project (3GPP) and it is the next evolution step of LTE. The 3G LTE-A standard requires a higher signal-to-noise ratio (SNR) than is typically experienced in widearea cellular networks to be able to use higher order modulation and coding schemes. A long distance between a transmitter and a receiver causes high path loss and thereby the required SNR levels cannot be reached. To improve the SNR and achieve cost-effective throughput enhancement and coverage extension, different layers of relaying have been introduced in the LTE-A framework. A wide range of relay types can be envisioned, ranging from simple repeaters, which are already used today as a low cost tool for coverage improvement, to more advanced solutions where the relay can be seen as a small base station [1]. Three different layers of relaying are proposed for LTE-A: layer-1 (repeater), layer-2 (relay) and layer-3 (wireless router). Layer-1 supports a simple amplify-and-forward (AF) protocol and layers two and three support the decode-and-forward (DF) protocol. [1, 2]

The main focus will be on a fixed relay station and non-cooperative types of relaying where the destination does not hear the source. The fixed relay station is one possible solution to achieve the target SNR and data rates in LTE-A. The relaying system corresponds to a two-hop communication system where the relay is assumed to be placed on a rooftop to ensure line of sight (LOS) conditions toward the base station. The relay-to-terminal link is also assumed to be a LOS channel. The cell size of the relay station can be described as an urban microcell, which models one possible scenario.

RELAY PROTOCOLS

The main focus is on layer-1 AF and layer-2 DF relaying protocols, since they present the most known relay types. Also other relaying protocols exist but most of them have complexities higher than the AF relay but lower than the DF relay.

Linear amplification is the only operation that the AF relay does for the received signal. Basically, the received signal is multiplied by a gain matrix and then forwarded to the destination. The received signal at the destination contains following parts.

$$\mathbf{y}_2 = \mathbf{H}_2 \mathbf{G} \mathbf{H}_1 \mathbf{x}_1 + \mathbf{H}_2 \mathbf{G} \mathbf{n}_1 + \mathbf{n}_2 \quad (1)$$

In (1), \mathbf{y}_2 denotes the received signal vector at the destination, \mathbf{H}_2 denotes the channel matrix of the channel between the relay station (RS) and the destination, \mathbf{G} denotes the amplification matrix at the RS, \mathbf{H}_1 denotes the channel matrix of the channel between the source and the RS, \mathbf{x}_1 denotes the transmitted signal vector from the source, \mathbf{n}_1 denotes the noise vector at the RS, \mathbf{n}_2 denotes the noise vector at the destination. In (2), it can

be seen that the overall noise at the destination is $\mathbf{n}_{\text{tot}} = \mathbf{H}_2 \mathbf{G} \mathbf{n}_1 + \mathbf{n}_2$. The total impact of the channels is needed to be estimated at the destination since the signal goes through two channels. The total channel matrix between source and destination is $\mathbf{H}_{\text{tot}} = \mathbf{H}_2 \mathbf{G} \mathbf{H}_1$, which consists of both channel matrixes and the amplification matrix. [3, 4]

The more complex DF relay protocol includes signal processing such as demodulation, decoding, encoding and modulation. The biggest advantage compared to layer-1 relays is that no noise is amplified and DF relays can suppress noise from the received signal. The transmitted signal does not contain any additional degradation and the DF relay can modify the decoded signal before transmission. A DF relay can change modulation, coding scheme and transmit power for every transmission. The destination does not need CSI of the first channel because it assumes that the relay successfully decodes the source signal. There is no point in forwarding erroneous bits if decoding fails. The DF relay requests retransmission and tries to decode again after maximum ration combining, if decoding fails. The same kind of HARQ schemes as at the base station and the terminal can be used in DF relays. [2, 5]

SYSTEM MODEL

The work is focused on the single user link-level perspective. Different transmission and relaying schemes are analyzed by the simulations in terms of various error ratios and throughput outcomes. The effect of other terminals and cells are not taken into account. The basic two-hop system model describes the behavior of the source, relay and destination. The simulator is mainly designed for the LTE standard but since LTE-A is backwards compatible with LTE the main structure is the same. In throughput calculations, all information bits are discarded and not counted in if at least one frame error is detected in the received transmission time interval (TTI) block which can be seen in Fig. 1. The used frame structure does not correspond to the LTE frame structure.

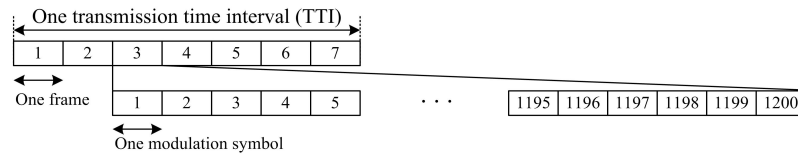


Figure 1: Structure of TTI block.

Perfect channel state information (CSI) and level of AF relay gain are assumed to be known at the destination. Simulations with the AF protocol are made with three different gains: nine and half decibels SNR gain, six decibels SNR gain and the last one does not provide any SNR gain. The link between the base station and the relay station is called the relay link and the link between the relay station and the terminal is called the access link in this work. Channel variations are continuous for the entire duration of the simulations and different SNR values are used in the access link to model different kinds of scenarios. The channel model between the source and the relay is based on the Wireless World Initiative New Radio (WINNER) B5a cluster delay line (CDL) channel model parameters and the channel between the relay and the destination is based on the WINNER B1 CDL channel model parameters [6]. The main simulation parameters used can be seen from Tab. 1.

SIMULATION RESULTS

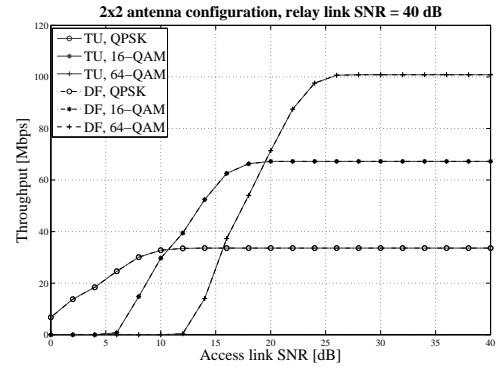
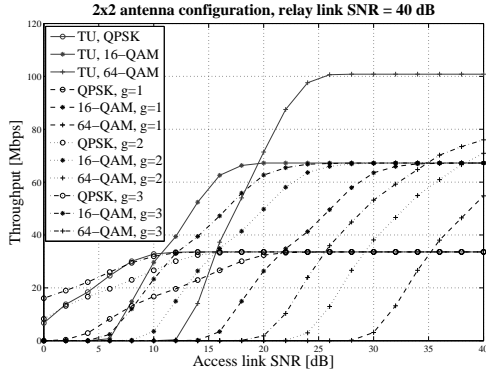
The simulation results for the AF and DF relaying systems with access link performance are presented in the following figures. Simulation results for an AF relay with a 2×2 antenna configuration and a 40 dB SNR in the relay link are presented in Fig. 2. A 40 dB SNR in the relay link is enough for QPSK and 16-QAM modulations but 64-QAM

Table 1: Simulation parameters

Carrier Frequency	5 GHz
Bandwidth	20 MHz
Number of/used subcarriers	2048/1200
Modulation schemes	QPSK, 16-QAM, 64-QAM
Channel code	Turbo coding
Code rate	1/2
MIMO scheme	VBLAST, Spatial multiplexing
Terminal speed	120 km/h
Detector type	List sphere detector K-BEST
HARQ scheme	Chase combining
Maximum number of retransmissions	3
Number of simulated frames	10000

modulation cannot reach the maximum throughput with any gain. An AF relaying system can improve throughput with nine and half decibels SNR gain compared to access link results when access link SNR is between zero and six decibels. The simulation results for a DF relay with a 2×2 antenna configuration and a 40 dB SNR in the relay link are presented in Fig. 3. A 40 dB SNR in the relay link is enough for all modulation schemes in DF relaying and the DF relay does not cause any additional degradations.

The simulation results for an AF relay with a 4×4 antenna configuration and a 50 dB SNR in the relay link are presented in Fig. 4 and the corresponding simulation results for the DF relay are presented in Fig. 5. The impact of noise amplification and forwarding can especially be seen with higher level transmission schemes like 64-QAM and 4×4 antenna configuration. DF relaying can also in this case offer the same throughput with the same SNR values as the access link. The access link channel simulation results are also plotted in the figures, but they equal to those of DF relaying and are therefore under DF relaying results.

Figure 2: AF relaying throughput in 2×2 .Figure 3: DF relaying throughput in 2×2 .

CONCLUSIONS

The AF and DF relaying protocols were assumed to behave differently since the impact of the relay on the system makes a major difference. Simulations confirm the assumption that an AF relay suffers from noise amplification and forwarding. More vulnerable higher order modulation and coding schemes do not reach the same performance with an AF relay than with a DF relay. Higher antenna configurations also affect AF relaying performance by increasing the required SNR in both links. When adequate conditions in the relay link can be guaranteed, the AF relay offers higher throughput with 2×2 and

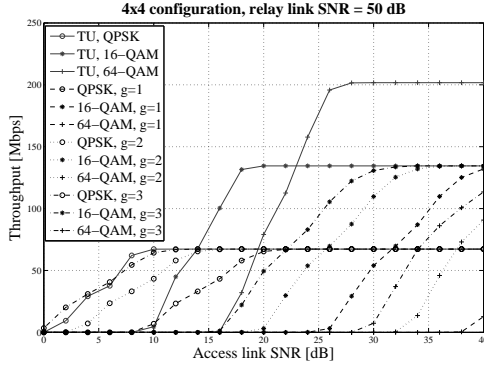


Figure 4: AF relaying throughput in 4×4 .

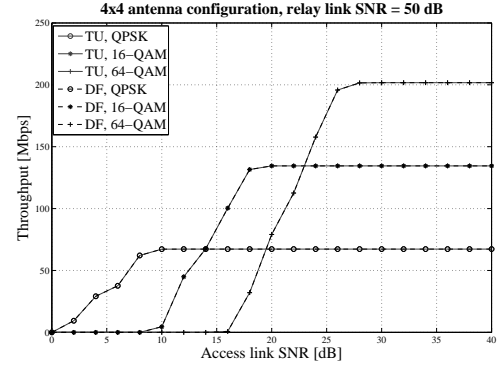


Figure 5: DF relaying throughput in 4×4 .

4×4 antenna configurations and QPSK modulation with low SNR levels in the access link than DF relaying. The AF relay can amplify the received signal and therefore the signal is stronger at the destination with AF relaying. In other cases, DF relaying achieves the maximum throughput with a lower SNR value in the access link than AF relaying. A DF relaying does not offer similar SNR gain, but in good enough conditions relaying corresponds to access link performance. Overall AF relaying system performance can be increased by using higher gains. When using higher gains, the relay also needs higher transmission power and therefore amplification is limited. The main reasons for the performance differences are noise amplification in the AF relay and the DF relay offering coding gain in both links.

The relay link limits total system performance with both relay types when it cannot offer the maximum throughput. In the case of AF relaying, the total noise levels increases too much and the destination cannot decode successfully, although HARQ retransmissions are used. In the case of DF relaying, the DF relay does not transmit anything to the destination if the relay cannot decode successfully. The relay link is more important than the access link for all relaying protocols since the operator can affect relay link conditions.

References

- [1] Dahlman E., Parkvall S., Sköld J. & Beming P. (2008) 3G Evolution, HSPA and LTE for Mobile Broadband. Academic Press is an imprint of Elsevier, second ed.
- [2] Peters S., Panah A., Truong K. & Heath Jr R. (2009) Relay Architectures for 3GPP LTE-Advanced. EURASIP Journal on Wireless Communication and Networking 2009.
- [3] Ma J., Orlik P., Zhang J., Kuze T., Iura H. & Li G. (2009) Static Power Allocation in Two-Hop MIMO Amplify-and-Forward Relay Systems. In: Proceedings of the IEEE Vehicular Technology Conference, pp. 1–5.
- [4] Juan Z., Sartori P. & Wei B. (2009) Performance Analysis of Layer 1 Relays. In: Proceedings of the IEEE International Conference on Communications, pp. 1–6.
- [5] Zheng K., Hu L., Wang W. & L. H. (2009) Performance Analysis of HARQ Transmission in Cooperative DF Relaying Systems. In: Wireless Pers Commun, Springer Science+Business Media, LLC. 2009, pp. 1–15.
- [6] Kyösti P. (2007) WINNER II Channel Models (D1.1.2 V1.2 IST-4-027756 WINNER II). URL:<http://www.ist-winner.org>.

An Efficient Close to Optimal Radio Resource Allocation Mechanism towards LTE Downlink Transmission

Pradeep Chathuranga Weeraddana⁽¹⁾
Marian Codreanu⁽¹⁾ and Matti Latva-Aho⁽¹⁾

⁽¹⁾ *Affiliation*

*Centre for Wireless Communications, P.O. Box 4500, FI-90014 University of Oulu, Finland.
Email: chathuranga.weeraddana@ee.oulu.fi*

INTRODUCTION

Long Term Evolution (LTE) is the well known radio access technology specified by one of the global standards developing organization, the Third Generation Partnership Project (3GPP)[1]. In this paper we consider a problem of radio resource allocation (RA) which can be adapted towards RA for LTE downlink transmission. Since the LTE downlink transmission scheme is based on Orthogonal Frequency Division Multiple Access (OFDMA), we abstract the main problem in to a radio RA problem in an OFDMA system. OFDMA plays a major role in the physical layer specifications of future wireless technologies which is not confined to LTE (e.g., WIMAX, IMT-A) [2]. In general OFDMA based transmission systems, the transmit power and sub-carriers are dynamically assigned to the users, based on their channel state information (CSI) to optimize a certain performance. Indeed this process requires solving combinatorial optimization problems.

The main contribution of this paper is to provide a low complexity very close to optimal resource allocation algorithm for joint optimization of multiuser subcarrier assignment and power allocation which is a simple extension of our previous work [3]. Numerical results are provided to compare the performance of the proposed algorithm to Lagrange relaxation based suboptimal methods [4] as well as to optimal exhaustive search based method. We did not consider each and every fine details of the LTE time/frequency domain structures of the frames which is out of the scope of the main concern. But the proposed solution method indeed can be used as a basic building block for more general resource allocation algorithms for practical LTE downlink transmissions after having appropriate modifications.

SYSTEM MODEL AND PROBLEM FORMULATION

Consider a single antenna OFDMA downlink transmission with K users and M subcarriers. The signal received by user k in subcarrier m can be expressed as

$$r_{km} = h_{km}x_{km}\sqrt{p_{km}} + w_{km}, \quad k = 1, \dots, K, \quad m \in \mathcal{S}_k, \quad (1)$$

where k is the user index, m is the subcarrier index, \mathcal{S}_k denotes the set of subcarriers allocated to user k , x_{km} is the transmitted signal, p_{km} is the power allocated, h_{km} is channel frequency response and w_{km} is the received noise. We assume that h_{km} is time-invariant and its value is available at the base station. The noise samples are assumed to be independent and identically distributed as $w_{km} \sim \mathcal{CN}(0, \sigma_{km}^2)$. We denote by $c_{km} = \frac{|h_{km}|^2}{\sigma_{km}^2}$ the channel signal-to-noise ratio (SNR) of k th user in subcarrier m and by β_k the weight associated with the rate of user k . The weighted sum-rate maximization problem subject to a sum-power constraint P_T can be formulated as [3]

$$\begin{aligned} & \text{maximize} && \sum_{k=1}^K \sum_{m \in \mathcal{S}_k} \beta_k \log_2(1 + p_{km}c_{km}) \\ & \text{subject to} && \sum_{k=1}^K \sum_{m \in \mathcal{S}_k} p_{km} = P_T \\ & && \mathcal{S}_k \cap \mathcal{S}_l = \emptyset, \quad \forall k \neq l \\ & && p_{km} \geq 0, \quad k = 1, \dots, K, \quad m = 1, \dots, M, \end{aligned} \quad (2)$$

where variables are p_{km} and \mathcal{S}_k .

APPROXIMATED PRIMAL DECOMPOSITION BASED ALGORITHM

By considering an equivalent virtual system and introducing M new variables $\bar{p}_m = \sum_{k=1}^K p_{km}$, $m = 1, \dots, M$, problem (2) can be decomposed into a master problem and M subproblems, one subproblem for each subcarrier $m = 1, \dots, M$ [3]. For a given subcarrier m , the subproblem is given by

$$\begin{aligned} & \text{maximize} && \sum_{k=1}^K \beta_k \log_2 \left(1 + \frac{p_{km}}{\bar{p}_m - p_{km} + c_{km}^{-1}} \right) \\ & \text{subject to} && \sum_{k=1}^K p_{km} = \bar{p}_m \\ & && p_{km} \geq 0, \quad k = 1, \dots, K, \end{aligned} \quad (3)$$

where variables are p_{km} , $k = 1, \dots, K$. The master problem can be expressed as

$$\begin{aligned} & \text{maximize} && \sum_{m=1}^M f_m^*(\bar{p}_m) \\ & \text{subject to} && \sum_{m=1}^M \bar{p}_m = P_T \\ & && \bar{p}_m \geq 0, \quad m = 1, \dots, M, \end{aligned} \quad (4)$$

where variables are \bar{p}_m and $f_m^*(\bar{p}_m)$ represents the optimal value of subproblem (3) for fixed \bar{p}_m . Let us denote by \mathcal{P} the feasible set of problem (3). Even though the subproblem (3) is not a convex optimization problem, from [5, Corollary 32.3.4] it follows that the solutions of subproblems (3) must be achieved at one of the vertices of the polyhedral set \mathcal{P} . Consequently, the solutions of the M subproblems can be expressed as

$$[p_{1m}^*, \dots, p_{Km}^*] = \bar{p}_m \mathbf{e}_{j_m}^T, \quad j_m = \arg \max_k (1 + \bar{p}_m c_{km})^{\beta_k}, \quad m = 1, \dots, M. \quad (5)$$

where j_m represents the index of the user allocated to m th subcarrier. By substituting (5) in the objective of (3), $f_m^*(\bar{p}_m)$ can be expressed as

$$f_m^*(\bar{p}_m) = \beta_{j_m} \log_2 (1 + \bar{p}_m c_{j_m m}) = \max_k \beta_k \log_2 (1 + \bar{p}_m c_{km}), \quad m = 1, \dots, M. \quad (6)$$

Note that the function $f_m^*(\bar{p}_m)$ is the pointwise maximum of a set of concave functions and thus $f_m^*(\bar{p}_m)$ is not a concave function w.r.t \bar{p}_m [6] in general. Thus, standard convex optimization tools (e.g., subgradient based methods) can not be directly applied to solve master problem (4). The trick is to use the following concave lower bound on the objective function of problem (4) so that approximated master problem is solved optimally.

$$\sum_{m=1}^M \beta_{j_m^{(i)}} \log_2 \left(1 + \bar{p}_m c_{j_m^{(i)} m} \right) \leq \sum_{m=1}^M f_m^*(\bar{p}_m), \quad [\bar{p}_1, \dots, \bar{p}_M]^T \in \bar{\mathcal{P}} \quad (7)$$

Thus, the proposed algorithm can be summarized as follows:

Algorithm 1 *Approximated primal decomposition for OFDMA weighted sum-rate maximization with parallel initializations*

1. *initialization: Given the number of random initialization points N_{rand} . Let $i = 1$ and $l = 0$.*

(a) *Uniform power init.: $\bar{p}_m^{(i)}(0) = P_T/M$, $m = 1, \dots, M$*

(b) *Random power init: $\bar{p}_m^{(i)}(l) = \mathcal{U}(0,1) \cdot P_T/M$, $m = 1, \dots, M$, $l = 1, \dots, N_{rand}$, where $\mathcal{U}(0,1)$ is a random number which is uniformly distributed between 0 and 1.*

2. *if $l \leq N_{rand}$ go to step 3, otherwise go to step 6.*

3. *solve the M subproblems (3) for $\bar{p}_m = \bar{p}_m^{(i)}(l)$ and return $j_m^{(i)}(l)$, computed according to (5). Let $j_m^{(i)} = j_m^{(i)}(l)$ and $g = \sum_{m=1}^M \beta_{j_m^{(i)}} \log_2 \left(1 + \bar{p}_m c_{j_m^{(i)} m} \right)$.*

4. solve the following approximation of master problem (4)

$$\begin{aligned} & \text{maximize} && \sum_{m=1}^M \beta_{j_m^{(i)}} \log_2 \left(1 + \bar{p}_m c_{j_m^{(i)} m} \right) \\ & \text{subject to} && \sum_{m=1}^M \bar{p}_m = P_T \\ & && \bar{p}_m \geq 0, \quad m = 1, \dots, M, \end{aligned} \quad (8)$$

and return the solution \bar{p}_m^* ; let $\bar{p}_m^{(i+1)}(l) = \bar{p}_m^*$ and $g^*(l) = \sum_{m=1}^M \beta_{j_m^{(i)}} \log_2 \left(1 + \bar{p}_m^* c_{j_m^{(i)} m} \right)$.

5. check a stopping criteria $g^*(l) = g$:

(a) if the stopping criteria is not satisfied let $i = i + 1$ and go to step 3.

(b) otherwise store the power allocation $\bar{p}_m^{(i+1)}(l)$, subcarrier allocation $j_m^{(i)}(l)$, and the associated objective value of problem (8) $g^*(l)$ for l th iteration, let $l = l + 1$ and go to step 2.

6. Choosing the best power and subcarrier allocation:

$$l^* = \arg \max_{l \in \{0, \dots, N_{\text{rand}}\}} f^*(l). \quad (9)$$

choose the power allocation and the subcarrier allocation stored in Step 5(b) which are associated with l^* .

The solution of problem (8) solved at step 3 is found by multilevel waterfilling (see [3] for more details).

NUMERICAL RESULTS

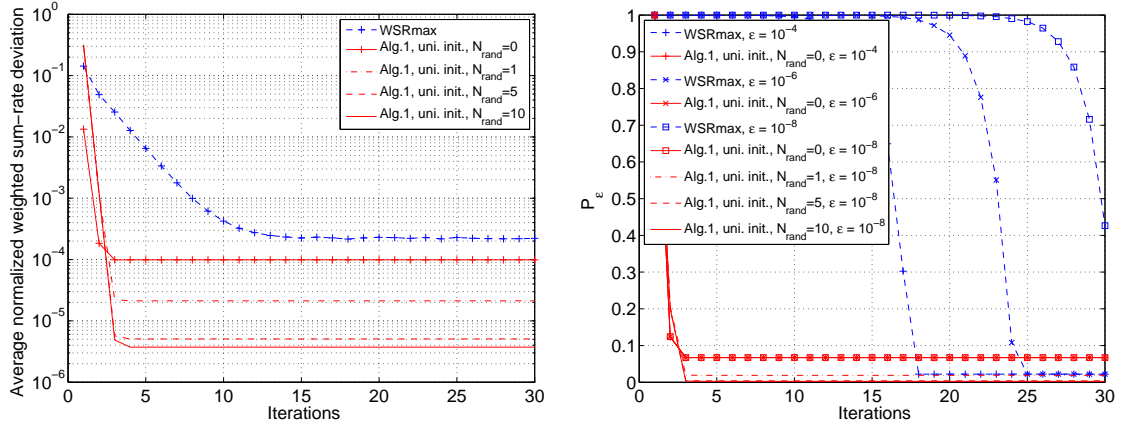
The performance of the proposed algorithm is compared to the dual decomposition based algorithm proposed in [4], denoted as WSRmax, as well as to the optimal algorithm based on exhaustive search. For a fair comparison, we first define the metric $\Delta C_{\text{weighted sum}} = \mathbb{E} \left\{ \frac{|C_{\text{opt}} - \hat{C}_{\text{subopt}}|}{C_{\text{opt}}} \right\}$, the average normalized weighted sum-rate deviation (ANWSRD), where, C_{opt} is the optimal weighted sum-rate value obtained using optimal exhaustive search, \hat{C}_{subopt} is the estimated objective value from either Algorithm 1 or the WSRMax algorithm and expectation $\mathbb{E}\{\cdot\}$ is taken w.r.t channel realization. Since for large M the computational complexity of optimal exhaustive search is prohibitively expensive. Thus, in our simulations we considered a small scale OFDMA system with $M = 8$ subcarriers and $K = 2$ users. It should be emphasized that this limitation is solely for the comparison purpose of Algorithm 1 with the optimal solution and not a limitation of our Algorithm 1. A uniform power delay profile with 4 channel taps is considered. We assume $\sigma_{km}^2 = \sigma^2, k = 1, \dots, K, m = 1, \dots, M$ and define SNR per subcarrier as $\frac{P_T}{M \cdot \sigma^2}$.

Figure 1(a) shows the convergence behavior of the considered algorithms with SNR= 10dB for $N_{\text{rand}} = 0, 1, 5$ and 10. The weights of the users are [1, 2]. The floor of the curves is due to the suboptimality of the algorithms. The results show that Algorithm 1 converges faster than the WSRMax algorithm and provides smaller values of ANWSRD. Specifically, for any value of N_{rand} Algorithm 1 requires only 3 iterations on average to achieve a constant level of ANWSRD whilst the WSRMax algorithm requires around 15 iterations to reach a constant level. Even with just uniform initialization (i.e., the case of $N_{\text{rand}} = 0$) the ANWSRD values achieved by proposed algorithm is smaller as compared to that of WSRMax algorithm. Remarkable reduction of ANWSRD is obtained when N_{rand} is changed from 0 to 1. As N_{rand} increased the incremental gains that can be obtained in terms of ANWSRD is reduced.

Then we compare the behavior of Algorithm 1 and the WSRMax algorithms using the following metric $P_\epsilon = \text{Prob} \left\{ |C_{\text{opt}} - \hat{C}_{\text{subopt}}| > \epsilon \right\}$, the probability of missing the global optimal, where ϵ is a small number which quantifies the maximum admissible deviation between C_{opt} and \hat{C}_{subopt} . It is considered that the global optimum is missed if \hat{C}_{subopt} is more than ϵ away from C_{opt} .

Figures 1(b) uses the same simulation setup as that in Figure 1(a) and depict the variation of probability of missing the global optimal, P_ϵ with the number of iterations. The floor of probability

P_ε is again due to the suboptimality of both algorithms. The influence of ε on P_ε for fixed N_{rand} ($= 0$) is totally indistinguishable in case of proposed algorithm. This behavior shows that the proposed algorithm can arrive very close to optimal solutions within a very small number of iterations and then it remains there. The results further show that the P_ε evaluated using the WSRMax algorithm is highly dependent on ε . That is, the smaller the deviations in the \hat{C}_{subopt} from the optimal C_{opt} , the larger the number of iterations required by the WSRMax algorithm to reach the expected target value P_ε . However, independent from the ε , proposed Algorithm 1 allows to find a suboptimal solution within a small number of iterations. Results further show that as the number of parallel initialization points are increased, P_ε become almost zero. This confirms that most of the time our proposed algorithm find the optimal solution.



(a) Average normalized weighted sum-rate deviation vs. Iterations for $K = 2$ users, $M = 8$ subcarriers and SNR = 10dB. (b) Probability of missing global optimum vs. Iterations for $K = 2$ users, $M = 8$ subcarriers and SNR = 10dB.

CONCLUSIONS

A joint subcarrier and power allocation algorithm has been proposed for maximizing the weighted sum-rate in multiuser OFDMA downlink systems which can be used as a building block for more general resource allocation algorithms for *long term evolution* downlink transmissions. The proposed solution method is an simple extension of our previous work [3] and the algorithm is based on an approximated primal decomposition based method. The original nonconvex optimization problem is divided into two subproblems which can be solved independently. Numerical results show that, despite its reduced computational complexity, the proposed algorithm provides very close to optimal performance.

References

- [1] E. Dahlman, S. Parkvall, J. Sköld, and P. Beming, *3G evolution: HSPA and LTE for mobile broadband*, Academic Press is an imprint of Elsevier, Linacre House, Jordan Hill, Oxford, 1 edition, 2007.
- [2] S. Sesia, I. Toufic, and M. Baker, *LTE - the UMTS long term evolution*, A John Wiley and Son publication, UK, 2009.
- [3] C. Weeraddana, W. Li, M. Codreanu, and M. Latva-aho, "Weighted sum-rate maximization for downlink OFDMA systems," in *Proc. Annual Asilomar Conf. Signals, Syst., Comp.*, Pacific Grove, California, Oct. 2008, pp. 990–994.
- [4] K. Seong, M. Mohseni, and M. Cioffi, "Optimal resource allocation for OFDMA downlink systems," in *Proc. IEEE Int. Symp. Inform. Theory*, Seattle, USA, Jul. 2006, pp. 1394–1398.
- [5] R. T. Rockafellar, *Convex Analysis*, Princeton, N.J., Princeton University Press, 1970.
- [6] S. Boyd and L. Vandenberghe, *Convex Optimization*, Cambridge University Press, Cambridge, UK, 2004.

TCP Performance over Geostationary Satellite Link

Jouko Vankka

Finnish Army Signal School

PL 5, 11311 Riihimäki, Finland, Email: jouko.vankka at mil.fi

INTRODUCTION

A significant amount of today's Internet traffic, including WWW (HTTP), file transfer (FTP), e-mail (SMTP), and remote access (Telnet) traffic, is carried by the TCP (Transmission Control Protocol) transport protocol [1]. Geostationary satellite links have a number of characteristics that may degrade the performance of TCP over it. The satellite links have an average RTT (round trip time) of around 500ms. The TCP uses the slow start mechanism to probe the network at the start of a connection. Time spent in slow start stage is directly proportional to the RTT and for a satellite link, it means that the TCP stays in slow start mode for a longer time than in the case of a small RTT link. This drastically decreases the throughput of short duration TCP connection. Furthermore, when packets are lost, the TCP enters the congestion control phase, and due to higher RTT, remains in this phase for a longer time, thus reducing the throughput of both short and long duration TCP connections.

TCP satellite gateways are proven to improve TCP throughput across high delay and lossy satellite links. The satellite gateways can improve TCP performance across stressed environments by breaking the end-to-end TCP connection into multiple transport layer connections [2].

RESULTS

To analyze the performance of the TCP satellite gateway, we conducted a variety of experiments using both the link emulator as well as the geostationary satellite link. We used the link emulator because of the limited testing time allowed with the satellite link and also because of the flexibility. The results demonstrate that improvements can be made to enhance the performance of TCP over satellite links through the satellite gateways. On the average, the satellite gateways introduce the significant improvement of up to 300 – 800 % in throughput.

References

- [1] T. R. Henderson, and R. H. Katz, "Transport Protocols for Internet-Compatible Satellite Networks", IEEE Journal on Selected Areas of Communications, Vol. 17, No. 2, pp. 345-359, February 1999.
- [2] K. Scott, P. Feighery, B. Crow, and M. Jurik, "TCP congestion control in shared satellite environments", MILCOM 2002 - IEEE Military Communications Conference, no. 1, October 2002, pp. 46 – 50.

Session B3

PUETTAVA RADIOTAAJUINEN TUNNISTEANTENNI

Tiiti Kellomäki ⁽¹⁾

Toni Björninen ⁽²⁾

Leena Ukkonen ⁽²⁾

Lauri Sydänheimo ⁽²⁾

⁽¹⁾ *Tampereen teknillinen yliopisto, Elektroniikan laitos
Pl. 692, 33101 Tampere
Email: tiiti.kellomaki at tut.fi*

⁽²⁾ *Tampereen teknillinen yliopisto, Rauman tutkimusyksikkö
Kalliokatu 2, 26100 Rauma*

JOHDANTO

Radiotaajuinen tunnistustekniikka (RFID) ja etäluettavat kulkukortit ovat tulleet jokapäiväiseen käyttöön. Nykyisissä järjestelmissä on hyvin yleisesti käytössä HF-tunniste, jonka lukuetaisyys on muutamia millimetrejä. Tällainen kortti on käytännössä pidettävä esillä ja asetettava erikseen lukijaan.

866 MHz:n alueella toimiva UHF-tunniste voidaan lukea useiden metrien päästä. Ovet voidaan siis avata kulkijalle ilman, että hänen itsensä tarvitsee tehdä mitään. Myös avonaisesta ovesta kulkevat voidaan rekisteröidä ja tarvittaessa paikantaa.

Vanhustenhoidosta karkailevat dementikkopotilaat vaativat jatkuvaa valvontaa. Paloturvallisuussyistä ovia ei kuitenkaan yleensä voida pitää lukittuina. Vaatteeseen tai rannekeeseen yhdistetyn RFID-tunnisteen avulla ovi voitaisiin asettaa hälyttämään, mikäli potilas pyrkii ulos. Karkulainen olisi näin mahdollista saada kiinni jo ennen kuin hän pääsee pois vanhainkodin pihalta.

Tässä julkaisussa esitellään RFID-tunnisteantenni, joka on tarkoitettu liitettäväksi vaatteeseen. Tunnisteen pituus on 68 mm ja leveys 22 mm, ja se mahtuu esimerkiksi paidan kaulukseen. Tunniste on passiivinen eli siinä ei ole omaa teholahtetta.

TUNNISTEANTENNI

Puettavan tunnisteantennin muoto ja mitat esitellään kuvassa 1. Pohjimmiltaan antenni on taivuteltu dipoli. Koska metallointia tarvitaan vain yhdelle puolelle kangasta, on tämä antenni helppo yhdistää vaatteeseen. Antenni ei myöskään vaadi piirilevymateriaaleja, vaan se on suunniteltu toimimaan tavallisella kangasalustalla, jonka dielektrisyysvakio on noin 1–1,5.

Koska säteilevän elementin ja käyttäjän välillä ei ole metallikerrosta eli maatasoa, pitää antennin ja käyttäjän väliin jäädä käytössä vähintään viiden millimetrin rako. Esimerkiksi kovakauluksisen paidan kaulus on yleensä vähintään senttimetrin päässä solisluusta, ja muuallakin vaatteiden väljyysvara on vähintään viiden millimetrin luokkaa.

Jotta antenni toimisi RFID-tunnisteena, on siihen kiinnitettävä mikrosiru. Antenni on suunniteltu käyttämään Alien H3 strap'ia [1], jonka impedanssi on $(16-j150) \Omega$ Euroopan UHF-RFID-taajuuskaistan keskitaajuudella (866 MHz). Antenni on konjugaattisovitettu sirun impedanssiin lisäämällä sen syöttöpisteen induktanssia T-sovituksen avulla [2].

Antennin käyttötaajuuden määrää sen kokonaispituus mukaan lukien ympyröiden kaaret. T-sovitus eli syöttöpisteen rinnalla kulkeva ohut liuska lisää induktanssia: mitä pidempi

T-sovitus, sitä suurempi induktanssi. Antennin kaistanleveyttä voidaan lisätä käyttämällä leveitä johdinventoja.

Vapaassa tilassa antennin sovitus on tarkoituksella huono. Kehon lähellä syöttöpisteimpedanssi ja resonanssitaajuus laskevat, ja näin tunnisteeseen paras toiminta saadaan 866 MHz:n kaistalle.

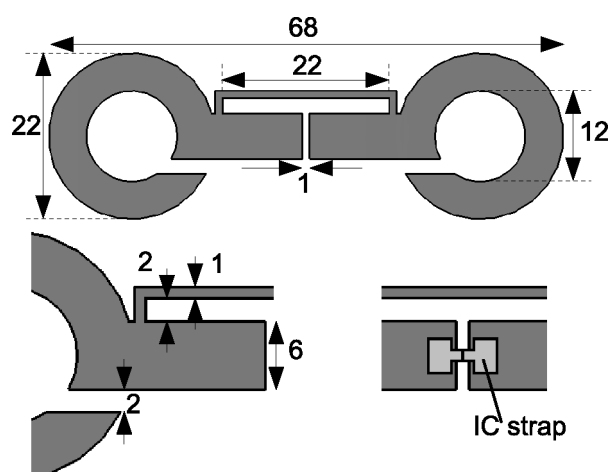
MITTAUSTULOKSIA

Antennin toimintaa on mitattu RFID-lukijalaitteella. Kaikissa mittauksissa antenniin on liitetty mikrosiru. Mitatuissa vahvistuksissa on siis mukana epäsovitushäviö sirun sisäänmenoimpedanssiin eli kyseessä on IEEE:n määrittelemä ”realised gain”. Mittauksissa antennin etäisyys kehosta oli 4–60 mm. Lukijalaite oli 1,6 metrin etäisyydellä.

Kehon lähellä antennin sähköinen pituus kasvaa, koska kehon dielektrisyysvakio on korkea (kudoksesta riippuen 10–55). Samalla hyötysuhde heikkenee rajusti, sillä keho absorboi suuren osan säteilytehosta. Molemmat ilmiöt ovat nähtävissä mitatusta vahvistuskäyrästä jokseenkin erillisinä: sähköisen pituuden muutos liikuttaa käyrää oikealta vasemmalle, hyötysuhteen pieneneminen puolestaan ylhäältä alas.

Kehon lähellä antennin impedanssi voi pienentyä jopa puoleen samalla, kun resonanssitaajuus pienenee. Resonanssitaajuuden muutos luonnollisesti pienentää käyttötaajuutta, mutta impedanssin pieneneminen kompensoi tätä, koska mikrosirun impedanssi ei ole taajuuden suhteen vakio, vaan sekä reaali- että imaginääriosan itseisarvo pienenee taajuuden kasvaessa. Esitetyn antennirakenteen käyttötaajuus pienenee siis kehon etäisyyden funktiona vähemmän kuin pelkkä resonanssitaajuus.

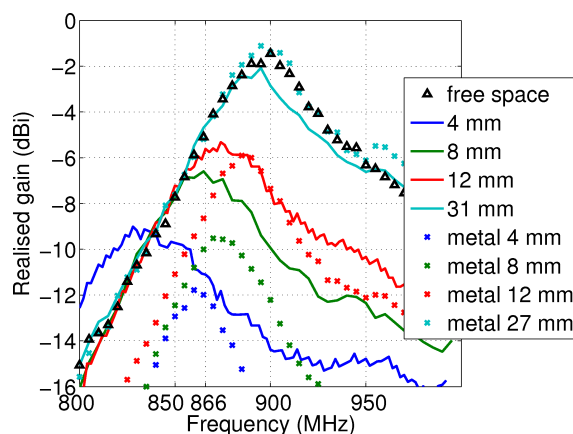
Mittauksissa havaittiin, että tunnisteantenni soveltuu parhaiten käytettäväksi yli 1 cm:n etäisyydellä kehosta. Kuvassa 2 on esitetty mitattu vahvistus, käyräparametrina antennin etäisyys kehosta. Yhden senttimetrin etäisyydellä, 866 MHz:n taajuudella, tunniste voidaan lukea viiden–seitsemän metrin päästä lukijan maksimiteholla (2 W ERP). Luku-etäisyys on yli kolme metriä silloinkin, kun antenni on 4 mm:n päässä kehosta. Antennin alle ei siis tarvita erillistä toppausta.



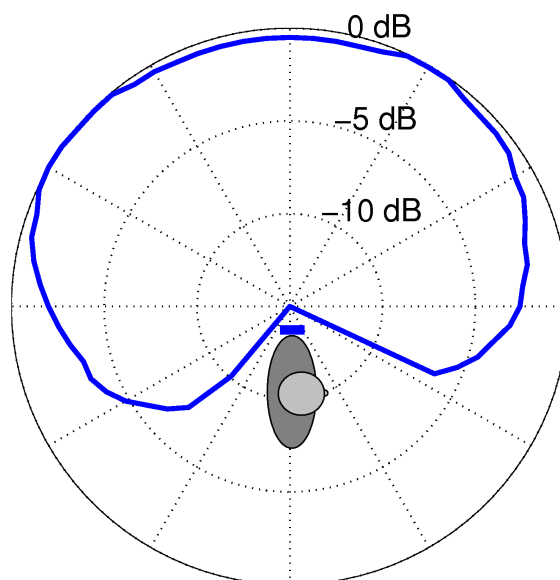
Kuva 1: Tunnisteantennin mitat millimetreinä. Antennissa on metallia vain yhdellä puolella alustaa, ja alustana voidaan käyttää mitä tahansa kangasta. Mikrosiru (IC) on strap'in keskellä. Huomaa, että viitteessä [3] T-sovituksen pituus on virheellisesti 12 mm; oikea arvo on 22 mm.

Kun antennin etäisyys kehosta on 3 cm, antennin impedanssi on sama kuin vapaassa tilassa. Kun etäisyyttä kasvatetaan tästä, kehosta heijastuva ja suoraan etenevä aalto alkavat vahvistaa toisiaan niin, että antennin vahvistus kasvaa yli vapaan tilan arvon.

Antennin säteilykuvio H-tasossa eli vaakatasossa mitattiin sekä vapaassa tilassa että olkavarrelle puettuna. Mittauksissa antenni oli pystyssä. Etäisyys kehosta oli mittauksessa 8 mm, ja säteilykuvion muodon voidaan olettaa olevan samanlainen etäisyydestä riippumatta. Kuva 3 osoittaa, miten puolen tehon keila kattaa puoli avaruutta. Tunniste ei ole luettavissa kehon takaa, mutta se voidaan lukea ranteen läpi. Vapaassa tilassa antennin H-tason säteilykuvio on suuntaamaton.



Kuva 2: Mitattu impedanssiepäsovituksen huomioiva vahvistus. Mittauksissa tunniste on käyttäjän olkavarrella, metallilevyn päällä tai vapaassa tilassa. Tunnisteen lopullinen käyttöaajuus on 866 MHz. Mustavalkolukijoille: käyrät vasemmalta oikealle vastaavat selitteen kohtia ylhäältä alas.



Kuva 3: Mitattu normalisoitu H-tason (vaakataason) säteilykuvio. Antenni on käyttäjän olkavarrella 8 mm:n etäisyydellä kehosta. Tunnistetta ei voida lainkaan lukea kehon läpi.

Antennin paikka keholla ei vaikuta sen impedanssiin eikä parhaan sovituksen taajuuteen. Olkavarrelle sijoitetun antennin vahvistus on 1–1,5 dB suurempi kuin vartalon päällä olevan antennin (kaulus, selkä, rintakehä). Olkavarrella keho absorboi vähemmän tehoa.

Suurinta lukuetaisyyttä varten antenni kannattaa sijoittaa olkavarteen. Jos säteilykuvioista halutaan suuntaamaton, ranne on parempi paikka. Ranteeseen sijoitetun antennin asento vaihtelee kuitenkin jatkuvasti, ja lukijalaitteelta vaaditaankin polarisaatiodiversiteettiä. Polarisaatioepäsovitushäviö voidaan minimoida kiinnittämällä antenni kaulukseen.

Antennin toimintaa tutkittiin myös, kun se oli lähellä metallia. Mittaustulokset on esitetty kuvassa 2. Kehoon verrattuna metalli aiheuttaa vähemmän pieleenvirittymistä. Antennin kaistanleveys pienenee metallin lähellä. Tunniste on luettavissa myös metallin lähellä, mutta se toimii varsin heikosti. Mittauksissa kehoa ei voida mallintaa metallilevyllä, vaan on käytettävä joko koehenkilöä tai sopivalla nesteellä täytettyä phantomia.

LOPUKSI

Työssä on esitelty tunnisteantenni Euroopan UHF-RFID-kaistalle (866 MHz). Kun tunniste on yhden senttimetrin päässä kehosta, se voidaan lukea 5–7 metrin etäisyydeltä. Antennin ominaisuudet eivät muutu merkittävästi, kun sen etäisyys kehosta muuttuu. Antennin alle ei ole tarpeen laittaa erillistä toppausta. Antenni toimii myös vapaassa tilassa.

Antennin pituus on 68 mm ja leveys 22 mm. Se mahtuu erinomaisesti esimerkiksi paidan kaulukseen, kalvosimeen tai jopa nappilistaan nappien väliin.

Lisää mittaustuloksia on esitetty julkaisussa [3].

KIITOKSET

DI Juha Virtanen ansaitsee suurkiitokset autettuaan mittauksissa ja käytännön ongelmissa. DI Timo Kellomäki ja tekn. yo. Joel Salmi auttoivat mittauksissa.

GETA-tutkijakoulu (Graduate School in Electronics, Telecommunication and Automation) rahoitti Tiiti Kellomäen työtä.

Kirjallisuutta

- [1] Alien Technology. (2009, Dec.) Higgs-3 product overview. [Online]. Available: http://www.alientechnology.com/docs/products/DS_H3.pdf
- [2] G. Marrocco, "The art of UHF RFID antenna design: impedance-matching and size-reduction techniques," *IEEE Antennas Propagat. Mag.*, vol. 50, pp. 66–79, Feb. 2008.
- [3] T. Kellomäki, T. Björninen, L. Ukkonen, and L. Sydänheimo, "Shirt collar tag for wearable UHF RFID systems," in *Proc. European Conf. on Antennas and Propagation, 2010*, 12–16 Apr. 2010, Barcelona, Spain.

Energy Savings in Mobile Networks: Case Study on Femtocells

M. Jada, J. Hämäläinen, R. Jäntti

*Department of Communications and Networking
Aalto University, School of Science and Technology
Espoo, Finland*

E-mail: mjada at cc.hut.fi, jyri.hamalainen at tkk.fi, riku.jantti at tkk.fi

INTRODUCTION

Mobile networks do not have considerable share in the overall energy consumption of the ICT (Information and Communication Technology) sector, which itself is responsible for 2% to 10 % of the world energy consumption. However, reduction in energy consumption of mobile networks is of great importance from economical (cost reduction) and environmental (decreased CO₂ emissions) perspective.

This paper presents first a discussion on different energy saving aspects in mobile networks. Then a case study on the impact of femtocells to the energy efficiency of WCDMA networks is given.

ENERGY SAVING ASPECTS IN MOBILE NETWORKS: PREVIOUS STUDIES

A. Background

Recently, the mobile communication community has become aware of large and ever-growing energy usage of mobile networks [1]. Besides industry the awareness of ever-increasing energy consumption has been growing also on academic research [2],[3],[4],[5],[6],[7].

A typical mobile network consists of three main elements: core network, base stations, and mobile terminals. Base stations contribute 60% to 80% of the whole network energy consumption. Thus the efforts in the reduction of energy consumption focus on the BS equipment, which includes the minimization of BS energy consumption, minimization of BS density and use of renewable energy sources [8].

The ways to minimize the BS energy consumption includes improvement in BS energy efficiency through better performance of BS hardware, usage of system level and software features, and usage of BS site solutions like fresh air cooling systems for indoor networks. One of the main energy saving approaches is the system level feature in which underutilized cells (BS's) are switched off whenever traffic load is small.

When cells are switched off, it is assumed that the radio coverage and feasible service conditions can be guaranteed by the remaining active cells (BS's), probably with some increment in the BS transmitting power. This increase in transmission power in remaining active BSs, however, can be small when compared to the savings achieved by switching off some BS sites.

B. BS switching in conventional macrocell topology

Energy saving through BS switching was used in [5] where proposed power saving algorithms can be centralized (when all the channel information and traffic requirements are known) or decentralized (no such information required). Energy savings are higher in

This work was prepared in Advanced Wireless Access (AWA) and Energy and Cost Efficiency for Wireless Access (ECEWA) project frameworks, and supported in part by Finnish Funding Agency for Technology and Innovation (Tekes), Ericsson Finland, Nokia Siemens Networks, Efore and European Communications Engineering.

centralized approach because BS density becomes lower, while coverage guarantee is better in decentralized approach because more BS's stay active. In [5] the focus was on the relation between BS energy saving and load balancing. Through examination it was found out in [5] that load balancing appears to be important BS energy saving algorithm due to its decentralized and dynamic nature.

Similar approach was applied in [4] where focus was in cell layout. To achieve optimal energy saving it was discovered that in real networks only a small fraction of cells need to remain on during the night time. In [4] few typical cellular network configurations (Manhattan/linear; Manhattan/squared; Hexagonal; Hexagonal/squared; Crossroad) had been compared assuming two different daily traffic patterns. Comparison indicates that the best solution is not to switch off the largest possible number of cells; rather it is important to make tradeoff between the low traffic period and the number of cells that are switched off. According to this paper for example, the best performing scheme is switching off 4 cells out of 5 with crossroad configuration.

C. *Impact of femtocells to the network energy efficiency*

We continue part of the study of [7] in this paper. It is shown that femtocells may reasonably decrease the network energy consumption but only if femtocells are deactivated when indoor traffic is nonexistent. Thus, femtocell should be capable of sensing the traffic and adjusting its mode (activate or deactivate) following the traffic conditions. Along with this feature femtocell can enter sleep mode when there is no indoor traffic. The importance of this feature is obvious from the fact that if a number of femtocells remain active when traffic is nonexistent, then network energy consumption increases accordingly.

CASE STUDY: IMPACT OF FEMTOCELLS TO THE WCDMA NETWORK ENERGY EFFICIENCY

A. *Modeling and comparison scenario*

We recall a simple model that was proposed in [7] to describe the daily energy consumption per square kilometer in the network:

$$\begin{aligned} (E / A)_{Nrw} = & \frac{N_{Site}^{New} \cdot N_{Cell} \cdot (P_{Oper} + \lambda^{New} \cdot P_{Tx})}{N_{Site} \cdot A_{Site}} \cdot 24h \\ & + \frac{N_{Cell} \cdot N_F \cdot P_F}{A_{Site}} \cdot 24h \end{aligned} \quad (1)$$

Thus, dimension for the performance is the kWh/km². The area covered by a three-sector site is given by $A_{Site} = 9/4 \cdot R^2 = ISD^2$. Here we present only one comparison scenario that offers more energy saving in network than the other scenario as in [7]. In the above equation, number of sites in new deployment and corresponding load λ^{New} refer to the new parametric values of the modified network with respect to the old parametric values of the reference network. Either of these changes is expected to take place in one of the two compared networks as in [7] depending upon the scenario. In order to make calculations more concrete we adopt from [4] the UMTS macrocell base station specific values $P_{oper}=137W$ and $P_{TX}=57W$, which will be then used in comparison. For femto BS input power we use two values, 2W and 5W. The former value is optimistic but reachable in future while latter value is already reality in products [9].

Comparison scenario: Assume that the macrocell ISD is not fixed but instead, we fix the target load in macrocells. Since femtocells offload part of the traffic, the required number of macrocell BS's is decreasing due to cell breathing [3] and we have,

$$(E / A)_{Ntw} = \frac{N_{Site}^{New} \cdot N_{Cell} \cdot (P_{Oper} + \lambda \cdot P_{Tx})}{N_{Site} \cdot A_{Site}} \cdot 24h + \frac{N_{Cell} \cdot N_F \cdot P_F}{A_{Site}} \cdot 24h \quad (2)$$

B. Numerical comparison

For comparisons we first carry out dimensioning of the network without femtocells and calculate daily energy consumption per square kilometer. When N_F femtocells are added to the system they take a certain portion of the users, say $(R_{femto} \cdot 100)$ % of users (R_{femto} is the ratio between femtocell and macrocell connections). Then number of macrocell sites is decreasing, thus reducing the energy consumption of the network. When comparison scenario is analyzed in case of the femtocells deployment that do not possess power save feature, we assume any fixed number of femtocells that remain active throughout the R_{femto} scale. We consider 64kbps service and initial system load 0.9. Other information besides service rate and load in (1) can be obtained from link budget in [7].

Utilizing equation (2), results regarding comparison scenario has been plotted in Fig.1 from energy saving perspective for both types of femtocells (with and without power save feature) having input power of 2W and 5W. Plotted curves show that total energy saving is more when deployed femtocell possess power save feature in comparison to the situation when they do not have such feature. In Fig.1 different symbols are used to differentiate the variuos plots depicting total energy saving in different conditions. For the case with $N_F = N_{users}$ we have used; Circle for the condition when femtocells with 2W input power possess power save feature, Triangle (Up) when femtocells with 2W input power do not possess power save feature, Asterisk (*) when femtocells with 5W input power possess power save feature, Traingle (Down) when femtocells with 5W input power do not possess power save feature. Similarly in case of $N_F = 2.3 \times N_{users}$ we have used; Square when femtocells with 2W input power possess power save feature.

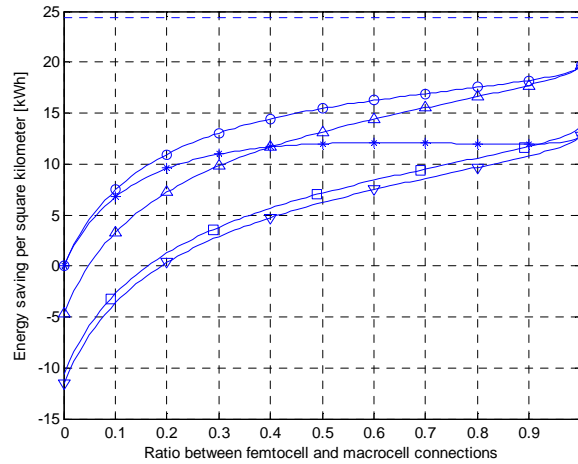


Figure 1: Daily energy saving per square kilometer in the network for comparison scenario .

We observe from plots of both input powers of femto BS; when more load out of full load gets shifted from macrocell to femtocell, approximately same amount of energy can be saved from both types of femtocell deployment (with and without power save feature). This figure explains that femtocells without power save feature would be more unfavourable when not much load of the macrocell is shifted to femtocell i-e during situation when there is not much indoor traffic existing in the network.

With input power of 2W, when femtocells that do not possess power save feature are deployed in the network, there will be extra energy consumed (no energy saving) by the network until R_{femto} reaches 0.05 since femto base station energy consumption is easily overtaking the achieved savings on the macrocell side. Whereas in case of the 5W femto BS, extra energy is consumed by the network until R_{femto} reaches 0.2, and this extra energy will be more than the extra energy consumed in case of 2W femto BS.

Therefore in case of 2W input power, the deployment of femtocells that do not possess power save feature could be acceptable if femtocells possessing this feature are unavailable. However in case of 5W input power, this femtocell feature is necessarily required.

Moreover, we vary the number of active femtocells (2W) in the network as for example $N_F = 2.3 \times N_{\text{users}}$, then the energy saving gets reduced. It is concluded through analysis that number of femtocells should be limited and upper bound to it is the number of users in the macrocell i-e N_F (*Upper bound*) = N_{users} , for both types of femtocells (with and without power save feature). Thus the maximum gain in energy saving will be achieved with $N_F = N_{\text{users}}$.

References

- [1] Emerson: “Energy Logic for Telecommunication”, *white paper, Ericsson, 2008*.
- [2] F. Richter, A. J. Fehske, G. P. Fettweis: “Energy Efficiency Aspects of Base Station Deployment Strategies for Cellular Networks”, *IEEE Vehicular Technology Conference, Anchorage, USA, September 2009*
- [3] G. Micallef, P. Mogensen, H. O. Scheck: “Cell Size Breathing and Possibilities to Introduce Cell Sleep Mode”. *European Wireless Conference*, p. 111-115, 2010.
- [4] M. A. Marsan, L. Chiaraviglio, D. Ciullo, M. Meo: “Optimal Energy Savings in Cellular Access Networks”. *Proc. IEEE ICC’09 Workshop, GreenComm, June 2009*.
- [5] S. Zhou, J. Gong, Z. Yang, Z. Niu, P. Yang: “Green Mobile Access Network with Dynamic Base Station Energy Saving”. *MobiCom’09, Sept 2009, Beijing, China*.
- [6] M. Jada, J. Hämäläinen, R. Jäntti, M. M. A. Hossain: “Power Efficiency Model for Mobile Access Network”. *IEEE PIMRC’10 Workshop, W-Green, Sept 2010, “In press”*.
- [7] M. Jada, J. Hämäläinen, R. Jäntti, M. M. A. Hossain: “Impact of Femtocells to the WCDMA Network Energy Efficiency”. *IEEE Ic-bnmt, China, Oct 2010, “In press”*.
- [8] J.T.Louhi: “Energy efficiency of modern cellular base stations”, *INTELEC 2007, Rome, Italy*.
- [9] Press Release on NEC FP 810 femtocell product, 2010. <http://www.slashgear.com/nec-fp810-femtocell-tiny-but-14-45-7mbps-data-rates-1073529/>.

Performance of IEEE 802.15.4a Receivers in Randomized Multiuser Interference in AWGN Channel

Ville Niemelä⁽¹⁾, Alberto Rabbachin⁽²⁾,
Matti Hämäläinen⁽¹⁾, Jari Iinatti⁽¹⁾

⁽¹⁾*University of Oulu, Centre for Wireless Communications,
P.O.BOX 4500, 90014-Oulu, Finland*

⁽²⁾*Institute for the Protection and Security of the Citizen, Joint Research Centre,
Via Enrico Fermi 2749, 21027-Ispra, Italy*

Email: ⁽¹⁾firstname.lastname@ee.oulu.fi, ⁽²⁾firstname.lastname@jrc.ec.europa.eu

INTRODUCTION

In wireless networks, the development is generally going towards smaller networks as various applications are being developed for different purposes; from local area networks (WLAN) through personal area networks (WPAN) to body area networks (WBAN). For healthcare and welfare sector, WBAN applications offer new solutions for measuring physiological parameters or tracking people or devices. In this area, improvements are needed because the population is aging, in the developed countries especially, and therefore the need of a nursing staff is constantly increasing as well as the relating nursing costs. Wireless measurements enable patients to stay home since the location is not necessary an issue and the measured data can be transferred from various places to a database accessed by the nursing staff in the hospital. Free time activities are also a potential area for WBAN applications since the requirements of the equipment during various sport exercises are similar than in medical applications. [1]

At the moment, there is an ongoing work by the IEEE for a WBAN standard 802.15.6 for low power devices [2]. IEEE published the IEEE 802.15.4a standard in 2007 for low-data-rate, low-power and low-complexity wireless personal area networks [3]. Because WBAN is a part of the WPAN, the IEEE 802.15.4a standard is suitable for body area network studies also. In this paper, ultra wideband (UWB) specifications of IEEE 802.15.4a [3] are followed in the implementation of a Matlab[®] based simulator. UWB technology offers high bandwidth, ranging capability and reduced receiver complexity due to baseband pulses [4]. The performance of different types of receivers is simulated in additional white Gaussian noise (AWGN) channel in the presence of similar interfering signals as a desired information signal. AWGN is the simplest channel model and chosen as a reference for the future fading channel simulations. The interfering signals can be from the other users of the same or a similar wireless sensor network, i.e., multiuser signals, which are randomly overlapped with the desired signal.

SYSTEM MODEL

The simulator is implemented according to the IEEE 802.15.4a UWB specifications. In impulse radio transmitters, the UWB waveform is expressed as [3]

$$x^{(k)}(t) = \left[1 - 2g_1^{(k)}\right] \sum_{n=1}^{N_{cpb}} \left[1 - 2s_{n+kN_{cpb}}\right] \times [p(t - g_0^{(k)}T_{BPM} - h^{(k)}T_{burst} - nT_c)] \quad (1)$$

where $g_0^{(k)}$ and $g_1^{(k)}$ are position and phase modulated bits, respectively. Sequence $s_{n+kN_{cpb}} \in \{0,1\}$, $n = 0, 1, \dots, N_{cpb} - 1$, is the scrambling code used in the k^{th} interval and $h^{(k)} \in \{0, N_{hop}-1\}$ is the k^{th} burst hopping position defined by the scrambler also. $p(t)$ is the transmitted pulse waveform at the antenna input, T_{BPM} is the half length of a symbol for the position modulation of the burst, T_{burst} is the length of a burst and T_c is the length of a pulse.[3]

Fig.1 presents the symbol structure with eight planned users, each with allocated burst transmission timeslot inside symbol quarters. The first quarter of the symbol is for position modulated zero bit and the third quarter for position modulated one bit. With eight users, a burst can have 1, 2, 16 or 128 pulses with 15.60, 7.80, 0.98 or 0.12 MHz symbol rates, respectively. [3]

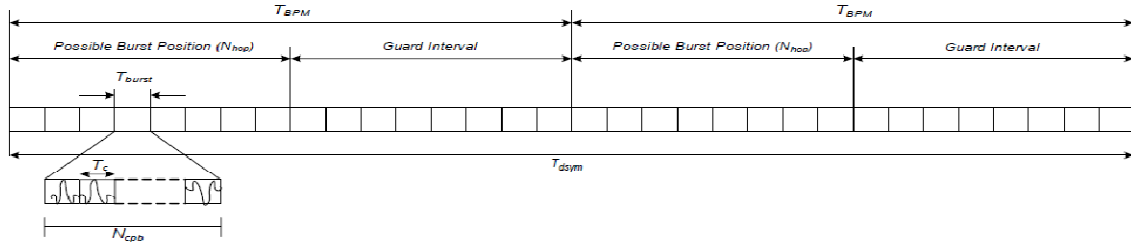


Figure 1. UWB symbol structure in IEEE 802.15.4a with eight users.

The other signals than the desired one are considered as multiuser interference, $x_{if}(t)$, and for the bursts of these signals, the time slot allocation $h^{(k)}$ is not utilized in the modeling. Waveforms from other radio systems are omitted. The starting instants of the transmission of the multiuser bursts are randomized by discrete uniform distribution to any given instant within a symbol quarter allocated by the position modulation. Therefore multiuser bursts can cause total or partial overlapping to the desired information burst, or in the best scenario, the bursts are not overlapping at all. Except for the timeslot allocation, the multiuser signals are built in similar way as the desired signal with equal length of bursts. Therefore, the modeling covers two different scenarios; *i*) the channel destroys the coordinated fashion of the symbol structure or *ii*) the interfering users are from another WBAN system in a close range.

Three different receiver types are investigated in this paper; a coherent receiver, a binary orthogonal non-coherent receiver with and without convolutional coding and an energy detector (ED). Reed-Solomon channel coding is utilized in all the receiver types due to the position modulation of the code bits. Convolutional channel coding is phase modulated and can be detected coherently only.

Coherent detection can be expressed as

$$v_i^{(k)} = \int_q^{q+T_{burst}} r(t - \tau)w(t) d\tau, i=0,1 \quad (2)$$

where $r(t) = x(t) + x_{if}(t) + n(t)$, $n(t)$ is additional Gaussian noise and $w(t)$ is a reference burst, either equal to or opposite in polarity to the transmitted burst. $q = k2T_{BPM} + iT_{BPM} + h^{(k)}T_{burst}$, defines the starting point of the integration which is assumed to be known exactly.

Since the transmitted signal is both position and phase modulated, the detection of the position modulated bit has to be done in a non-coherent manner. The comparison of the

absolute values defines which position modulated binary number has been received in the non-coherent receiver

$$\left| v_0^{(k)} \right| \underset{\substack{\text{"1"} \\ \geq}}{\overset{\substack{\text{"0"} \\ \leq}}{}} \left| v_1^{(k)} \right|. \quad (3)$$

If $v_0^{(k)}$ is bigger than $v_1^{(k)}$, the received position modulated bit is '0', otherwise '1'. The phase modulated bit is detected by taking the correlation output described in (2) based on the position modulation result in (3)

$$v_0^{(k)}, v_1^{(k)} \underset{\substack{\text{"0"} \\ \geq}}{\overset{\substack{\text{"1"} \\ \leq}}{}} 0. \quad (4)$$

Comparison is made to zero, i.e., bigger than zero, the phase modulated bit is '1', '0' otherwise.

In ED, an ideal band-pass filter is used to reduce the noise. The decision variable in ED is expressed as

$$w_i^{(k)} = \int_q^{q+T_{burst}} r(t)^2 dt, i=0,1. \quad (5)$$

A comparison is made between the decision variables in order to detect the received bit

$$w_0^{(k)} \underset{\substack{\text{"1"} \\ \geq}}{\overset{\substack{\text{"0"} \\ \leq}}{}} w_1^{(k)}. \quad (6)$$

RESULTS

Fig.2 presents the results for two different data rates, thus different burst lengths. With data rate of 0.98 MHz there are 16 pulses in a burst and with 7.80 MHz 2 pulses in a burst [3]. Different colors of the curves present different receiver types. The bit error rate (BER) results are presented as a function of E_b/N_0 , i.e., energy of bit over noise. The energy of a bit, independent of the number of pulses in a burst, is always normalized to one. In the simulations, 1.155×10^6 bits per E_b/N_0 value was simulated. Coherent receiver offers the best performance in terms of BER. Non-coherent receiver with convolutional channel coding has approximately 2 dB worse performance. Without the convolutional coding in the non-coherent receiver, the difference in performance is approximately 4.5 dB worse when compared to the reference coherent receiver.

The performance of ED depends on the burst length, due to the receiver operation presented in (5). With long burst, the integrated noise increases and therefore the performance with short burst is better. The difference in performance compared to non-coherent receiver without convolutional coding changes from 2 dB to approximately 5 dB, depending on the burst length in ED.

For coherent and non-coherent receivers, having more pulses in a burst offers robustness against randomized overlapping multiuser interference in AWGN. For a short burst, multiuser interference seems to have more impact on the performance of coherent and non-coherent receivers. With both burst lengths, ED seems to be very

vulnerable for the multiuser interference as can be seen from the Fig.2. Even one randomly overlapping multiuser signal corrupts the detection of the desired signal.

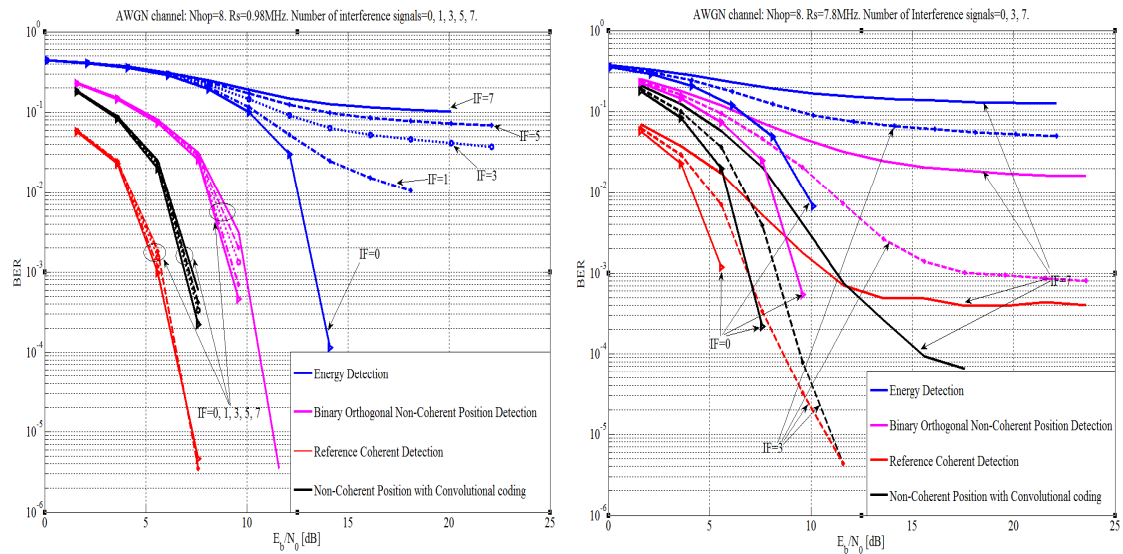


Figure 2. Effect of multiuser interference on different receiver types.

CONCLUSIONS

The presented results are in AWGN, without the time slot allocation for the interfering signals and the signals are randomly overlapping. In a real WBAN channel, the time slot allocation would be applied but on the other hand the channel would lengthen the signal causing inter symbol interference and multiuser interference.

The results show a general conclusion that with the most complex receiver structure is achieved the best performance, coherent receiver being the best and ED the worst receiver in terms of BER. In non-coherent receiver with short burst especially, having convolutional channel coding in the case of many multiuser signals provides significant improvement in the performance when compared to the non-coherent receiver without convolutional coding. From the burst length point of view, longer the burst, thus smaller data rate, better the robustness against multiuser interference signals. Only exception is ED, which is equally vulnerable to multiuser interference with different lengths of bursts, i.e., with different data rates.

REFERENCES

- [1] Hämmäläinen M., Pirinen P., Shelby Z. (2007) Advanced Wireless ICT Healthcare Research. Mobile and Wireless Communication Summit, 1-5 July 2007. 16th IST, Budapest, Hungary.
- [2] IEEE 802.15 WPAN Task Group 6 (TG6) Body Area Networks. <http://www.ieee802.org/15/pub/TG6.html> Page available at 03.06.2010.
- [3] IEEE Standard 802.15.4a: Part 15.4: Wireless Medium Access Control (MAC) and Physical Layer (PHY) Specifications for Low-Rate Wireless Personal Area Networks (WPANs), Amendment 1: Add Alternate PHYs. IEEE Computer Society, IEEE Std 802.15.4a-2007 (Amendment to IEEE Std 802.15.4-2006), USA. 187 p.
- [4] Rabbachin A. (2008) Low complexity UWB receivers with ranging capabilities. Acta Universitatis Ouluensis, Series C, Technica 298. University of Oulu, Oulu.